© Copyright by Chinkyo Kim, 1998

STRAIN RELAXATION MECHANISM OF SEMICONDUCTOR THIN FILMS

BY

CHINKYO KIM

B.Sc., Seoul National University, 1993
M.S., University of Illinois at Urbana-Champaign, 1995

THESIS

Submitted in partial fulfillment of the requirements
for the degree of Doctor of Philosophy in Physics
in the Graduate College of the
University of Illinois at Urbana-Champaign, 1998

Urbana, Illinois

STRAIN RELAXATION MECHANISM OF SEMICONDUCTOR THIN FILMS

BY

CHINKYO KIM

B.Sc., Seoul National University, 1993
M.S., University of Illinois at Urbana-Champaign, 1995

THESIS

Submitted in partial fulfillment of the requirements
for the degree of Doctor of Philosophy in Physics
in the Graduate College of the
University of Illinois at Urbana-Champaign, 1998

Urbana, Illinois

STRAIN RELAXATION MECHANISM
OF SEMICONDUCTOR THIN FILMS

Chinkyo Kim, Ph.D.
Department of Physics
University of Illinois at Urbana-Champaign, 1998
Ian K. Robinson, Advisor

For the atoms at clean surface of crystal, the atomic bonding environment is very different from that of deep inside bulk crystal. This fact forces those atoms to rearrange themselves in such a way that reconstruction occurs with the total energy being minimized. Reconstruction also takes place when foreign atoms are deposited on a clean surface. This strain experienced by individual atoms will propagate into a bulk crystal down to a few layers, sometimes even to several layers. Using x-ray diffraction, the positions as well as thermal vibrational amplitudes of these strained atoms can be determined. In the first part of this thesis, we present the surface reconstruction and a strain analysis of Sb/Si(111) using synchrotron radiation x-ray diffraction.

Another case when we can observe macroscopic strain is heteroepitaxial film growth. Even though there is lattice mismatch between substrate and film, pseudomorphic film growth is usually possible at the initial stage of growth, so the film is grown under strain. However, it becomes energetically favorable to introduce misfit dislocations above a certain thickness of film growth, which is called a critical thickness. In this case, strain is considered in the continuum elastic sense, defined by the lattice constant of the material. From measurement of the positions of multiple Bragg reflections, accurate values of lattice constant can be obtained using x-ray diffraction as a function of film thickness and a critical thickness can be determined. The second part of the thesis is a study of III-nitride thin films grown on sapphire (0001) substrate with molecular beam epitaxy. Irradiation experiments were also performed

to investigate whether strain relaxation takes place in SiGe films and GaN films to look for indications of metastability.

Acknowledgments

First of all, I would like to thank God for all things. He has always been faithful to me through all those tough and happy days in my life. Sometimes I faced difficulties, but I could accept those with His help and thank Him. I believe that these experiences helped me spiritually grow up. I could never even imagine that I could do anything in my life without Him. And I really thank my parents for the most precious inheritance in the world, the faith in Jesus Christ. Their unfailing love and support have proved valuable help all the time. I also thank my brother and sister for their encouragement and guidance.

I, from the deepest part of my heart, thank Professor Ian K. Robinson for his guidance and support during my stay at the University of Illinois. I have never seen such a person who is so excellent in an area of science and who has such a wonderful personality. He provided an excellent example for me both as a scientist and as a kind person. I thank Professor Kyekyoon Kim for his care and help, too. This work might have not been possible without his support. I also would like to thank Professor Jong-Chun Woo at the Seoul National University. His care and encouragement made my continuous study at the University of Illinois possible. My office mates, Kyu-Hwan Shim and Jaemin Myoung, were among my best senior friends at the University of Illinois. They cared for me so much that I can't thank them too much. Without them, my study would have been much tougher and not enjoyable. I would never forget all those days in the laboratory. And I also thank other friends in Ian's Lab, Dr. Yong Song Chu, Dr. Kevin Whiteaker, Don A. Walko, David Fanning, John Pitney, and Arunabha Ghosh. My former roommates, Yonghoon Kim and Mike Cich, shared a lot of good times with me over my last year here. They have been really good friends. My special thanks to my friend Seokhyun Yoon and other Korean graduates and

researchers in Physics must be given here. I would like to thank all the members of the Bible study group which I have been in. Their care and prayer became one of the biggest supports for this thesis. I also would like to thank Korean Foundation for Advanced Studies for their consistent support from 1990 through the end of my study at the University of Illinois.

This work was supported by the U. S. Department of Energy under Grant No. DEFG02-96ER45439 and by Samsung Electronics Co. LTD.. NSLS is supported by U. S. DOE under grant No. DE-AC012-76CH00016.

Table of Contents

Chapter I. Introduction ... 1

Chapter II. Theoretical background ... 4

2.1 Fundamentals of X-ray diffraction ... 4

2.1.1 Bragg peaks from bulk ... 4

2.1.2 Fractional order peaks and crystal truncation rod ... 6

2.1.3 Algebra of orientation matrix ... 9

2.1.4 X-ray diffraction geometry ... 10

2.2 Theory of strain and dislocations ... 12

Chapter III. Strain propagation of Sb/Si(111) into bulk ... 18

3.1 CTRs of Si(111) ... 18

3.2 Introduction to Sb/Si(111) ... 18

3.3 Results and discussion ... 20

Chapter IV. Strain analysis of GaN thin films ... 31

4.1 Introduction ... 31

4.2 Critical thickness of GaN ... 34

4.3 Effect of buffer layer relaxation on the critical thickness ... 43

Chapter V. Effect of AlN buffer layer on the strain relaxation of GaN ... 54

5.1 Thin film diffraction of AlN ... 54

5.2 Thickness dependence of AlN on the strain of GaN ... 54

Chapter VI. Strain relaxation induced by irradiation in Si_xGe_{1-x} films ... 60

6.1 Irradiation with 25 keV Ga^+ ions ... 64

6.2 Irradiation with 3 keV He^+ ions ... 75

Chapter VII. Strain relaxation induced by irradiation; evidence of equilibrium theory for GaN ... 82

Chapter VIII. Summary and conclusion 90

References 91

Vita 99

List of Tables

Table 1: Displacement parameters used for a least-squares fit. Also shown are thermal vibration amplitudes $\sigma = \sqrt{<u^2>}$ for Sb, the first three layers near surface, Si(S), and bulk Si below three layers, Si(B). Numbers are all in Å units 26

Table 2: Bond lengths between atoms near surface in Å. Numbering of Si atoms is shown in Fig. 11 27

Table 3: Previously measured Sb-Sb bond lengths in Å in Si(100) and Si(111) with different technique 28

Table 4: Physical parameters of III-nitrides and sapphire 32

Table 5: Thickness and in-plane lattice constant of GaN and AlN layers in each sample 44

Table 6: A list of SiGe samples irradiated 62

Table 7: Irradiation dose for each SiGe samples. Note that these samples were irradiated with 3 keV He^+ ions except the sample A with 25 keV Ga^+ 63

Table 8: Irradiation dose for each GaN samples. All these samples were irradiated with 3 keV He^+ ions. The samples B and C are the same as in Ch. IV. 89

List of Figures

Figure 1: Diffraction pattern from different dimensional system 7

Figure 2: Typical CTRs with different surface configuration 8

Figure 3: Schematic diagram of diffractometer angles. Incident and exit angles are also shown 11

Figure 4: Epitaxial film growth below and above the critical thickness . 13

Figure 5: Typical slip plane and dislocation system in Si(001) 14

Figure 6: Plan view of typical 60° type dislocation and Burger's vector of Si. Surface normal is (111) 15

Figure 7: A unit cell of Si, which has a diamond structure 19

Figure 8: Bragg peaks of Si in reciprocal space and CTRs 20

Figure 9: UHV chamber installed in X16A at NSLS 21

Figure 10: Patterson function of Sb ($\sqrt{3} \times \sqrt{3}$) structure on Si(111). Peaks are identified with numbers corresponding to the inter-atomic vectors between Sb shown in Fig. 11 23

Figure 11: ($\sqrt{3} \times \sqrt{3}$) surface reconstruction of Sb on Si(111). Solid, hatched and hollow circles represent Sb, the first layer and the second layer of Si atoms, respectively. Lateral displacements from the ideal positions for the first layer of Si atoms are shown. d_{12} for Sb atoms is a absolute distance, not a displacement. Inter-atomic vectors between Sb are also shown corresponding to six peaks in the Patterson function 24

Figure 12: Side view of Sb adsorbed Si(111). Vertical displacement vectors are shown for the first three layers of Si near surface 25

Figure 13: Integrated intensities of fractional and integer order rods . . . 29

Figure 14: Integrated intensities of in-plane peaks for a fractional order. The radii of solid and hollow semi circles are proportional to measured and calculated integrated intensities, respectively. Experimental errors are represented as outer shells of solid circles 30

Figure 15: Wurtzite GaN unit cell 33

Figure 16: Unit cells of sapphire (0001) and AlN superimposed. Solid line is for sapphire and dashed line for AlN. Open circles and hatched ones represent O in sapphire and Al in AlN, respectively 35

Figure 17: Kappa diffractometer 37

Figure 18: Fit of in-plane lattice constant *a* as a function of GaN layer thickness 39

Figure 19: Lattice constant c as a function of GaN layer thickness 40

Figure 20: Reciprocal lattice map near (103) Bragg peaks of sample C. The GaN reciprocal lattice unit was used for indexing. Two peaks which has the same *h* value are clearly visible 45

Figure 21: Index scan along *l* direction through (103) peak. Two Gaussians were used to fit AlN and GaN peaks 46

Figure 22: Reciprocal lattice map near (103) Bragg peaks of sample D. The GaN reciprocal lattice unit was used for indexing. A very weak AlN peak is shown on the shoulder of GaN 47

Figure 23: Index scans along in all three directions. A fit of Gaussians was done for *l* scan. This time the AlN reciprocal lattice unit was used for indexing 48

Figure 24: In-plane lattice constants of AlN and GaN films on sapphire(0001)

with the fit using a simple theory 50

Figure 25: In-plane lattice constants of AlN and GaN films on sapphire(0001) with the fit using an improved theory 51

Figure 26: Theoretical description of in-plane lattice constants above the critical thickness with various γ's. This plot corresponds to Eq. (40) with a fixed β' 52

Figure 27: Fit of (00L) rod of 80 Å thick AlN film on sapphire substrate. A model with 65 alternating Al and N layers was used with several layers near the interface allowed to relax. The distance between sapphire and AlN at the interface was set to 0.45 Å 55

Figure 28: Change of fits with variation of interface distances. The same sample as shown in Fig. 27 with $d_\circ$=0.45 Å 56

Figure 29: Lattice constant a of a series of AlN layers. $h_c = 4 \pm 2$ Å was used 57

Figure 30: In-plane lattice constant of GaN in samples A through E ... 58

Figure 31: Mesh scans of a SiGe sample irradiated with 25 keV Ga^+ ions 65

Figure 32: Lines of trace of the highest intensity in mesh scans 66

Figure 33: Index scans along h direction through (202) 67

Figure 34: Diffuse scattering component of irradiated sample 68

Figure 35: In-plane lattice constant of $Si_{0.7}Ge_{0.3}$ film as a function of thickness predicted by equilibrium theory 69

Figure 36: A 1-dimensional model of strain relaxation. Hollow circles represent original unrelaxed lattice points and solid ones are for relaxed lattice points... 70

Figure 37: Diffraction intensity calculation using a 1-dimensional model of strain relaxation, described in the text 72

Figure 38: A plot of peak width and shift as a function of dose. Domain size calculated from peak width and shift is also shown in the upper panel 73

Figure 39: Scans of the sample B through (202) peak 76

Figure 40: Scans of the sample C through (202) peak 77

Figure 41: Scans of the sample D through (202) peak 78

Figure 42: Scans of the sample E through (202) peak 79

Figure 43: Dilation effect of out-of-plane lattice constant upon irradiation. Note that the sample D was irradiated with the sample hot and the sample E was irradiated without rastering. So, the dose was estimated from the amount of dilation 80

Figure 44: Scans of the sample B through (101) peak 84

Figure 45: Scans of the sample B through (102) peak 85

Figure 46: Scans of the sample C through (101) peak 86

Figure 47: Scans of the sample G through (101) peak 87

Chapter I. Introduction

One of the most powerful feature of physics is that it can explain and predict many different phenomena using different models on the basis of a few fundamental principles. Once an interesting problem is observed, a model is proposed to explain it and changes on the model are made until it is successfully applicable to the problem. Ever since atoms were known as building blocks of nature in one sense and are arranged in such a beautifully organized way that some materials are crystallized, it was found that those atoms bond one another in such a way that a total energy of the system is minimized. In this case, the governing principle of a periodic arrangement of atoms is energy minimization. The ways atoms arrange themselves periodically in crystalline matters depend on the properties of elements and many properties of crystalline materials are closely related to the periodicity of the constituents. Therefore, it is of significant importance to have knowledge of a structure before pursuing to investigate other properties of the material.

The configuration of atomic arrangement in crystalline material changes whenever there are introduced a different environment around atoms in which we are interested. For example, surface atoms of bulk crystal experience totally different bonding environment in contrast with those deep inside bulk because they face into the air so that they rearrange themselves in order to minimize a total energy. This is called surface relaxation. If foreign species are deposited on a surface, they will sit on energetically favored places with relaxation of existing surface or a few deep layers. That is called surface reconstruction. These are among strain relaxation mechanism controlled by energy minimization from a microscopic point of view. By a microscopic point of view, we mean that we are interested in atomic arrangement of each atoms at the surface and several layers below it.

Likewise, we can extend the concept of strain relaxation when we are concerned only with macroscopic physical quantity such as lattice constant. This can be easily visualized with growth of lattice mismatched films. In other words, when lattice mismatched film is grown on a substrate it could be grown either pseudomorphically, accommodating the lattice mismatch in the form of elastic strain energy, or incommensurate by introducing misfit dislocations. It is determined by energy minimization whether dislocations will be introduced to accommodate misfit. Sometimes, a system of thin film is not at the minimum of total energy due to other controlling factors such as kinetic effects. It depends on each system whether it will be equilibrated at minimum energy. Due to the reasons mentioned above, understanding of strain relaxation of crystalline materials is of interest from the physics point of view. Growing demand of device industry, which exploits various properties of epitaxial thin films, made this area of technological interest, too.

With capability of controlling atomic levels of deposition such as in molecular beam epitaxy (MBE) or chemical vapor deposition (CVD) techniques, we are able to study surfaces with adsorbates or interface structures of two different material in a sense of strain analysis. Since every material has its own lattice constant, it is no wonder that when we deposit on a substrate a different element we expect strain near interface of two materials. Depending on how large the lattice mismatch is, the strain propagates quite far inside each material or just a few layers. Therefore, more demands for thin film industry requires more intensive knowledge of this area. And it gives importance of understanding that strain of thin films are one of the main factors controlling electronic and optical properties of the films.

To investigate those properties of strained or relaxed materials, a lot of analysis tools have been used and x-ray diffraction is one of them. In the past x-ray diffraction was not widely used in surface science until the advent of synchrotron radiation source

because the intensity from surface layers was too low to detect with a conventional table top x-ray source. However, synchrotron x-ray source made it possible to study a surface structure of even a sub-monolayer. X-ray diffraction has a couple of unique advantages over other surface analysis tools. First of all, it does not interact much with material. In other words, the scattering cross section is so small that we can easily analyze diffraction data. As is clear from the previous sentence, it does not destroy samples, either. In addition to these, x-ray diffraction can be used not only to pin down the positions of individual atoms on a surface with appropriate reciprocal space measurements but also to measure the strain averaged over the film.

In this thesis, I present an investigation of strain relaxation of crystalline materials using the x-ray diffraction method. Strain relaxation of metal atoms on Si substrate will be analyzed in terms of the detailed atomic arrangement at and near the surface. Macroscopic analysis of strain relaxation of SiGe films and III-nitride films will also be given, which show two very different behaviors of strain relaxation.

Chapter II. Theoretical background

2.1 Fundamentals of X-ray diffraction[1]

2.1.1 Bragg peaks from bulk

The physical quantity we measure experimentally in an x-ray diffraction experiment is the intensity of x-rays diffracted from a material under investigation. Rigorously speaking, the x-ray is mostly diffracted by the electrons in a material. Therefore, by x-ray diffraction experiment we would like to know an electron distribution in a material. In the following section, we are going to explain how we can relate a physical quantity we measure with the electron distribution.

For simplicity, we consider an amplitude instead of an intensity from now on. First of all, we consider the amplitude scattered from one electron. From the general textbook of electromagnetic waves, we can find the Thompson formula[2, 3] which describes the amplitude of the wave A_1 that comes from a scattering electron at $\mathbf{r}_\mathrm{e}$, as a function of the amplitude of the wave $\mathrm{A}_\circ$ as shown in Eq. (1), assuming a dipole approximation,

$$\mathrm{A}_1 \exp(-i\mathbf{k}_\mathrm{f} \cdot \mathbf{r}_\mathrm{e}) \ = \ \mathrm{A}_\circ \exp(-i\mathbf{k}_\mathrm{i} \cdot \mathbf{r}_\mathrm{e}) \frac{e^2}{mc^2 \mathrm{R}_\circ} \tag{1}$$

where e and m are the electrons charge and mass, c speed of light, $\mathrm{R}_\circ$ distance between a scattering source and a detector, $\mathbf{k}_\mathrm{f}$ and $\mathbf{k}_\mathrm{i}$ are the wave vector of outgoing and incoming waves, respectively. So,

$$\mathrm{A}_1 \ = \ \mathrm{A}_\circ \frac{e^2}{mc^2 \mathrm{R}_\circ} \exp(i\mathbf{q} \cdot \mathbf{r}_\mathrm{e}) \qquad where \quad \mathbf{q} \ \equiv \ \mathbf{k}_\mathrm{f} - \mathbf{k}_\mathrm{i} \tag{2}$$

By integrating the electron density of an atom we can obtain the diffraction amplitude from an atom,

$$\mathrm{A}_2 = \mathrm{A}_\circ \frac{e^2}{mc^2 \mathrm{R}_\circ} \int \rho(\mathbf{r}') \exp(i\mathbf{q} \cdot (\mathbf{R_n} + \mathbf{r}_\mathrm{j} + \mathbf{r}')) \mathrm{d}^3\mathbf{r}'$$

$$= \mathrm{A}_\circ \frac{e^2}{mc^2\mathrm{R}_\circ}\mathrm{f}(q)\exp(i\mathbf{q}\cdot(\mathbf{R_n}+\mathbf{r}_\mathrm{j})) \tag{3}$$

where an atomic form factor,$\mathrm{f}(q)$, is given by $\mathrm{f}(q) = \int \rho(\mathbf{r}')\exp(i\mathbf{q}\cdot\mathbf{r}')\mathrm{d}^3\mathbf{r}'$. In other words, the atomic form factor is just a Fourier transformation of electron density of an atom. Note that the atomic form factor is written as a function of the magnitude of the momentum transfer, independent of direction, because in almost all cases the atom is spherically symmetric.

By summing up contributions from all atoms inside a unit cell, we can get an amplitude from a unit cell. Note that we should label form factors from different elements inside a unit cell since usually there are different elements inside a unit cell.

$$\begin{aligned}
\mathrm{A}_3 &= \mathrm{A}_\circ \frac{e^2}{mc^2\mathrm{R}_\circ}\sum_{\mathrm{j}=1}^{\mathrm{N_c}}\mathrm{f}_\mathrm{j}(q)\exp(i\mathbf{q}\cdot(\mathbf{R_n}+\mathbf{r}_\mathrm{j})) \\
&= \mathrm{A}_\circ \frac{e^2}{mc^2\mathrm{R}_\circ}\mathrm{F}(\mathbf{q})\exp(i\mathbf{q}\cdot\mathbf{R_n})
\end{aligned} \tag{4}$$

where the structure factor, $\mathrm{F}(\mathbf{q})$, is defined by $\mathrm{F}(\mathbf{q}) = \sum_{\mathrm{j}=1}^{\mathrm{N_c}}\mathrm{f}_\mathrm{j}(q)\exp(i\mathbf{q}\cdot\mathbf{r}_\mathrm{j})$. The final step is to consider a whole crystal.

$$\mathrm{A}_4 = \mathrm{A}_\circ \frac{e^2}{mc^2\mathrm{R}_\circ}\mathrm{F}(\mathbf{q})\sum_{\mathrm{n}_1=1}^{\mathrm{N}_1}\sum_{\mathrm{n}_2=1}^{\mathrm{N}_2}\sum_{\mathrm{n}_3=1}^{\mathrm{N}_3}\exp(i\mathbf{q}\cdot(\mathrm{n}_1\mathbf{a}_1+\mathrm{n}_2\mathbf{a}_2+\mathrm{n}_3\mathbf{a}_3)) \tag{5}$$

Now we introduce a very useful concept of reciprocal lattice. If we choose unit vectors for real space as $\mathbf{a}_1, \mathbf{a}_2, \mathbf{a}_3$ we can define reciprocal lattice vectors $\mathbf{b}_1, \mathbf{b}_2, \mathbf{b}_3$ as below.

$$\mathbf{b}_1 = 2\pi\frac{\mathbf{a}_2\times\mathbf{a}_3}{\mathbf{a}_1\cdot(\mathbf{a}_2\times\mathbf{a}_3)}, \quad \mathbf{b}_2 = 2\pi\frac{\mathbf{a}_3\times\mathbf{a}_1}{\mathbf{a}_1\cdot(\mathbf{a}_2\times\mathbf{a}_3)}, \quad \mathbf{b}_3 = 2\pi\frac{\mathbf{a}_1\times\mathbf{a}_2}{\mathbf{a}_1\cdot(\mathbf{a}_2\times\mathbf{a}_3)} \tag{6}$$

If we define $\mathbf{q} = h\mathbf{b}_1 + k\mathbf{b}_2 + l\mathbf{b}_3$

$$\begin{aligned}
\mathrm{I_s}(\mathbf{q}) &= \mathrm{A}_\circ{}^2\frac{e^4}{m^2c^4\mathrm{R}_\circ{}^2}|\mathrm{F}(\mathbf{q})|^2\left|\sum_{\mathrm{j}_1=1}^{\mathrm{N}_1}\sum_{\mathrm{j}_2=1}^{\mathrm{N}_2}\sum_{\mathrm{j}_3=1}^{\mathrm{N}_3}\exp(i\mathbf{q}\cdot(\mathrm{j}_1\mathbf{a}_1+\mathrm{j}_2\mathbf{a}_2+\mathrm{j}_3\mathbf{a}_3))\right|^2 \\
&= \mathrm{A}_\circ{}^2\frac{e^4}{m^2c^4\mathrm{R}_\circ^2}|\mathrm{F}(\mathbf{q})|^2\frac{\sin^2(\mathrm{N}_1a_1h\pi)}{\sin^2(\mathrm{a}_1\mathrm{h}\pi)}\frac{\sin^2(\mathrm{N}_2a_2h\pi)}{\sin^2(\mathrm{a}_2\mathrm{h}\pi)}\frac{\sin^2(\mathrm{N}_3a_3h\pi)}{\sin^2(\mathrm{a}_3\mathrm{h}\pi)}
\end{aligned} \tag{7}$$

If h, k, l=integers,

$$\mathrm{I_s}(h,k,l) \;=\; \mathrm{A_\circ}^2 \frac{e^4}{m^2c^4\mathrm{R}_\circ^2} |\mathrm{F}(\mathbf{q})|^2 \mathrm{N_1}^2\mathrm{N_2}^2\mathrm{N_3}^2 \tag{8}$$

These are Bragg peaks. As derived above, it is evident that the positions of Bragg peaks in a reciprocal space are dependent on the lattice constants of material observed and they can be easily measured from the Bragg peak positions.

2.1.2 Fractional order peaks and crystal truncation rod

In addition to the Bragg peaks which results from bulk property of material, there could be more distribution of diffraction peaks in reciprocal space. As shown in Eq.(7), if we average out the fast oscillation of numerators because in a real crystal N is a very large number, there would be streaks of intensity connecting Bragg peaks. However, in a real situation the faces of the parallelepiped illuminated by the x-ray beam is not well-defined except by one surface. Due to that reason, the streaks of intensity are mainly distributed near Bragg peaks and only one component of those streaks remains along the surface normal direction. This is called a crystal truncation rod (CTR) [4]. So, one of the ways to study surface roughness or other surface properties is to measure CTRs.

There is one more contribution to diffraction we need to consider. Atoms in a surface have a different bonding environment in contrast to those deep inside the bulk. So, it is energetically favorable for them to rearrange themselves in such a way that reduces the number of dangling bonds. This is called a surface reconstruction. Since a reconstructed surface has a larger periodicity than that of bulk, it results in fractional order diffraction rods between integer order Bragg peaks in reciprocal space. In a similar way, if we deposit some foreign elements on a surface, they usually cause a reconstruction so that we can observe fractional order diffraction rods in this case, too.

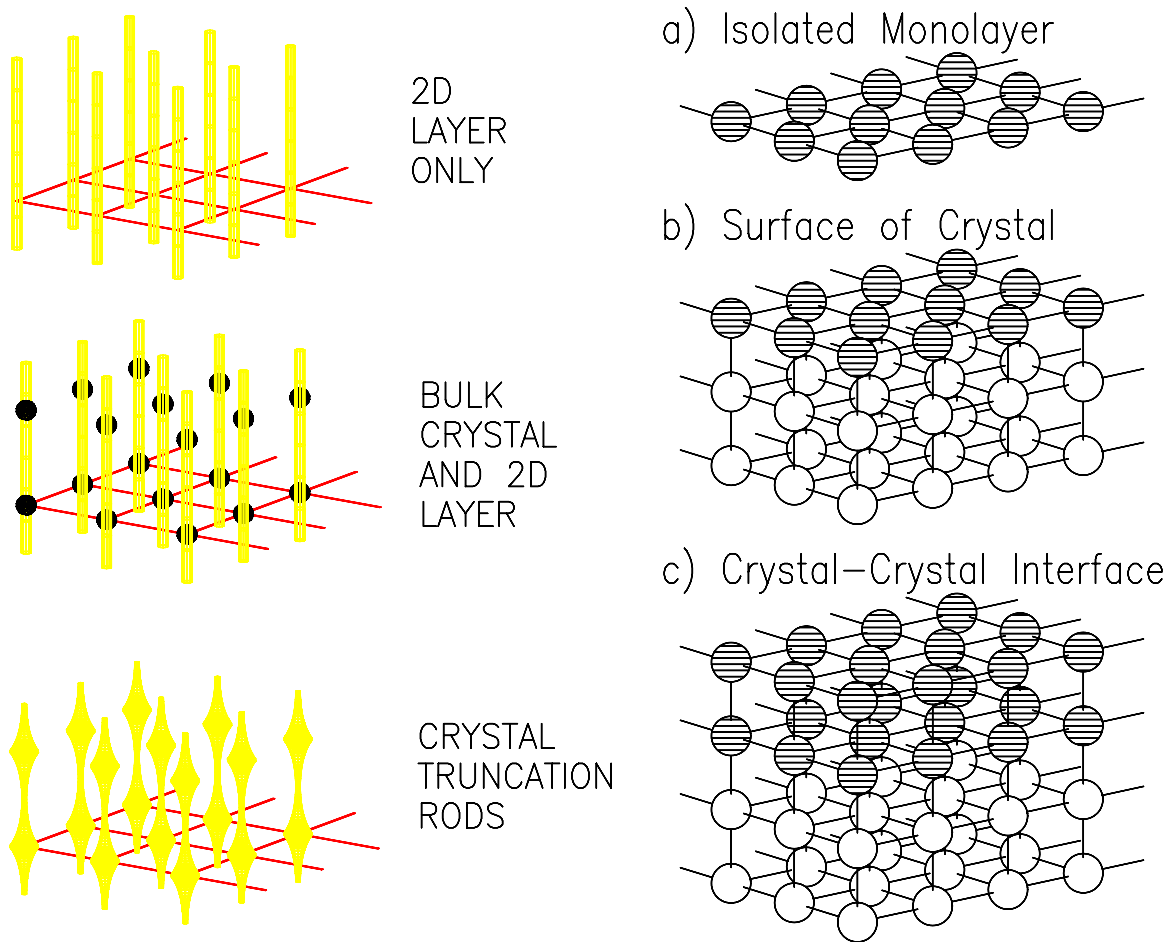

Figure 1: Diffraction pattern from different dimensional systems.

Therefore, what we can usually observe in a reciprocal space is 1) Bragg peaks from the bulk, 2) crystal truncation rods and 3) fractional order rods. In real experiments, there is also diffuse scattering which comes from several different contributions such as thermal vibration of atoms and defects distribution inside crystal. Depending on what kind of information we want to know, we determine which of the above we will concentrate on. Note that fractional order rods contain information of only surface reconstruction, but crystal truncation rods need to be measured to know the registry of surface atoms with respect to bulk atoms. In Fig. 1, three different diffraction

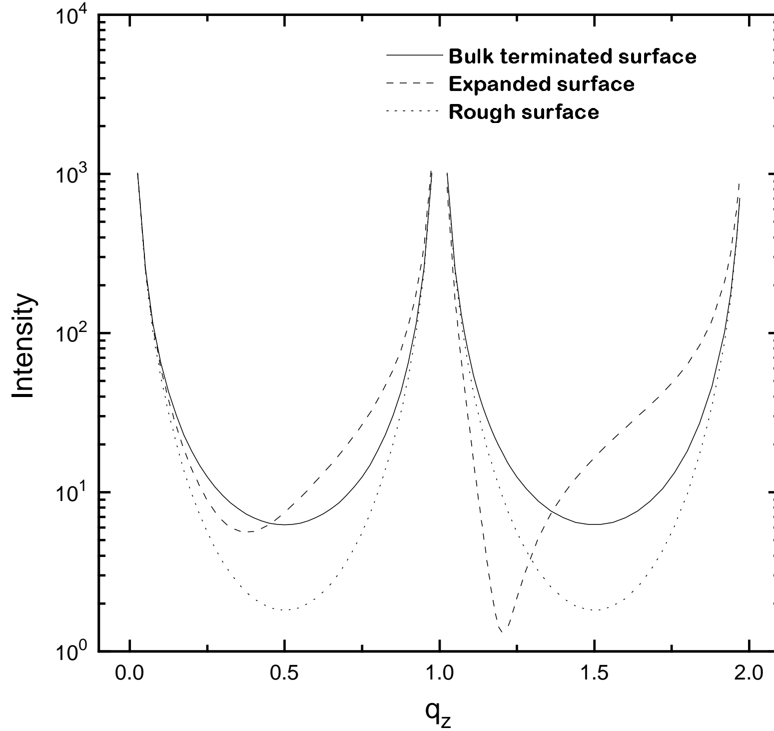

Figure 2: Typical CTRs with different surface configuration.

patterns are illustrated with corresponding crystal structures.

Now we consider the case when the surface is not perfectly bulk-terminated. For example, if the top layer of the surface is expanded, as shown in Fig. 2, the dashed curve is the CTR which we would observe. Due to the phase factor of the top expanded layer, the CTRs near Bragg peaks get asymmetric. The case shown in Fig. 2 is when the top layer expanded 10 %. If the top layer is contracted, it also gives asymmetric Bragg peaks, but the dip due to the modulation occurs below the Bragg peak. Another case when the CTR is altered results from surface roughness. A simple model of statistical roughness was proposed by Ian Robinson[4] and worked

quite well in many cases. In his model, roughness is parameterized with β which is a occupation probability of the first layer on top of the perfectly terminated crystal. Then, the probability of the second layer, the third layer and so on are given by β^2, β^3 … . Therefore, the CTR including surface roughness can be calculated as in Eq.(9), where $\mathrm{I_{ctr}}(\mathbf{q}\cdot\mathbf{a_3}) = 1/4\sin^2(\mathbf{q}\cdot\mathbf{a}_3/2)$. The dotted curve in Fig. 2 is a example of surface with a roughness of $\beta = 0.2$. However, this derivation is only true for a rough surface with unit cell high steps. In other words, if the unit cell consists of two atomic layers and the step is not a unit cell in height but an atomic layer, then the formula will not be a simple expression like Eq.(9).

$$\begin{aligned}
\mathrm{I_{ctr,rough}}(\mathbf{q}\cdot\mathbf{a_3}) &\propto \left|\sum_{\mathrm{j}=-\infty}^{0}\exp(i\mathbf{q}\cdot\mathrm{j}\mathbf{a}_3)+\sum_{\mathrm{j}=1}^{\infty}\beta^{j}\exp(i\mathbf{q}\cdot\mathrm{j}\mathbf{a}_3)\right|^2 \\
&= \left|\frac{1}{1-\exp(-i\mathbf{q}\cdot\mathbf{a}_3)}+\frac{\beta\exp(i\mathbf{q}\cdot\mathbf{a}_3)}{1-\beta\exp(i\mathbf{q}\cdot\mathbf{a}_3)}\right|^2 \\
&= \mathrm{I_{ctr}}(\mathbf{q}\cdot\mathbf{a_3})\frac{(1-\beta)^2}{1+\beta^2-2\beta\cos(\mathbf{q}\cdot\mathbf{a}_3)} \qquad (9)
\end{aligned}$$

An alternative roughness model has been proposed,[5] using a Poisson distribution with parameter λ rather than geometric. In that case, the intensity is given by

$$\mathrm{I_{ctr,rough}}(\mathbf{q}\cdot\mathbf{a_3}) \propto \mathrm{I_{ctr}}(\mathbf{q}\cdot\mathbf{a_3})\exp\Big(-4\lambda\sin^2(\frac{\mathbf{q}\cdot\mathbf{a_3}}{2})\Big) \qquad (10)$$

where a standard deviation of roughness is $\sigma = \sqrt{\lambda}$.

2.1.3 Algebra of orientation matrix

In this section, we briefly show how a least-squares fit works to construct the best reciprocal lattice from multiple Bragg peaks measurement. In order to make the explanation easier and since it is true that it is always possible to convert diffractometer angles to Cartesian coordinates, here we use Cartesian coordinates to locate Bragg peaks in the reciprocal space. Now consider we have n Bragg peaks which have indices (usually integers) of y_{ij}, where i runs from 1 to 3 and j from 1 to n.

These form a matrix, **Y**. Their Cartesian coordinates in the reciprocal space are x_{ij}, where i and j run from 1 to 3 and n, respectively. Note that we fix and use some reference coordinate system to locate the Bragg peaks from the beginning, which is defined relative to the zero's of the diffractometer angles by Busing and Levy[6]. If n is 3, there exists a unique 3×3 matrix **A** so that **Y=AX**. **A** is a transformation matrix which relates our reference coordinate system and the one we would like to define. In other words, it transforms the unit vectors from one coordinate system to those of the other. If n is larger than 3, there will not usually exist a matrix which satisfies **Y=AX**. So, our goal is to find a matrix **A** with known matrices **X, Y** which minimizes

$$\Lambda = \sum_{j=1}^{n} \sum_{i=1}^{3} (\sum_{k=1}^{3} a_{ik} x_{kj} - y_{ij})^2 \tag{11}$$

So,

$$\frac{\partial \Lambda}{\partial a_{pq}} = 2 \sum_{j=1}^{n} \sum_{i=1}^{3} (\sum_{k=1}^{3} a_{ik} x_{kj} - y_{ij}) \delta_{ip} x_{qj} = 2 \sum_{j=1}^{n} (\sum_{k=1}^{3} a_{pk} x_{kj} - y_{pj}) x_{qj} = 0 \tag{12}$$

which is in a matrix notation

$$\mathbf{A}\mathbf{X}\mathbf{X}^{\mathrm{T}} = \mathbf{Y}\mathbf{X}^{\mathrm{T}}. \tag{13}$$

Therefore,

$$\mathbf{A} = \mathbf{Y}\mathbf{X}^{\mathrm{T}}(\mathbf{X}\mathbf{X}^{\mathrm{T}})^{-1}. \tag{14}$$

Note that an inverse of **X** has no meaning since **X** is a 3×n matrix. We can calculate the lattice constants from a transformation matrix **A** because unit vectors of a reciprocal space have one-to-one correspondence with those of a real space. More details can be found in reference[6].

2.1.4 X-ray diffraction geometry

In our x-ray diffraction experiments, four angles, $2\theta, \theta, \chi$ and ϕ, are used to control the sample orientation and detector position. Since only three Eulerian angles are

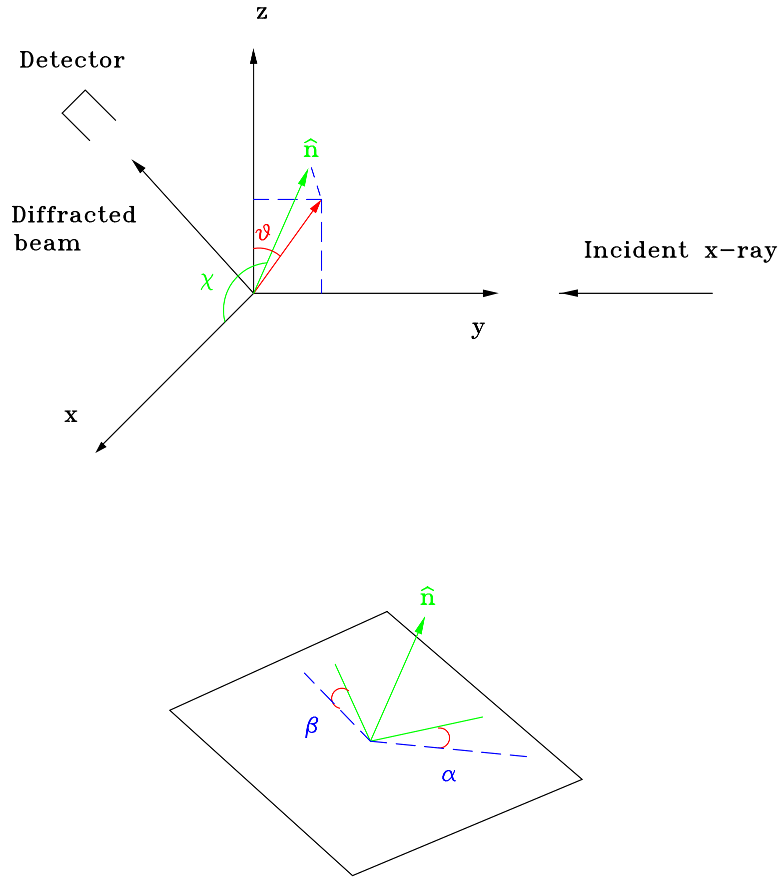

Figure 3: Schematic diagram of diffractometer angles. Incident and exit angles are also shown.

enough to determine a general orientation and the length of q, one of four angles is not needed and can be constrained. In our case, the incident and exit angles are set to be equal for constraint. These angles are determined with some of four diffractometer angles and are derived in the following paragraph.

In Fig. 3, a Cartesian coordinate is fixed and the surface normal vector moves as a function of θ and χ. The surface normal vector is defined by

$$\mathbf{n} = \mathbf{x}\cos\chi + \mathbf{y}\sin\chi\sin\theta + \mathbf{z}\sin\chi\cos\theta. \tag{15}$$

And the incident angle, α, is determined by

$$\alpha = \pi/2 - \cos^{-1}(\mathbf{n} \cdot \mathbf{y}) = \sin^{-1}\Big(\sin\theta \sin\chi\Big). \tag{16}$$

And in the same way, the exit angle, β, is determined by

$$\begin{aligned} \beta &= \pi/2 - \cos^{-1}\Big(\mathbf{n} \cdot (\mathbf{z} \sin 2\theta - \mathbf{y} \cos 2\theta)\Big) \\ &= \sin^{-1}(\sin 2\theta \sin\chi \cos\theta - \cos 2\theta \sin\chi \sin\theta). \end{aligned} \tag{17}$$

Note that, when a sample surface lies flat on the diffractometer ϕ-axis, the condition of the same incident and the exit angle is equivalent to the condition that the 2θ angle is twice as large as θ.

2.2 Theory of strain and dislocations

When a lattice mismatched film is to be grown on a substrate, there are typically two ways to accommodate the misfit between the film and the substrate: by elastic strain and misfit dislocations. The total energy of elastic strain is proportional to the thickness of a film multiplied by square of strain. On the other hand, the energy of dislocation is at the first order approximation proportional to misfit only, representing the dislocation density Due to these different dependence of energy of two types, at the initial stage of growth it is energetically favorable to accommodate a misfit by elastic strain only. So, the film is pseudomorphic. However, at a certain thickness it becomes the lower energy configuration to accommodate the misfit with combination of elastic strain and misfit dislocations, rather than elastic strain alone. The thickness where misfit dislocations are introduced is called a critical thickness and this is schematically shown in Fig. 4.

Dislocations are produced by slip of the most densely packed planes. A vector of such a slip displacement is called a Burger's vector which is the most important quantity associated with a dislocation. When a Burger's vector is parallel with the

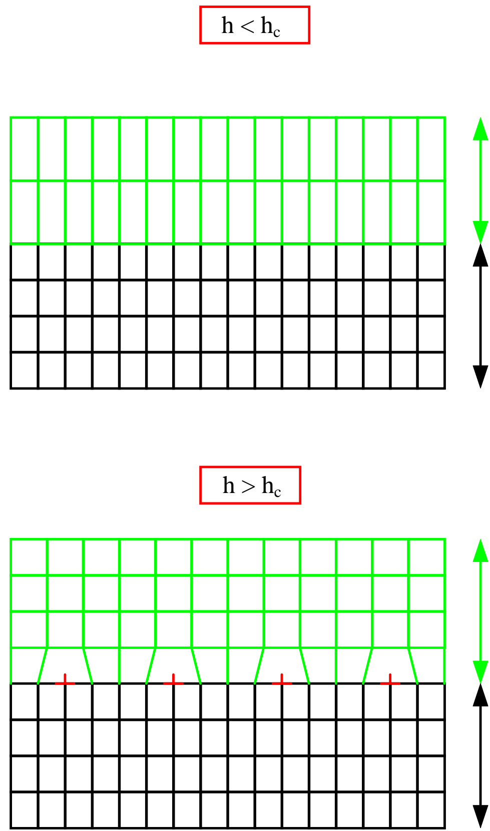

Figure 4: Epitaxial film growth below and above the critical thickness.

line of associated dislocation, it is a screw dislocation. When perpendicular, it's an edge dislocation. Depending on crystal systems, dislocations are on different crystallographic planes. For example, in FCC crystal the major operative slip system is {111}<110>, where {111} is the slip plane and <110> is the slip direction. The slip system and the Burger's vector is schematically shown in Fig. 5 and a plan view of them is shown in Fig. 6. More comprehensive theory of dislocations can be found in other references[7, 8]

Now we consider how to formalize a model to analyze macroscopic strain relaxation in thin films. From elementary elasticity theory the strain energy per unit area is

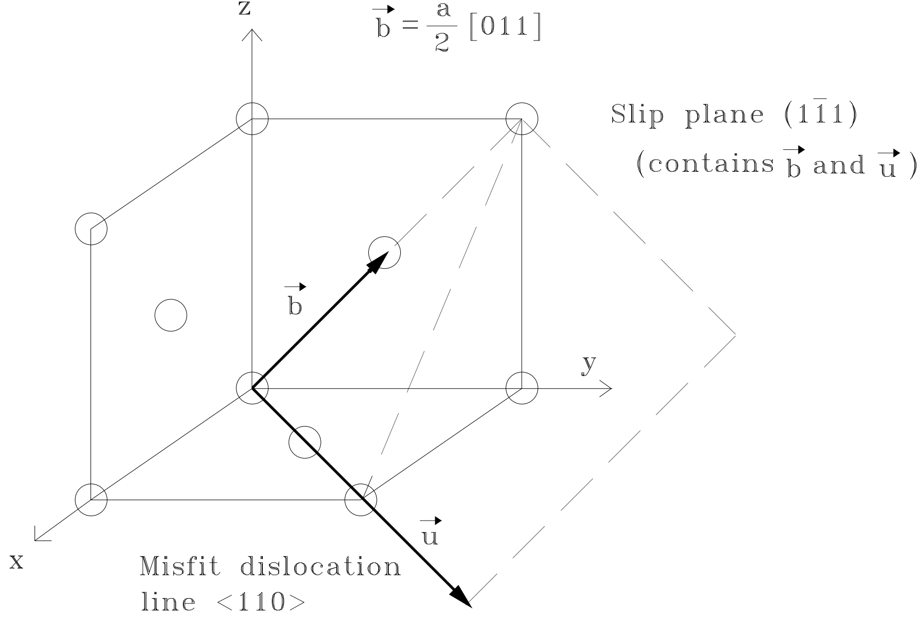

Figure 5: Typical slip plane and dislocation system in Si(001).

proportional to $h(a_\circ - a)^2$, where h is a film thickness, $a_\circ$ is the lattice constant of the completely relaxed material of the film and a is the actual lattice constant of the film. Assuming that the effective range of the dislocation field is constant, the energy due to dislocations depends on their density alone, which is proportional to $(a - a_s)$, where a_s is the in-plane lattice constant of the substrate. Then, the total energy of the strained film is given by

$$E = \alpha h(a - a_\circ)^2 + \beta(a - a_s) \tag{18}$$

where α and β are constants. In our work, we use an equilibrium theory to explain our experimental results. The basic assumption of the equilibrium theory is that the

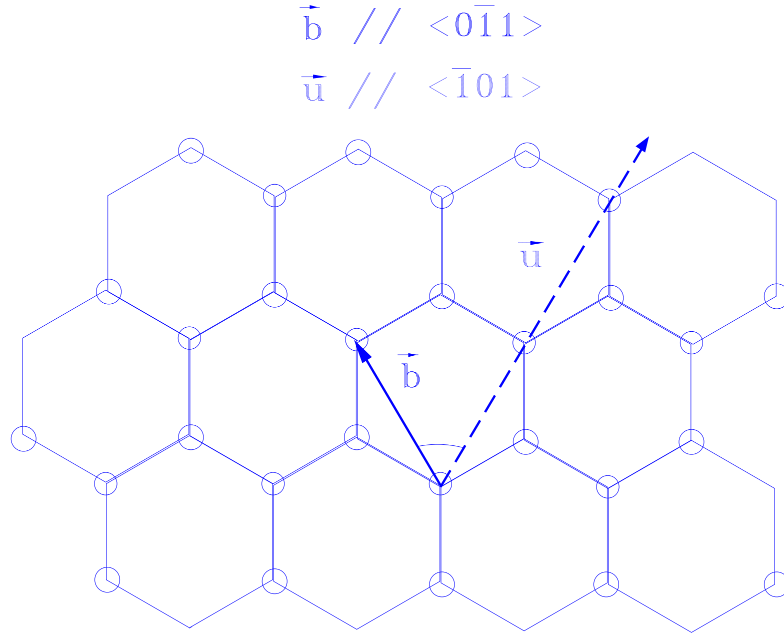

Figure 6: Plan view of typical 60° type dislocation and Burger's vector of Si. Surface normal is (111).

film is in a mechanical equilibrium state. For the system to be in equilibrium, this energy should be a minimum: $\partial E/\partial a = 0$. Then, to obtain the value of h_c, the critical thickness, we simply need to consider $a = a_s$. Setting $\partial E/\partial a = 0$ also gives a relation between h and a so long as $a > a_s$. At $a = a_s$, h is equal to h_c below which the film is pseudomorphic and a will have the same lattice constant as the substrate. The derived relation between a and h from Eq. (18) is

$$a = a_\circ + \frac{h_c}{h}(a_s - a_\circ) \tag{19}$$

The method we have used to determine h_c experimentally is to fit lattice constant data for thicker films, and use Eq. (19) as an extrapolation formula.

Now we consider the total energy more rigorously. The elastic strain ε depends on the mismatch between a film and its substrate, m, as well as the average number of dislocations present at the interface[9]. The relationship is given by

$$m = |\varepsilon| + \frac{b'}{p} \tag{20}$$

where $m = (a_\circ - a_s)/a_s$, $|\varepsilon| = |a_\circ - a|/a_\circ$, a_s is the lattice constant of the substrate, b' is the active component of the Burgers vector and p is the average distance between dislocations. Assuming ideal misfit dislocations we obtain the following expression.

$$\frac{b}{p} \approx m - |\varepsilon| \approx \frac{(a - a_s)}{a_\circ} \tag{21}$$

Using the expressions from Kasper,[9] a better estimate of the energy of the dislocations per unit length is given by

$$E_{ds} = \frac{\mu b^2}{4\pi(1-\nu)p}\left(1 + \ln\left(\frac{Q}{q}\right)\right) \tag{22}$$

where q is the inner cut-off radius, given by[10] $q = \pi b/(2\sqrt{2}(1-\nu))$, m is the shear modulus, ν is the Poissons ratio, b is a Burgers vector. Q is the effective range of the misfit dislocation field, and has two limiting values that depend on the density of dislocations, p

$$Q = p/2 \qquad \text{when} \quad h >> p/2 \tag{23}$$

$$= \frac{p(4hp)}{2(p^2 + 4h^2)} \approx 2h \qquad \text{when} \quad h << p/2 \tag{24}$$

We will use another approximation, $Q = hp/(2h + p/2)$, to interpolate smoothly between the two limits of Kasper. This then applies over the entire domain of h. With this approximation, the total energy of a film with thickness h is given by

$$E \approx \alpha(a - a_\circ)^2 h + \beta(a - a_s)\left(1 + \ln\left(\frac{2hp}{q(p+4h)}\right)\right) \tag{25}$$

Following the same calculation we used to obtain Eq. (19), we find,

$$(a - a_\circ)h = \left(1 + \ln\left(\frac{2hp}{q(p+4h)}\right) - \frac{1}{p^2} + \frac{1}{p(p+4h)}\right)\left(\frac{(a_s - a_\circ)h_c}{1 + \ln(2h_c/q)}\right) \tag{26}$$

where $p = ba_\circ/(a - a_s)$ as before. Since Eq. (26) is an implicit function, we must solve it numerically to obtain a as a function of h.

Chapter III. Strain propagation of Sb/Si(111) into bulk

3.1 CTRs of Si(111)

Si has a diamond structure with a lattice constant of a = 5.43 Å with cubic symmetry (Fig. 7). At room temperature a (7×7), so called DAS (Dimer Adatom Stacking fault) reconstruction is the stable state of a clean Si(111) surface. In our experiments, we chose a hexagonal coordinate system for Si(111) surface. Due to the bulk symmetry of Si, the CTRs of Si(111) have three different shapes as a function of l. As shown in Fig. 8, (1,0,l) type rods have Bragg peaks at $l = 1, 4, \ldots$, (1,1,l) types have peaks at $l = 0, 3, \ldots$ and (0,1,l) types have peaks at $l = -1, 5, \ldots$. Note that (0,1,2) type Bragg peaks are forbidden.

3.2 Introduction to Sb/Si(111)

The surface reconstruction resulting from the adsorption of foreign atoms has been one of the most extensively studied subjects in surface science because of the alteration of electronic properties of the surface by adsorption, which attracts significant interest from fundamental and technological points of view[11]. In particular, the surface reconstruction of Si induced by Sb draws interest due to the technological importance in the fabrication of Sb doped Si devices[12, 13, 14].

It has been reported that a clean Si(111) surface tends to form a $(\sqrt{3}\times\sqrt{3})$ reconstruction by adsorption of group III metals (Al, Ga, In) [15, 16, 17]. In contrast, the occurrence of a simple (1×1) structure by a column V metal, As, was reported[18]. Unlike As, a $(\sqrt{3}\times\sqrt{3})$ reconstruction of Sb on Si(111) was observed from a low energy electron diffraction(LEED) and x-ray photoelectron spectroscopy(XPS) study[19]. Since then many groups have studied the structure and a couple of structural models

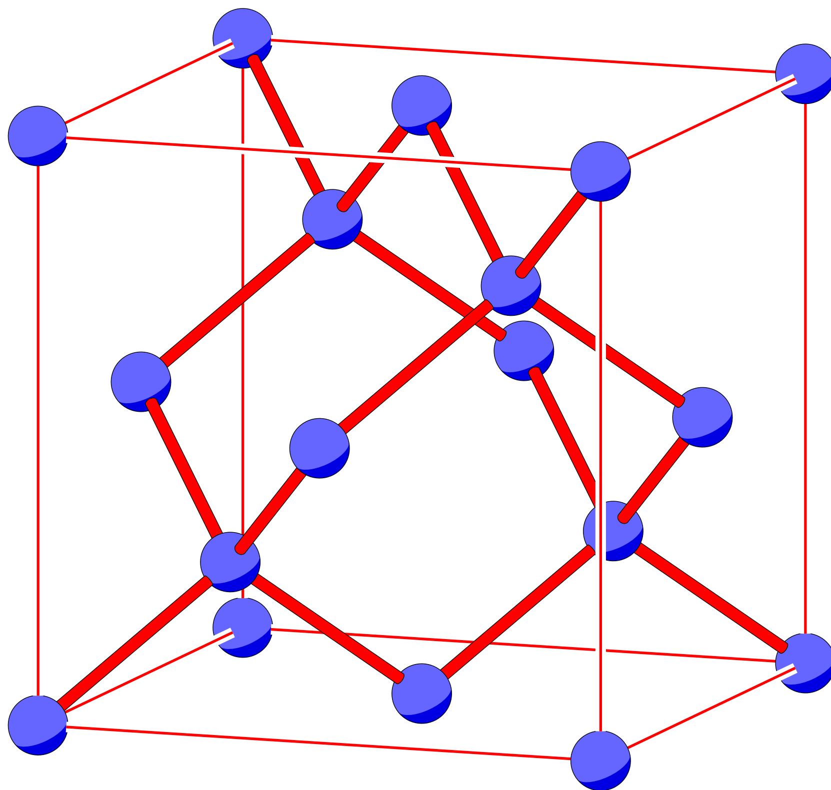

Figure 7: A unit cell of Si, which has a diamond structure.

were proposed. Abukawa *et al.* proposed a trimer model of "milk stool" structure obtained from x-ray photoelectron diffraction study[20] and the same result was obtained using scanning tunneling microscopy[21]. Woicik *et al.*, using back-reflection x-ray standing waves and surface extended x-ray absorption fine structure, support the milk stool model, too[22]. More recently, x-ray diffraction data was obtained in favor of Abukawa *et al.*'s model[23]. Nakatani *et al.* had difficulty in determining the structure of the system thoroughly from the data presented because the information concerning the lateral adsorption site was insufficient. However, with further work they were able to support the T_4 model over the H_3 model, but no detailed analysis

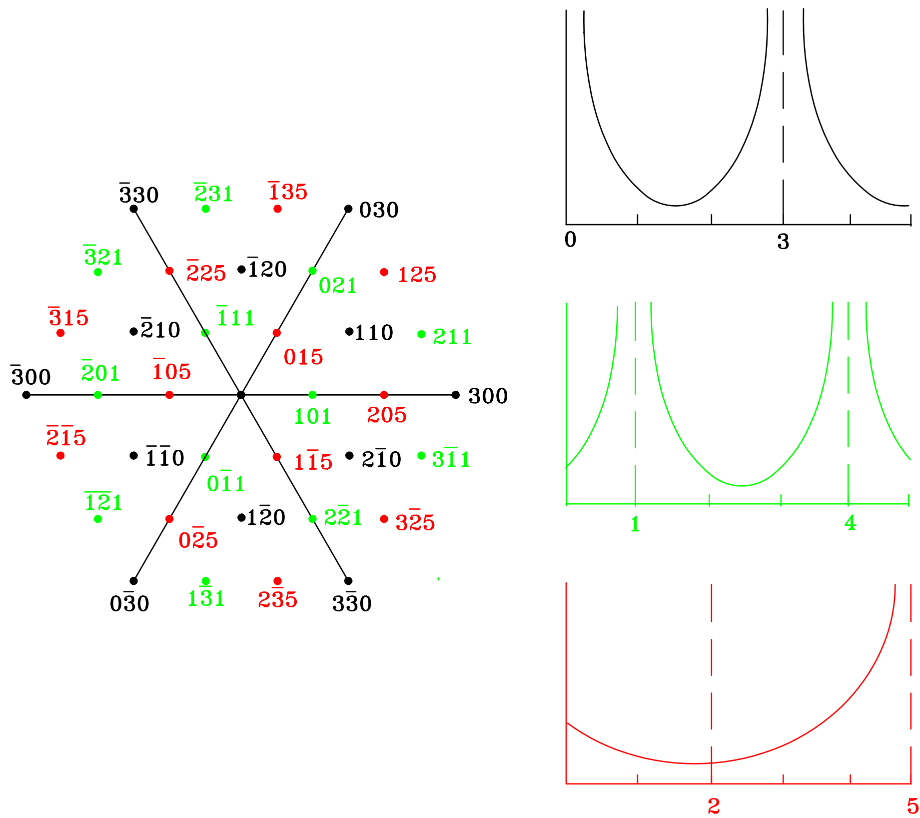

Figure 8: Bragg peaks of Si in reciprocal space and CTRs.

was given with it[24].

In this work we investigated the detailed structures of a trimer and Si substrate below it using *in-situ* x-ray diffraction. A wide range of reciprocal space was probed to obtain information regarding lateral and vertical displacements of each atom. A trimer model was confirmed by the Patterson function and the structural properties of Sb and Si are presented.

3.3 Results and discussion

X-ray measurements were done with the five-circle diffractometer combined with the molecular beam epitaxy (MBE) chamber[25](Fig. 9) on beamline X16A of Na-

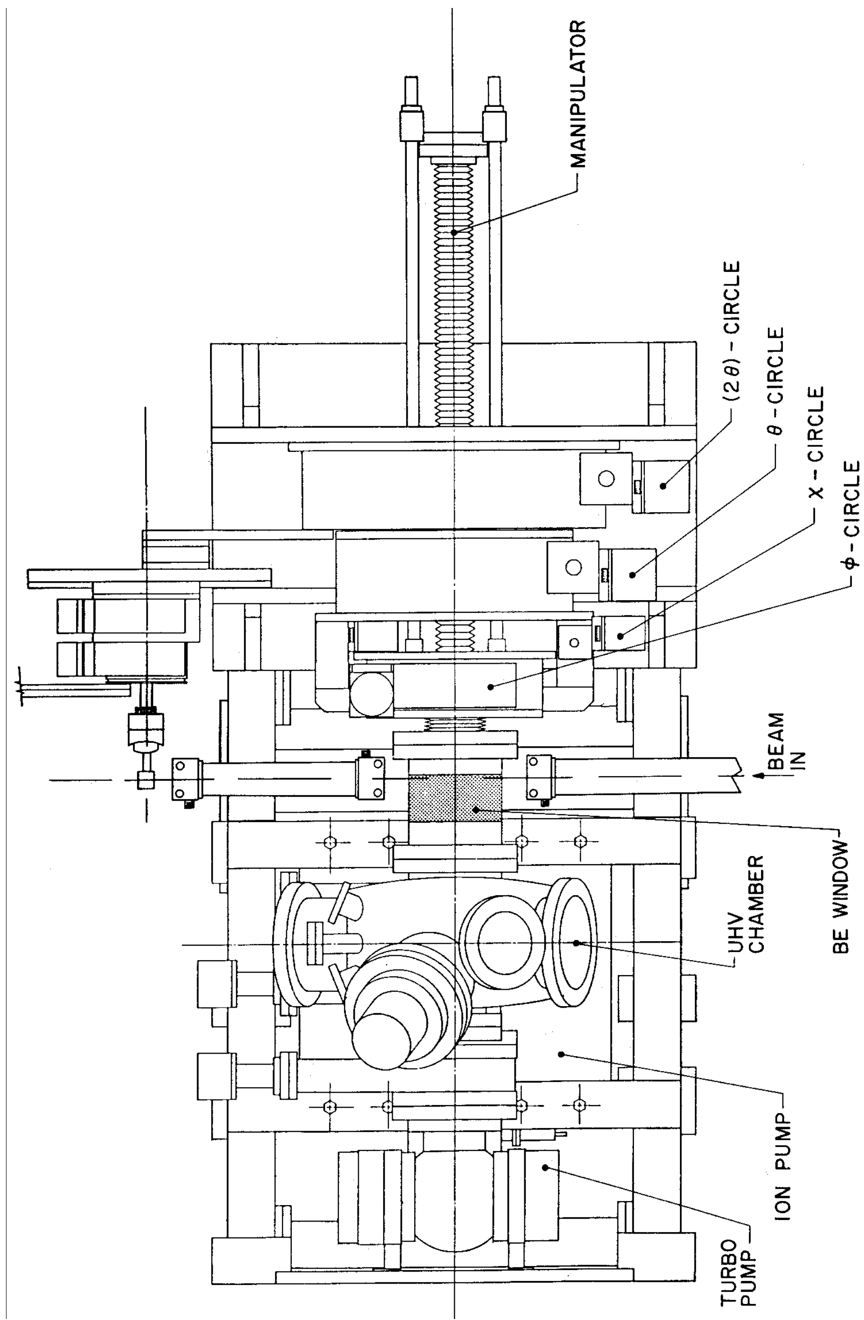

Figure 9: UHV chamber installed in X16A at NSLS.

tional Synchrotron Light Source at Brookhaven National Laboratory. Two Si(111) monochromator crystals were used to select 1.12 Å wavelength x rays. The sample was mounted inside the MBE chamber with the center of its face at the intersection of the diffractometer axes. A position sensitive detector was used with a 2 mm × 10 mm slit, but no analyzer was used. The hexagonal unit cell was chosen so that $a = b = 3.939$ Å and a, b were parallel with $[0\bar{1}1]$ and $[\bar{1}10]$, respectively. This coordinate system was used for indexing the x-ray diffraction data.

In the MBE chamber, a clean Si(111) (7×7) reconstruction was prepared by flashing the Si sample prior to Sb deposition. The (7×7) reconstruction was confirmed by measuring the 1/7th order in-plane peak. Sb was evaporated from a Knudsen cell and the 1/7th order in-plane peak disappeared as Sb was adsorbed on the clean Si(111) surface. The appearance of a 1/3rd order in-plane peak assured that the $(\sqrt{3}\times\sqrt{3})$ structure was rendered. While watching the intensity of the 1/3rd order peak (1/3, 1/3, 0.2) the preparation conditions, i.e., dose rate and sample temperature, were optimized for maximum intensity. It was found best to maintain dosing during cooling of the sample from ~ 600 °C to ~ 400°C and only cease dosing after that. The reconstructed surface stayed uncontaminated over the time scale of measurement with our base pressure $< 2\times10^{-10}$ Torr. For each data point, a scan of diffractometer angle θ was done such that the integrated intensity could be obtained by subtracting the background intensity[26]. Data were collected along the surface normal direction for three fractional-order and three integer-order rods. Fractional-order in-plane peaks were measured to calculate the Patterson function. For reliability of data, measurements were repeated for the symmetry equivalent positions and the integrated intensity was averaged over each symmetry equivalent data point.

Shown in Fig. 10 is a Patterson function[27, 28] obtained from the fractional-order in-plane peaks data set resulting from the $(\sqrt{3}\times\sqrt{3})$ surface reconstruction. The six

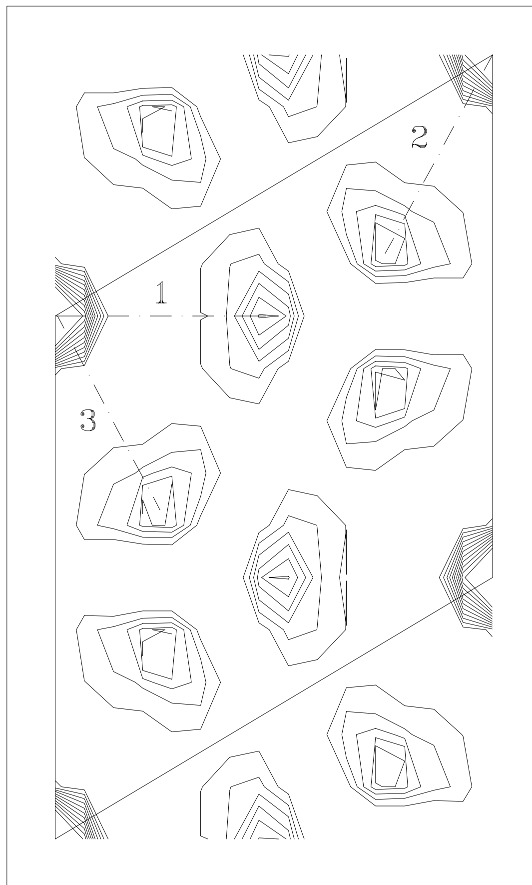

Figure 10: Patterson function of Sb $(\sqrt{3} \times \sqrt{3})$ structure on Si(111). Peaks are identified with numbers corresponding to the inter-atomic vectors between Sb shown in Fig. 11.

peaks in the Patterson function are predominantly Sb-Sb inter-atomic vectors in the surface reconstruction, consistent with a simple triangular arrangement of heavy Sb atoms, such as exists in the "milk stool" trimer model[20]. This is one of the clearest evidences of a trimer obtained from x-ray diffraction data. Therefore, we started our fitting model with one trimer of Sb atoms in the $(\sqrt{3} \times \sqrt{3})$ unit cell (Fig. 11). The numbered peaks in the Patterson function are associated with the inter-atomic vectors labeled in Fig. 11. The location of the center of the trimer is not determined

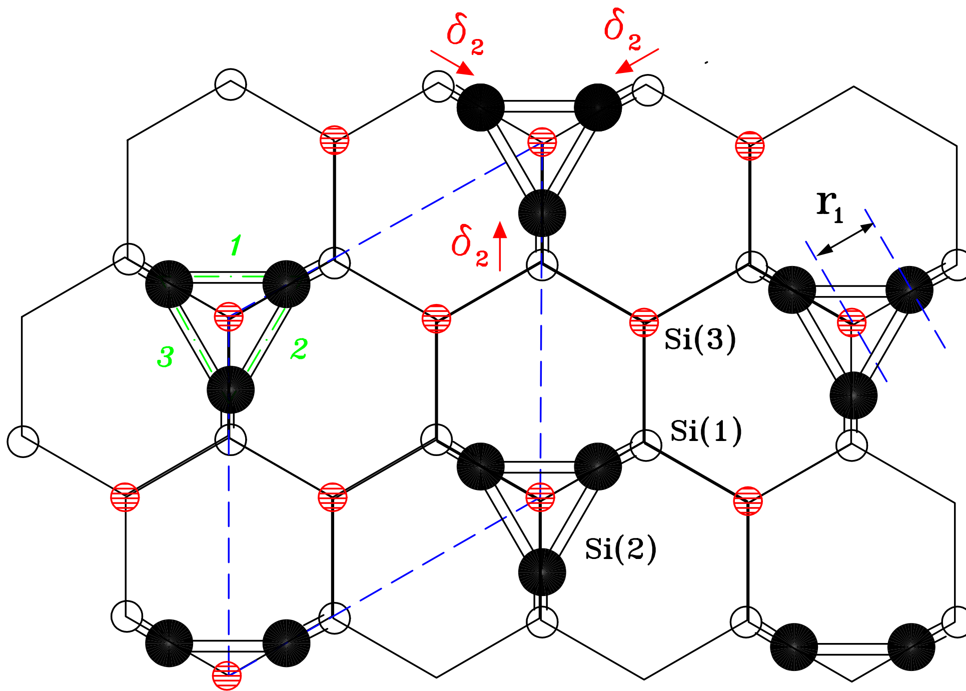

Figure 11: $(\sqrt{3}\times\sqrt{3})$ surface reconstruction of Sb on Si(111). Solid, hatched and hollow circles represent Sb, the first layer and the second layer of Si atoms, respectively. Lateral displacements from the ideal positions for the first layer of Si atoms are shown. d_{12} for Sb atoms is a absolute distance, not a displacement. Inter-atomic vectors between Sb are also shown corresponding to six peaks in the Patterson function.

from the Patterson, and both T_4 and H_3 sites are possible while maintaining the full surface symmetry. Our fit was in favor of a T_4 site with $\chi^2 = 3$ compared with $\chi^2 = 12$ in the case of a H_3 site, which is in agreement with the result obtained in Ref. 23.

In Ref. [21], Mårtensson *et al.* calculated the displacements of Sb and surface layers of Si atoms of the fully relaxed trimer structure through minimization of the Hellmann-Feynman forces at T = 0. Their results are listed in Table 1. In their calculation, they obtained the same displacements for all the atoms in the second(third) Si layers and all three layers were displaced downwards with respect to their ideal

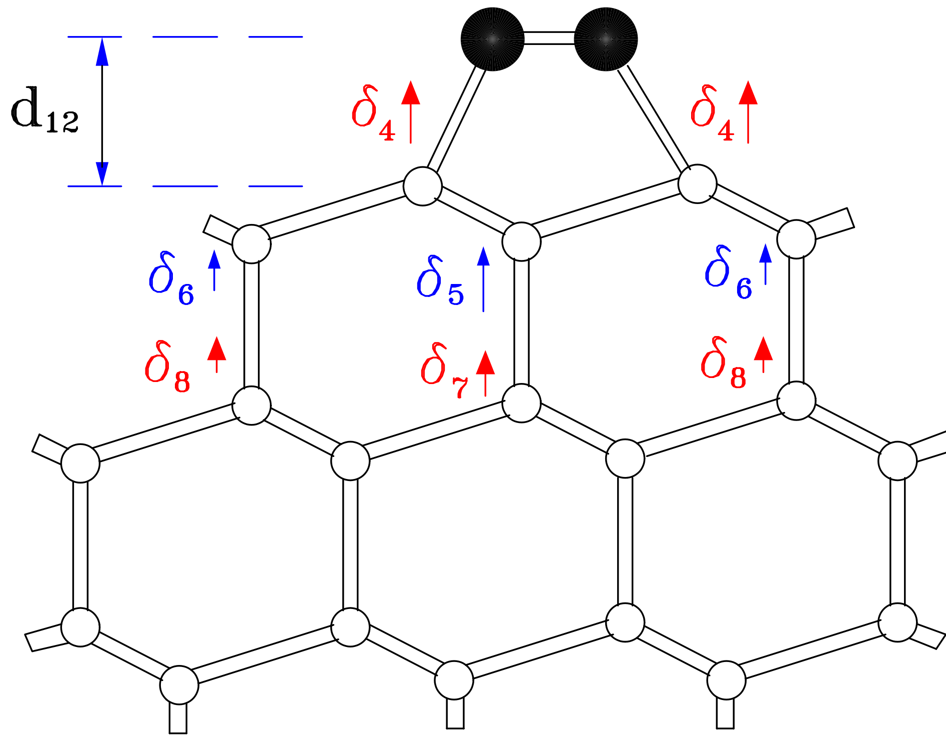

Figure 12: Side view of Sb adsorbed Si(111). Vertical displacement vectors are shown for the first three layers of Si near surface.

positions. The distance between the first and second layers of Si was d_{23} = 0.874 Å, that between the second and third d_{34} = 2.411 Å. The second and third layers of Si atoms each have two symmetry-inequivalent atom positions. Fig. 11 shows these sites in the second layer, Si(2), directly below the Sb trimer, and Si(3). Symmetry prevents lateral displacements of these atoms, but their vertical displacements do not need to be the same amount or even in the same direction. So, for the second(third) layer of Si atoms two independent parameters $\delta_5, \delta_6(\delta_7, \delta_8)$ were used for vertical displacements in our fitting model as shown in Fig. 12. Previous experimental results from Ref. 23 and our results are shown next to Mårtensson *et al.*'s in Table 1. It turned out that the displacements of δ_4 and δ_7 of Si atoms were upward and $\delta_5, \delta_6, \delta_8$ downward, with

Table 1: Displacement parameters used for a least-squares fit. Also shown are thermal vibration amplitudes $\sigma = \sqrt{<u^2>}$ for Sb, the first three layers near surface, Si(S), and bulk Si below three layers, Si(B). Numbers are all in Å units.

	Our work	Ref.[21]	Ref. [23]
r_1	1.688 ± 0.003	1.63	1.63
d_{12}	2.437 ± 0.017	2.51	2.63
δ_2	0.123 ± 0.014	0.06	(-0.18)
δ_4	0.048 ± 0.009	-0.07	·
δ_5	-0.127 ± 0.030	-0.16	·
δ_6	-0.028 ± 0.017	-0.16	·
δ_7	0.027 ± 0.020	-0.10	·
δ_8	-0.011 ± 0.008	-0.10	·
σ_{Sb}	0.25 ± 0.007	·	·
σ_{Si}(S)	0.15 ± 0.007	·	·
σ_{Si}(B)	0.08	·	·

d_{23} = 0.918 Å and d_{34} = 2.266 Å. With all these displacement parameters, thermal vibration amplitudes of atoms were included in our fitting model and their values are shown Table 1. In general, the thermal vibration amplitude of surface atoms is bigger in the surface normal direction than in the surface parallel direction, but an anisotropic thermal vibration amplitude in our fitting model didn't make any noticeable change in the fit. Therefore, we assumed isotropic thermal vibration amplitudes for all atoms. Our result of thermal vibration amplitude, $\sigma = 0.25$ Å, for Sb is a large value but also comparable with those obtained from other cases such as 0.12 Å for Si on Si(111) (2× 1) and 0.16 Å for Sb on Si(100)[29, 30].

Fig. 13 shows our experimental results and fits of the integrated intensities along three fractional-order rods and three integer-order rods, and Fig. 14 for the fractional-orders alone. The bond lengths between Sb-Sb, Sb-Si and Si-Si are listed in Table 2. Lateral and vertical displacements of Sb adatoms as well as the first three layers of Si atoms were taken into account. The bond length 2.92 Å between Sb-Sb on Si(111)

Table 2: Bond lengths between atoms near surface in Å. Numbering of Si atoms is shown in Fig. 11.

	Our work	Ref.[21]	Ref.[23]
Sb-Sb	2.92 ± 0.01	2.82	2.82
Sb-Si	2.47 ± 0.04	(2.57)	2.74
Si(1)-Si(2)	2.30 ± 0.05	·	·
Si(1)-Si(3)	2.44 ± 0.05	·	·

is a bit larger than the previous determination [23].

There now exist multiple experimental and theoretical determinations of the Sb-Sb bond length on both Si(111), where a trimer is formed, and on Si(100) with a dimer. These are summarized in Table 3. The covalent bonding is very different between the two cases, with 60° angle in the trimer and approximately 90° in the dimer. A corresponding trend in bond length might be expected by analogy with inorganic compounds of phosphorus in the same chemical group V: the best example we found was compounds of phosphorus and sulfur which formed molecules with analogous structures to the dimer and trimer. In the P_4S_7 molecule, P is in a very similar geometrical position as Sb on Si(100) and has a P-P bond length of 2.33 Å [37]. On the other hand, in the P_4S_3 molecule, P is in a covalently-bonded trimer, like Sb on Si (111), and has a P-P bond length of 2.24 Å [37]. So, the bond length is actually decreasing from dimer to trimer structure. The experimental data for dimer and trimer configurations of Sb (Table 3) do not concur with this apparent trend for P. The almost identical Sb-Sb bond length on Si(100) and Si(111) may be due to metallic behavior, which has been seen in photo emission experiments on Sb/Si(100) [38].

For the integer-order rods, the fit is almost perfect and well describes even the very

Table 3: Previously measured Sb-Sb bond lengths in Å in Si(100) and Si(111) with different techniques.

	Si	Sb-Sb	Ref.
X-ray standing wave	(100)	2.75 ± 0.06	[30]
X-ray standing wave	(100)	2.81 ± 0.09	[31]
SEXAFS	(100)	2.88 ± 0.03	[32]
Ion channeling RBS	(100)	2.80 ± 0.10	[33]
X-ray diffraction	(100)	2.85 ± 0.01	[34]
LDA cluster theory	(100)	2.93 ± 0.05	[35]
LDA slab theory	(100)	2.96	[36]
SEXAFS	(111)	2.87 ± 0.02	[22]
X-ray diffraction	(111)	2.82	[23]
X-ray diffraction	(111)	2.92 ± 0.01	Our work
LDA theory	(111)	2.82	[21]

detailed structures. However, for the fractional-order rods the fit deviates from the data points. Anisotropy of the vibrations was found not to account for the differences; we did not try an anharmonic model, so this remains a possibility. We tried many variations in our model to fit the fractional-order rods. Since the peaks observed along (4/3, 1/3, L) and (5/3, 2/3, L) rods are 3 reciprocal lattice units away from the main peak, one variation we tried was to add more (fractionally occupied) layers of Sb on top of the original model we used. Others were to change the occupancy of the first and second layer of Si atoms or to substitute Sb for Si in the first layer, but none of these attempts improved the result.

In summary, we studied Sb adsorbed Si(111) surface using x-ray diffraction. Through the Patterson function the $(\sqrt{3} \times \sqrt{3})$ reconstruction was clearly identified. Detailed atomic displacements down to the third layer of Si were obtained. Contrary to a previous result, the first and half of the third layer of Si atoms were found to move upwards. Even though the thermal vibration amplitude is anisotropic

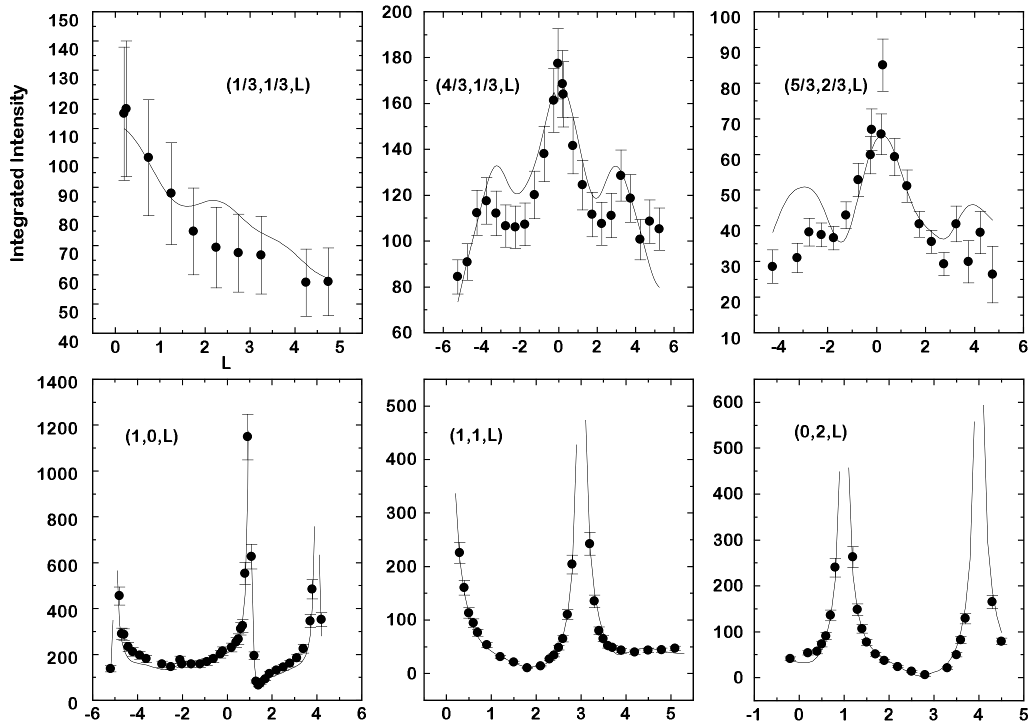

Figure 13: Integrated intensities of fractional and integer order rods.

in general, a least-squares fit with isotropic thermal vibration amplitude model was good enough to explain our experimental results.

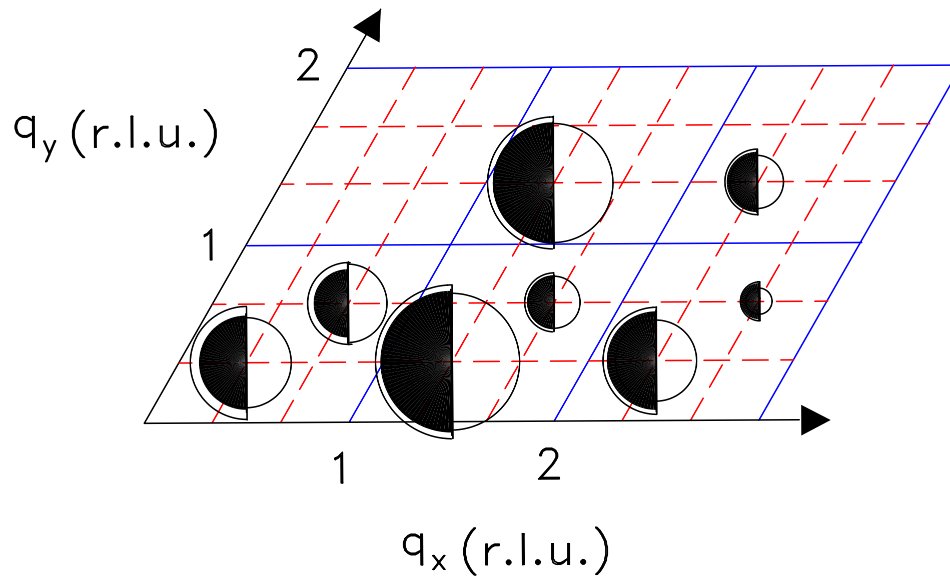

Figure 14: Integrated intensities of fractional-order in-plane peaks. The radii of solid and hollow semi circles are proportional to measured and calculated integrated intensities, respectively. Experimental errors are represented as outer shells of solid circles.

Chapter IV. Strain analysis of GaN thin films

4.1 Introduction

GaN is a compound semiconductor with an Wurtzite structure (Fig. 15) and has a wide band gap of 3.4 eV. A Wurtzite structure is commonly observed for GaN, AlN and InN, but each can also crystallize in a metastable zincblende structure[39]. By alloying with Al or In, the energy band gap can be varied between 1.9 eV and 6.2 eV ranging from blue to ultra violet region. As wide band gap materials have recently drawn much attention with increasing demand of short wave length optical devices, high power and high temperature electronic devices, much effort has been made to grow high quality epitaxial films and to understand the properties of these materials[40, 41]. The physical properties of III-nitrides are summarized in Table 4.

Most substrates commonly used to grow GaN epitaxial layers such as sapphire and SiC have such a sizable lattice mismatch with GaN that introduction of a AlN buffer layer was found to be crucial to improve the quality of GaN film[42, 43]. Since the strain of GaN film is strongly affected by AlN buffer layer, it is important to understand the effect of AlN on the physical properties of GaN. Compared with the amount of work on other properties of III-nitrides, however, there has been little work on the strain of III-nitride thin films[44, 46].

As we mentioned in the earlier chapter, there are many ways of studying strain of materials. In the previous chapter, we showed how we could measure the strain of surface atoms and adsorbates on an atomic scale using the surface x-ray diffraction technique. With this kind of approach, we were able to observe how strain propagates into a bulk substrate, too. Now we move on to another approach of strain analysis in macroscopic scale. For a clean surface or one with a few monolayers of adsorbate on it, it is possible to pindown the positions of each atom during strain analysis.

From Ref.[40]

Table 4: Physical parameters of III-nitrides and sapphire

(a)GaN		
Wurtzite polytype :		
Band gap	E_g (200 K) = 3.39 eV	E_g (1.6 K) = 3.50 eV
Temperature coefficient	dE_g/dT = -6.0 x 10^{-4} eV/K	
Pressure coefficient	dE_g/dP=4.2x10^{-3} eV/kbar	
Lattice constants	a = 3.189 Å	c = 5.185 Å
Thermal expansion	$\Delta a/a$ = 5.59 x 10^{-6} K	$\Delta c/c$ = 3.17 x 10^{-6} K
Thermal conductivity	κ = 1.3 W/cm K	
Index of refraction	n (1 eV) = 2.33	n (3.38 eV) = 2.67
Dielectric constants	$\varepsilon_r \approx 9$	$\varepsilon_\infty = 5.35$
Zinc-blende polytype :		
Band gap	E_g (300 K) = 3.2 ~ 3.3 eV	
Lattice constant	a = 4.52 Å	
Index of refraction	n (3 eV) = 2.9	
(b) AlN		
Wurtzite polytype :		
Band gap	E_g (300 K) = 6.2 eV	E_g (5 K) = 6.28 eV
Lattice constants	a = 3.112 Å	c = 4.982 Å
Thermal expansion	$\Delta a/a$ = 4.2 x 10^{-6} K	$\Delta c/c$ = 5.3 x 10^{-6} K
Thermal conductivity	κ = 2 W/cm K	
Index of refraction	n (3 eV) = 2.15 ± 0.05	
Dielectric constants	$\varepsilon_r \approx 8.5 \pm 0.2$	ε_∞ = 4.68 ~ 4.84
Zinc-blende polytype :		
Band gap	E_g (300 K) = 5.11 eV,theory	
Lattice constant	a = 4.38Å	
(c) InN		
Wurtzite polytype :		
Band gap	E_g (300 K) = 1.89 eV	
Temperature coefficient	dE_g/dT = -1.8 x 10^{-4} eV/K	
Lattice constants	a = 3.548 Å	c = 5.760 Å
Thermal expansion	$\Delta a/a \approx$ 4 x 10^{-6} K	$\Delta c/c \approx$ 3 x 10^{-6} K
Thermal conductivity	$\kappa \approx 0.8 \pm 0.2$ W/cm K	
Index of refraction	n = 2.9 ~ 3.05	
Dielectric constants	$\varepsilon_r \approx 15$, estimated	$\varepsilon_\infty = 8.4$
Zinc-blende polytype :		
Band gap	E_g (300 K) = 2.2 eV, theory	
Lattice constant	a = 4.98 Å	
(d) Al_2O_3		
Lattice constants	a = 4.758 Å	c = 12.99 Å
Thermal conductivity	κ = 0.5 W/cm K	
Thermal expansion	$\Delta a/a$ = 7.5 x 10^{-6} K	$\Delta c/c$ = 8.5 x 10^{-6} K

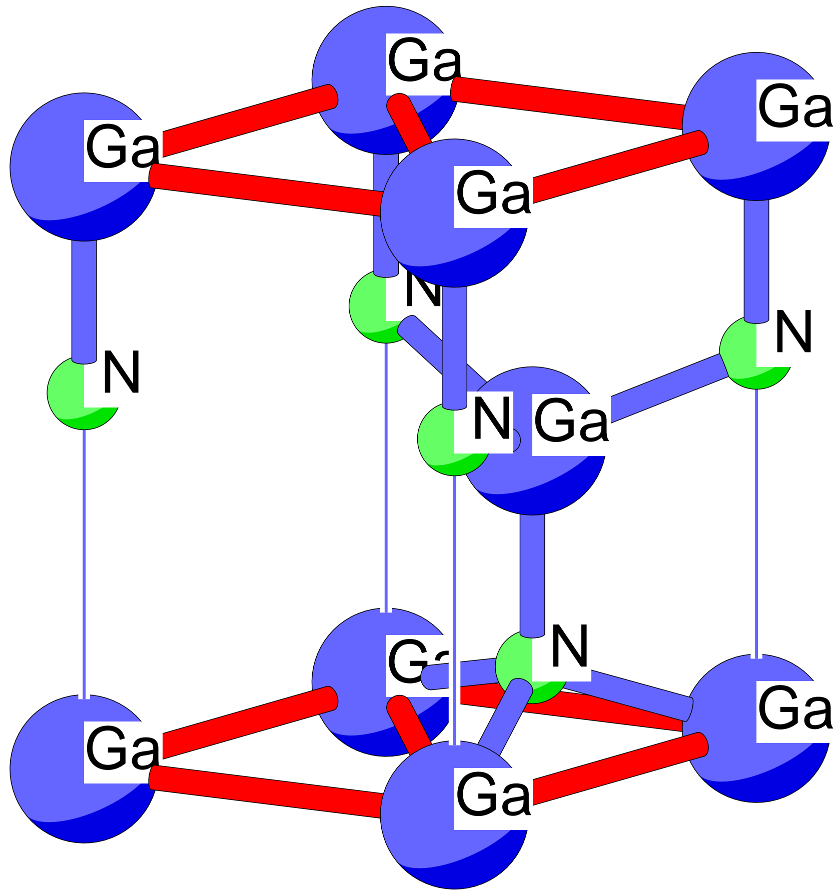

Figure 15: Wurtzite GaN unit cell.

However, in the case of thin films which are thicker than several dozens of Å it is neither easy nor so meaningful to trace down all the positions of each atoms in a film. This is the case when it is more reasonable as well as easier to interpret the results by keeping track of a macroscopic physical quantity. So, we are going to use strain which is derived from the lattice constant of a material of interest as in Eq. (27)

$$\varepsilon = \frac{(a - a_\circ)}{a_\circ} \tag{27}$$

where $a_\circ$ is the lattice constant of the film with no strain at all and a is the actual

lattice constant of the film. From the definition, it is straightforward to evaluate the strain of a film.

4.2 Critical thickness of GaN

Strain of epitaxial films has been extensively studied in many systems such as Si_xGe_{1-x}. However, the prediction of equilibrium theory for the variation of strain as a function of film thickness or the critical thickness was not so accurate, so a kinetic theory was introduced to explain the discrepancy between the experimental results and the theory. It was assumed that the equilibrium theory alone was not enough to explain the results on the strain in Si_xGe_{1-x} system[10]. However, in GaN films grown on sapphire(0001) using AlN buffer layer the kinetic effect was found to be insignificant and it was observed that the equilibrium theory alone was enough to explain strain relaxation behavior. In this chapter, the strain relaxation of GaN will be described using equilibrium theory.

Using Bond's double crystal X-ray method[45] Hiramatsu et al.[46] previously measured the lattice constant of GaN grown by hydride vapor phase epitaxy and metal organic vapor phase epitaxy in the thickness range 0.6 μm to 1200 μm and found that the lattice constant c of GaN decreased with increasing film thickness of GaN. They explained it by strain relaxation mechanism resulting from cracks, assuming that the origin of the stresses was just the difference in the thermal expansion coefficient because their samples were considered to be thick enough to ignore the stress coming from lattice mismatch. Furthermore, only lattice constants near the surface of GaN were measured because the penetration depth was less than the thickness.

In our experiment, GaN samples with smaller thicknesses in the range from 50 Å to 1 μm were grown by molecular beam epitaxy (MBE) on sapphire (0001) using a 32 Å AlN buffer layer at the University of Illinois at Urbana-Champaign. Sapphire

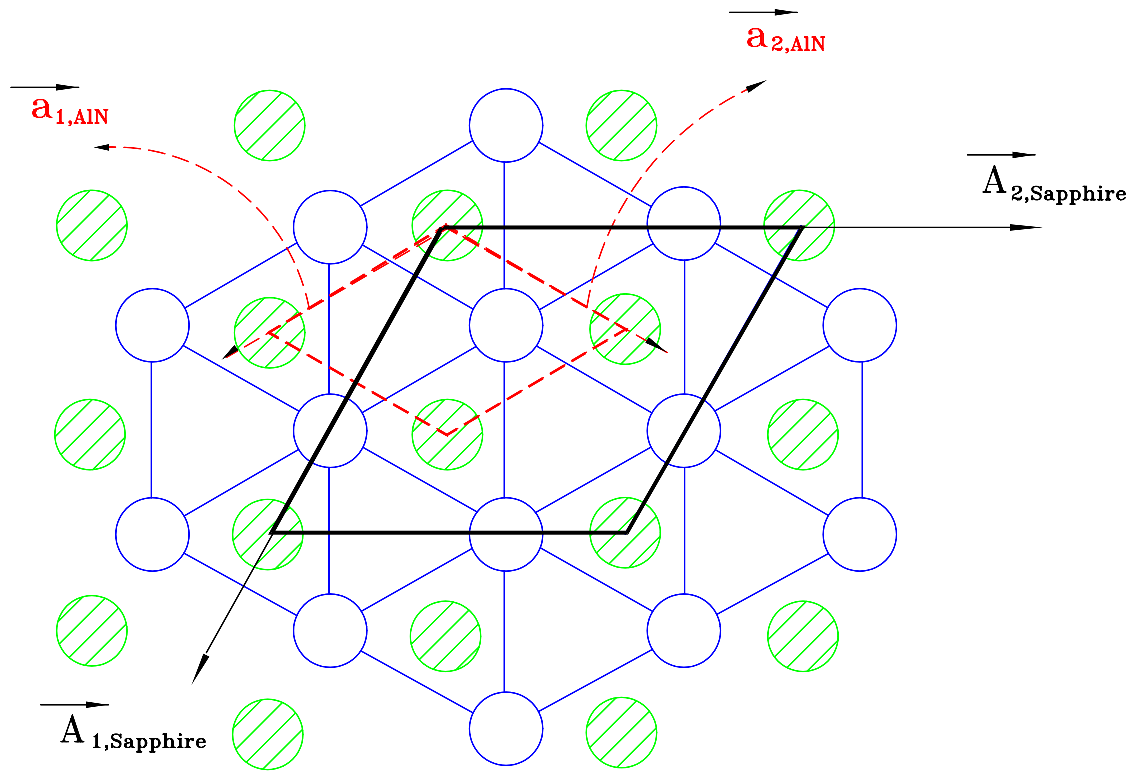

Figure 16: Unit cells of sapphire (0001) and AlN superimposed. Solid line is for sapphire and dashed line for AlN. Open circles and hatched ones represent O in sapphire and Al in AlN, respectively.

substrate preparation consisted of degreasing in successive rinses with trichloroethane, acetone and methanol. Then the substrate was etched in 3:1 $H_2SO_4 : H_3PO_4$. Both rinsing and etching were done at a temperature of 150 °C. After rinsing and etching, the substrate was inserted into the ultra high vacuum chamber. Thermal cleaning at 800 °C resulted in sharp reflection high energy electron diffraction (RHEED) patterns typical of the clean sapphire surface. AlN buffer layer was then grown at a substrate temperature of 550 °C and an Al effusion cell temperature of 1030 °C for 15 minutes. An radio frequency plasma source was used for nitrogen.

We used an AlN buffer layer because its in-plane lattice constant is intermediate,

as used previously[46]. This redistributes the substantial mismatch between two interfaces. The surface unit cell of sapphire (0001) and AlN are shown in Fig. 16. In order to have a workable signal from the thinnest films, the NSLS synchrotron X-ray source was employed to measure lattice constant a and c of GaN films using the least-squares fit method described in Ch. II. A four circle diffractometer featuring *kappa geometry*[47] (Fig. 17) installed at the beam line X16C of National Synchrotron Light Source in the Brookhaven National Laboratory was used for measurement. Our experimental resolution was determined by a 2 mm by 2 mm wide slits in front of a scintillation detector. Our data therefore extend Hiramatsu's work to thinner films. We could estimate the critical thickness of GaN grown on AlN using an equilibrium energetic relationship between the lattice constant a and the film thickness.

Using the relation of $Nd \approx 2\pi/\Delta q$, where Δq is the momentum transfer difference between successive minima of fringes near (002) Bragg peak and Nd is the film thickness, the AlN buffer layer thickness of 32 Å was obtained. The full width at half maximum of (002) rocking curve of AlN was 4.8 arcmin which confirmed that it was epitaxial with the sapphire substrate. On top of the AlN buffer layer, the GaN layer was grown with the substrate temperature of 700 °C and a Ga effusion cell temperature of 910 °C. Using a profilometer trace of a shadow in the film, the thickness of the thickest GaN sample was measured to be 1 μm ± 0.05 μm. This calibration allowed the thickness of the other samples to be derived from their growth time. The thickness of our GaN films was found to range from 50 Å to 1 μm. Using the fringe method we determined the thickness of the 50 Å GaN film to be within ± 5 Å, which assured us that the thickness calibration was accurate for the thinner films, too.

The way we measured the lattice constants was as follows. The same method was used for each sample. (1) Optimize each of the diffractometer angles for N (typically N=10) different Bragg peaks of GaN, (2) build N corresponding reciprocal lattice

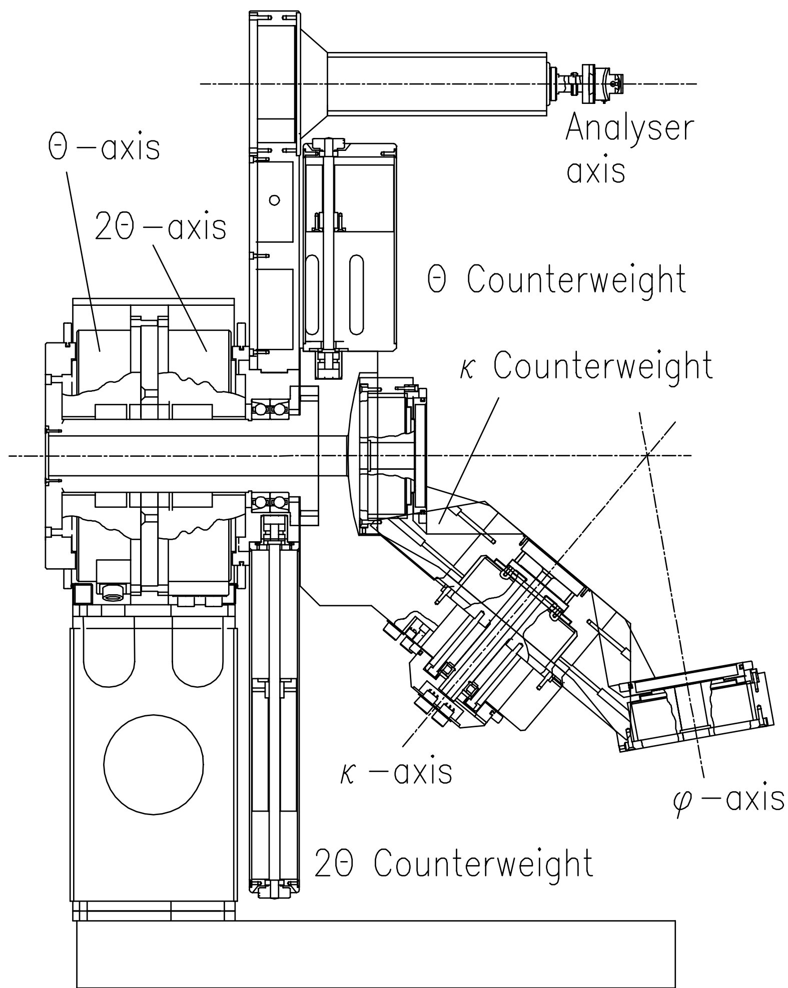

Figure 17: Kappa diffractometer.

vectors from the angles of each Bragg peaks and (3) use a least-squares fit method to get a best fit of lattice which goes through all the Bragg peaks observed. In this way, lattice constant a and c were obtained for each sample. The same method was separately applied to a blank sample containing only the 32 Å AlN buffer layer, in order to measure its lattice constant a, which turned out to be 3.084 Å. This compares with its bulk value 3.112 Å, indicating a partial compression of the buffer layer.

Because of instrumental limitations, the resulting lattice constants will depend

slightly on which Bragg peaks are used in the calculation as well as on their setting accuracy. Since the values were substantially overdetermined, we could use this redundancy to obtain a reliable error estimate. We carefully chose as many peaks as possible isotropically distributed in the reciprocal space. In order to estimate the error connected with the choice of Bragg peaks, we systematically omitted one or more Bragg peaks from the set and repeated the refinement. The resulting error was 0.007 Å for both a and c, including a correction for the systematic (misalignment) error of the diffractometer.

Our results for the lattice constants a and c of the GaN films are plotted in Figs. 18 and 19 as a function of their thickness. They both show a progressive trend away from the bulk GaN lattice constants for thinner films. In the case of the in-plane lattice constant (Fig. 18), the values are found to lie between those of bulk GaN and the AlN buffer layer. It is clear that if the trend towards thinner films were extrapolated slightly, the GaN lattice constant would cross that of the AlN buffer layer. This is the situation that occurs at the critical thickness, h_c of GaN: thinner films would simply have a pseudomorphic epitaxial relationship with the AlN substrate. In order to establish a quantitative estimate of h_c, it is necessary to make a theoretical fit to the data for the trend of lattice constant with thickness, which we explain next.

At thermodynamic equilibrium, misfit dislocations appear at the interface of strained layer heterostructure when the strained layer is thick enough that it is energetically favorable for the mismatch to be accommodated by a combination of elastic strain and interfacial misfit dislocations, rather than by elastic strain alone[48]. Therefore, in the initial stage of growth, when the film is below the critical thickness, GaN is expected to grow pseudomorphically on AlN. Above the critical thickness, the strain begins to relax by spontaneous creation of dislocations at the GaN/AlN interface. Subsequently the lattice constant begins to approach the bulk value as the

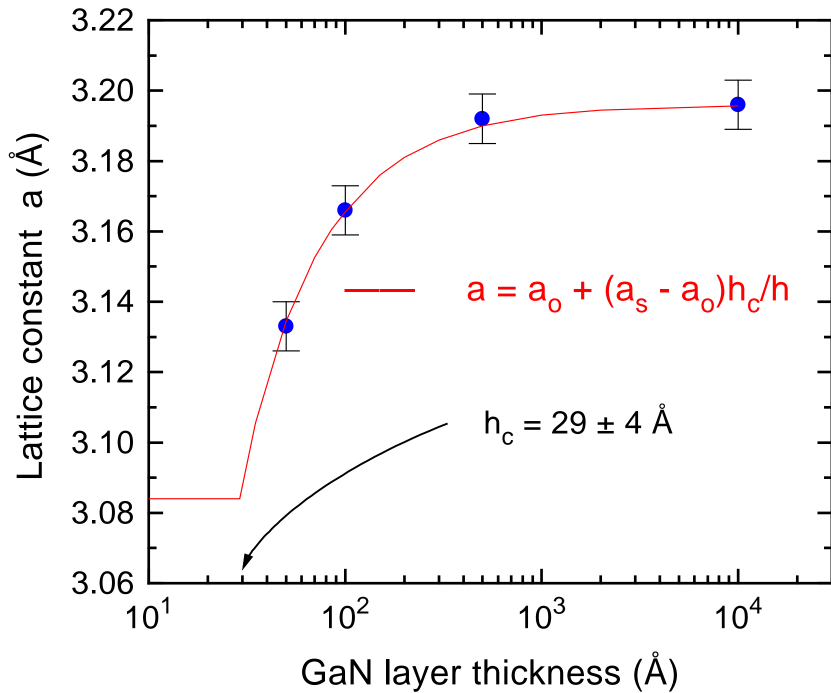

Figure 18: Fit of in-plane lattice constant a as a function of GaN layer thickness.

thickness of GaN increases further.

By observing the trend of the lattice constants as a function of thickness, the thickness at which $a = a_s$, where a_s is the lattice constant of the substrate, which is called the critical thickness h_c, may be extrapolated using a fitting function. In Ch. II, we derived a functional form that was based on Van der Merwe's equilibrium theory[49]. The total energy of an epitaxial film is given by the sum of i) the strain energy which is proportional to square of in-plane strain as well as film thickness and ii) the energy due to dislocations. By assuming that the effective range of the dislocation field is constant, the energy due to dislocations depends on their density alone, which is linearly proportional to in-plane strain. This gave us Eqs. (18) and (19). By differentiating this total energy with respect to the in-plane lattice constant

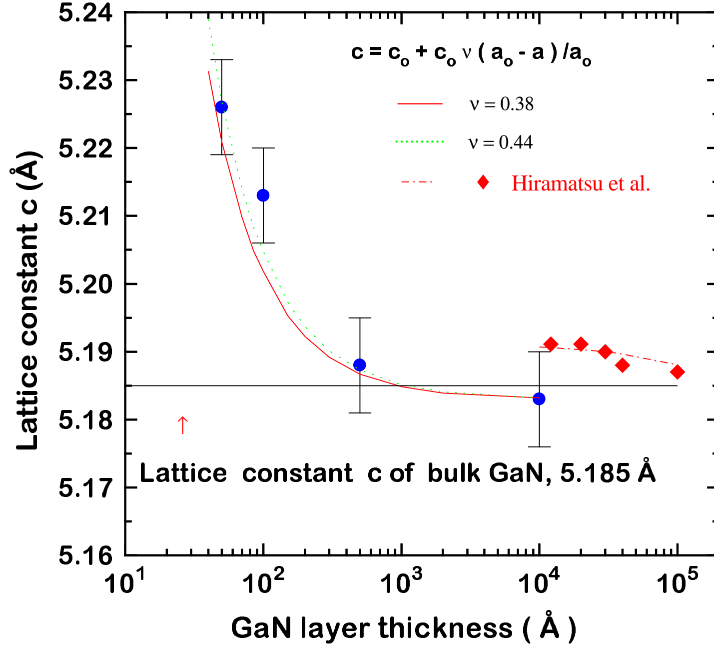

Figure 19: Lattice constant c as a function of GaN layer thickness.

we obtained the theoretical dependence of a on h

$$a = a_\circ + \frac{h_c}{h}(a_s - a_\circ) \tag{28}$$

where a is the in-plane lattice constant of GaN film, h is the thickness of the film, $a_\circ$ is the lattice constant of unstrained GaN, a_s is the lattice constant of the substrate, which we took to be the measured value of 3.084 Å. The independence of the substrate in-plane lattice constant a, of the film grown on top of it was an additional assumption which I will examine further in Ch. V.

h_c= 29 Å ± 4 Å was obtained to fit our data in the entire region of the thickness (Fig. 18) by adjustment of the parameter h_c alone. The resulting fit curve is the solid line through the data points. Using Kasper's[9] energetic correction estimates for the dislocation interactions we obtained a different expression for Eq. (28)[50]. Quantitatively, using the logarithmic correction for the effective range of the dislocation field (Eq. (26)) did not give a significantly different result at the level of accuracy of our data[50].

The critical thickness has been calculated and discussed by many authors. [51, 52] However, there have been many reports[53, 54] on experimental determinations of the critical thickness indicating that coherence apparently persists to thicknesses much greater than that predicted by classical theories. Recently, Fischer et al.[55] reported a new approach in equilibrium theory for strain relaxation in metastable heteroepitaxial semiconductor structures. In this equilibrium theory, they included the elastic interaction between straight misfit dislocations and obtained h_c by setting the excess resolved shear stress required to produce misfit dislocations to zero. According to Fischer et al., the critical thickness is given by

$$\frac{(a_\circ - a_s)}{a_s} = \left(\frac{b\cos\lambda}{2h_c}\right)\left(1 + \left(\frac{1-(\nu/4)}{4\pi(1+\nu)\cos^2\lambda}\right)\ln(h_c/b)\right) \tag{29}$$

where, as before, $a_\circ$ and a_s denote the lattice constants of the fully relaxed film and that of the substrate, respectively. λ is the angle between the Burgers vector and the direction in the interface, normal to the dislocation line. At the interface between GaN and AlN layer, the most commonly observed dislocations are 60 ° dislocations on (0001) plane[56]. Inserting appropriate material parameters, $\lambda = \pi/6$, $\nu = 0.38$ and $b = 3.084$ Å , the calculated critical thickness of GaN is 43.5 Å which is about of the same order of magnitude with our result. Note that λ is $\pi/6$ since both Burger's vector and dislocation line are on the interface. The expansion of c as a result of contraction of a is simply explained by the Poisson ratio, ν, so c can be related to a

from its definition.

$$c = c_\circ + \frac{c_\circ \nu}{a_\circ}(a_\circ - a) \tag{30}$$

where $c_\circ$ is the bulk (relaxed) lattice constant. Shown in Fig. 19 are our data of lattice constant c, the data from Hiramatsu,[46] and the best fit of Eq. (30) with $c_\circ$=5.183 Å and $a(h)$ taken from Eq. (1). The solid line is obtained using $\nu = 0.38$ from Detchprohm et al[46]. We obtained a slightly better fit (dotted curve) with $\nu = 0.44 \pm 0.05$, which can be considered as an experimental estimation of the Poisson ratio for a thin GaN film. Compared with Hiramatsu et al.'s results, the changes in the lattice constant c were very large because our samples were so thin that the effect of lattice mismatch was dominant. However, our result of lattice constant c sits on Hiramatsu's data without any discontinuity. Although the apparent trend in Hiramatsu's data overlies a region where our values appear to be constant, they are still consistent within error. Since the determination of the critical thickness is more sensitive to data obtained for thin samples, this uncertainty of lattice constant in a thicker region does not seriously change the fitting value of the critical thickness.

In summary, synchrotron X-ray diffraction was utilized to measure lattice constants a and c of thin GaN films grown on 32 Å AlN buffer layer by MBE using a least-squares fit method. Due to the lattice mismatch, the changes in lattice constants of GaN films were observed. The critical thickness of GaN was estimated to be 29 Å ± 4 Å. It is noteworthy that an equilibrium energetic argument appears to explain our observations, and gives good quantitative agreement with the predicted h_c. This is not the case in other systems, such as Ge_xSi_{1-x}, where critical thicknesses ten times the equilibrium value are found, and kinetic models are needed to explain the phenomenon[10].

4.3 Effect of buffer layer relaxation on the critical thickness

In the previous section, we investigated the strain relaxation of GaN grown on sapphire (0001) with a thin AlN buffer layer and explained the result with an equilibrium theory. This analysis was based on one of our assumption of an inert AlN buffer layer. However, there was a possibility that AlN buffer layer also would have relaxed as the GaN thickness had increased.

Meanwhile, Huang *et al.*[61] have shown that mutual elastic interaction between two thin films can be important especially when the buffer layer is very thin in such a way that the strain transfer between films can occur and a critical thickness can be increased in certain cases. Therefore, we reexamined our previously measured samples for evidence of the change of AlN in-plane lattice constants. A least-squares fit of multiple Bragg peaks was employed to determine a lattice constant[62]. For those samples in which the in-plane lattice constants of GaN and AlN were very close, the reciprocal lattice mapping was employed to unambiguously determine whether the peaks belong to GaN or AlN. In addition to those which had been previously measured, the sample B was newly measured this time.

The in-plane lattice constants of AlN and GaN are listed in Table 5. The sample A has only 32 (Å) of AlN layer with no GaN layer on top of it and all other samples have 32 (Å) of AlN and GaN with different thicknesses. For the sample B and C, the in-plane lattice constants of GaN and AlN in each sample determined from a least-squares fit method were the same within an experimental error. To be sure of pseudomorphic growth, a full reciprocal lattice mapping of the intensity distribution was done and in Fig. 20 shows two clearly separated peaks along l. Using the reciprocal lattice unit of GaN which we chose for the measurements, the peak at (103) is apparently of GaN and the one above it is from AlN. This reciprocal lattice

map clearly shows that the GaN is pseudomorphically grown on AlN, which was not detected in our previous measurement[62]. In Fig. 21, we show an index scan along l direction through (103) peak of the same sample. Again, the two peaks are clearly separated and two Gaussians were used to fit these peaks. With these results, it is apparent that both AlN and GaN have the same value of in-plane lattice constant. For the sample B, in the same way pseudomorphic growth was observed.

For the sample D, GaN dominates over AlN in peak intensity in such a way that it was too difficult to find AlN peaks even though the peak separation was far enough to be resolved. So, again a reciprocal lattice mapping method was used to find AlN peak. In Fig. 22, the GaN peak is dominant and a very weak AlN peak is seen in the edge of the GaN peak. It is clear that the latter peak would not have been detected without reciprocal lattice mapping. With help of reciprocal lattice map, we were able to find AlN peak and index scans through (103) AlN peak were done and shown in Fig. 23. Symmetrically equivalent peaks of AlN were found more and using the least-squares fit method[62] the in-plane lattice constant was obtained. Note that the h, k, l were labeled in Fig. 23 with respect to the AlN reciprocal lattice. Even though the peak is very broad in l direction, as expected for such a thin film, the full width at half maximum is smaller in h, k direction, which gives a good determination

Table 5: Thickness and in-plane lattice constant of GaN and AlN layers in each sample.

Sample	AlN (Å)	GaN (Å)	a_{AlN} (Å)	a_{GaN} (Å)
A	32	·	3.084	·
B	32	25	3.134	3.134
C	32	50	3.142	3.142
D	32	100	3.103	3.174
E	32	500	·	3.192
F	32	10^4	·	3.196

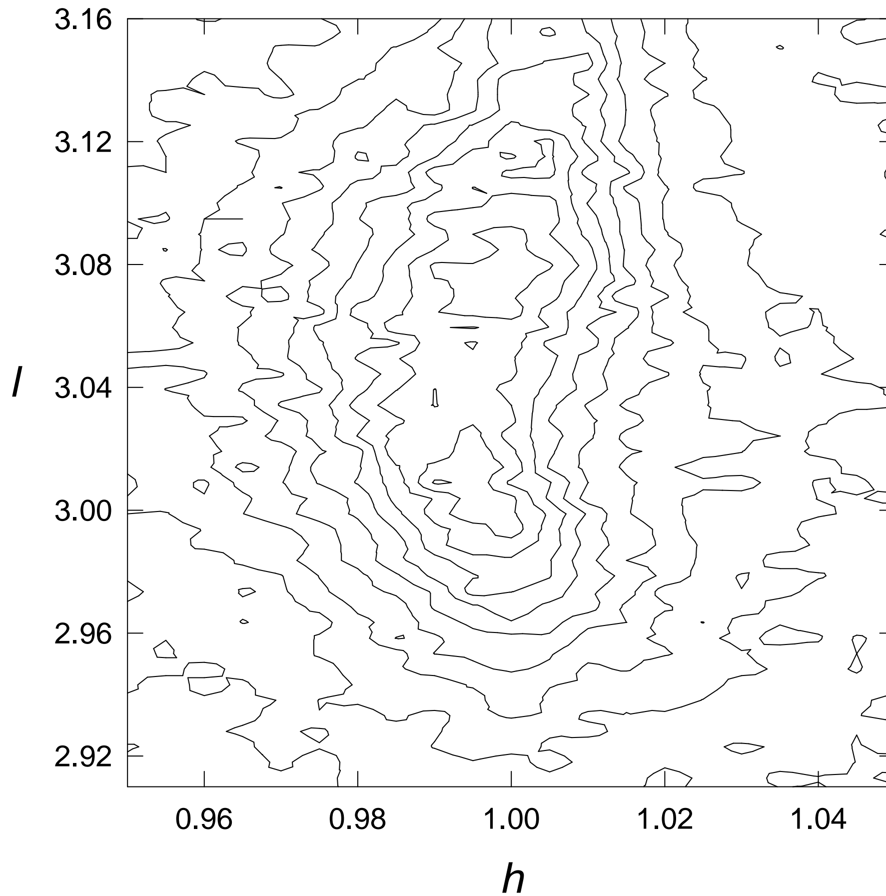

Figure 20: Reciprocal lattice map near (103) Bragg peaks of sample C. The GaN reciprocal lattice unit was used for indexing. Two peaks which has the same h value are clearly visible.

of the in-plane position. The lateral shift between the 2 peaks is clear evidence for non-pseudomorphic growth of GaN. The interesting trend among the samples is that the in-plane lattice constant of AlN increased in the pseudomorphic growth region and then began to decrease as soon as the pseudomorphic growth ended. In other words, after misfit dislocations were introduced, GaN proceeded to relax in the same direction as below the critical thickness, but AlN began to shrink back.

In our sample configuration, 32 (Å) of AlN buffer layer was grown on sapphire

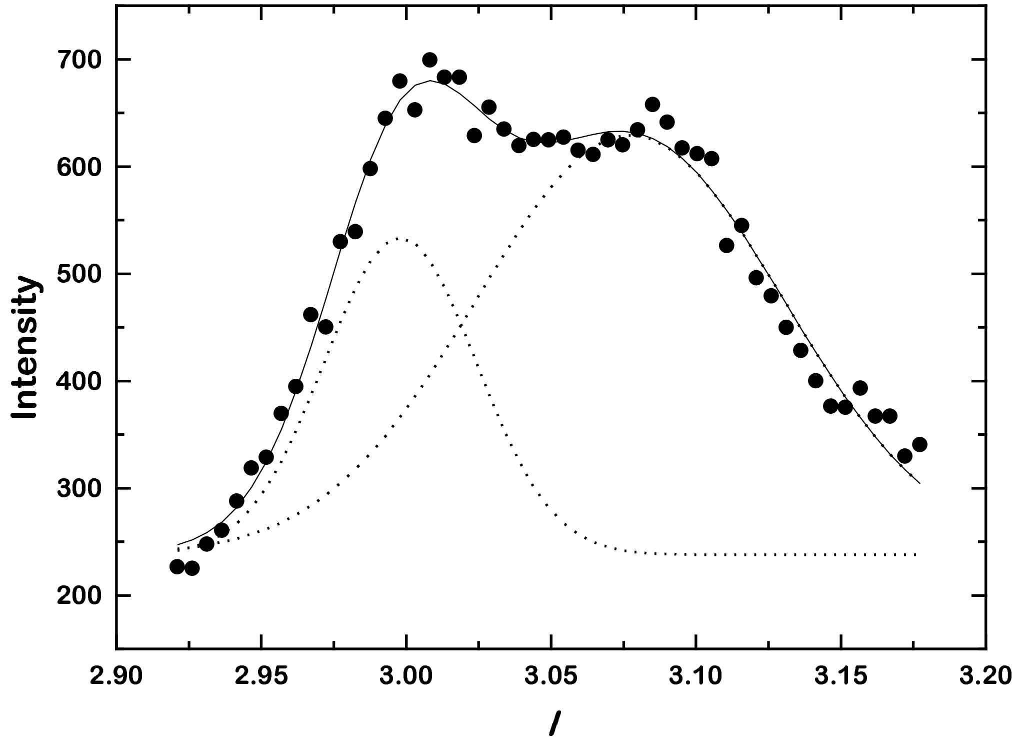

Figure 21: Index scan along *l* direction through (103) peak. Two Gaussians were used to fit AlN and GaN peaks.

substrate followed by the GaN layer. Since the in-plane lattice mismatch between sapphire and AlN is so large that misfit dislocations are introduced at the interface to accommodate the mismatch even at a few layers of AlN. The dislocation densities at sapphire-AlN interface is much higher than at the AlN-GaN interface because of the connection between the lattice mismatch and the dislocation density. With higher dislocation density, the response of AlN layer to the stress coming from sapphire can be assumed to be less important than that to GaN. Therefore, We can make the approximation that AlN and GaN form a *free standing bilayer* and that the only effect

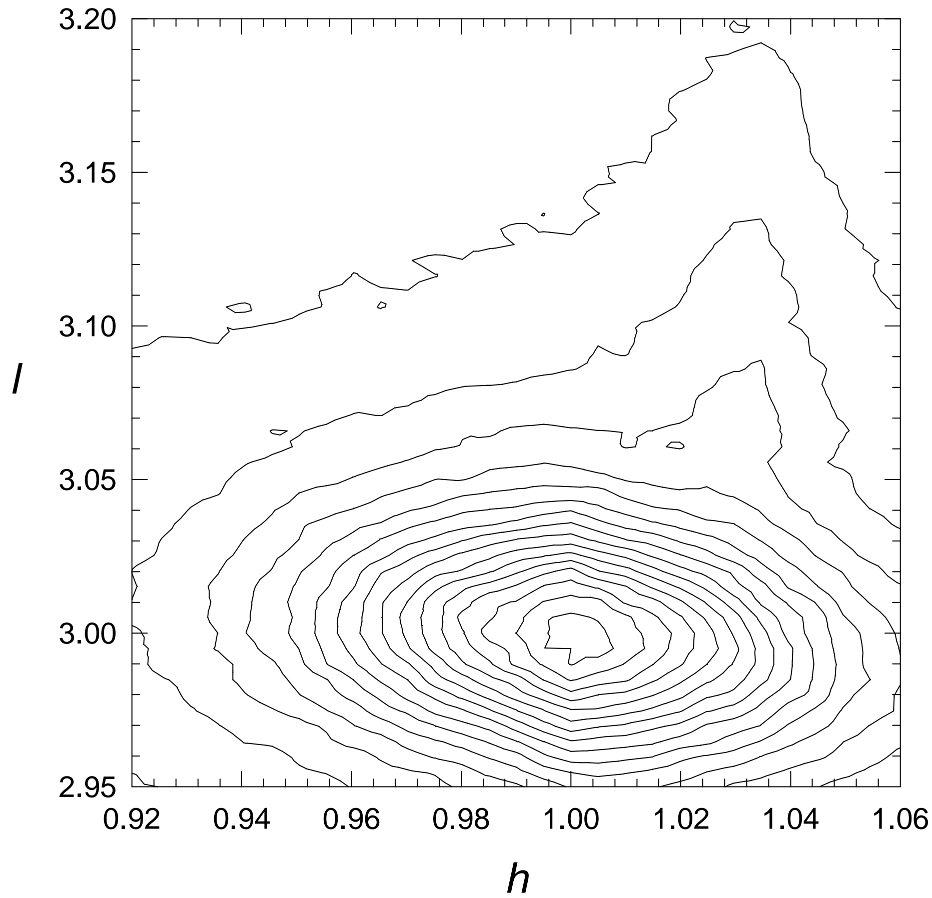

Figure 22: Reciprocal lattice map near (103) Bragg peaks of sample D. The GaN reciprocal lattice unit was used for indexing. A very weak AlN peak is shown on the shoulder of GaN.

of the sapphire substrate is to modify the in-plane lattice constant to the observed value of 3.084 (Å). This value is consistent with a calculation for 32 (Å) of bare AlN on sapphire and the bulk elastic constants of AlN.

Based on this assumption, the total energy of AlN and GaN bilayer in the pseudomorphic limit consists only of elastic strain energy which can be expressed as[61]

$$E = \alpha_1 h_1 (a - a_{10})^2 + \alpha_2 h_2 (a - a_{20})^2 \tag{31}$$

where a is the common in-plane lattice constant of two films. It should be noted

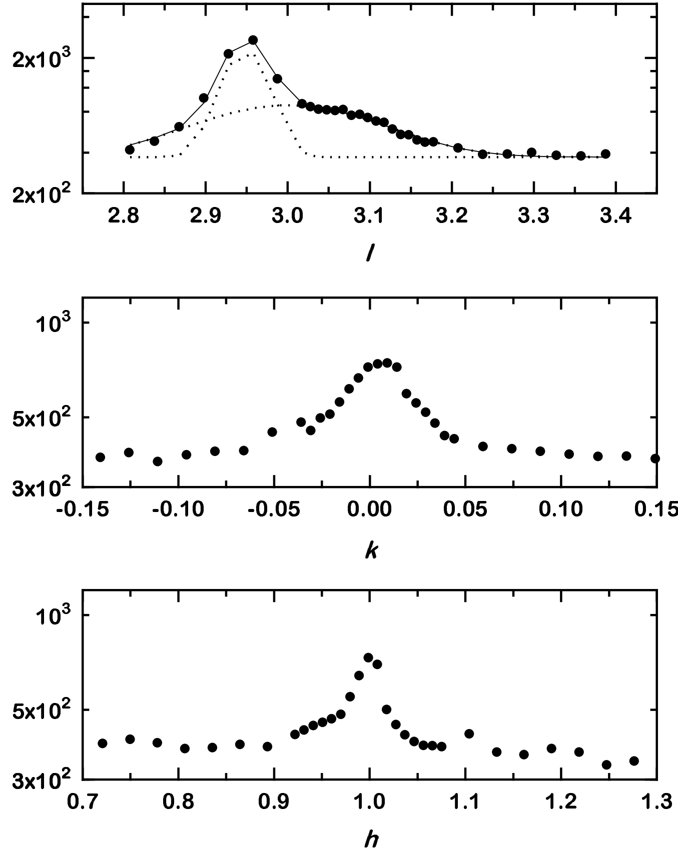

Figure 23: Index scans along in all three directions. A fit of Gaussians was done for l scan. This time the AlN reciprocal lattice unit was used for indexing.

that up to a certain thickness of GaN the lattice mismatch between two films is fully accommodated only by strain so that both films have the same in-plane lattice constant. With an assumption of equilibrium growth of nitride films, the minimization condition, $\partial E/\partial a = 0$, gives us

$$a = \frac{\alpha_1 h_1 a_{10} + \alpha_2 h_2 a_{20}}{\alpha_1 h_1 + \alpha_2 h_2} = \frac{h_1 a_{10} + \frac{\alpha_2}{\alpha_1} h_2 a_{20}}{h_1 + \frac{\alpha_2}{\alpha_1} h_2}. \tag{32}$$

Since only h_2 is a variable, Eq. (32) gives the curve through the data in Fig. 24 where α_2/α_1 was set to 0.8 for the best fit. This value roughly agrees with the ratio of the calculated shear modulus of GaN and AlN, which is 0.88[63, 64]. a_{10}= 3.084 (Å) is

the effective in-plane lattice constant of the 32 (Å) film of AlN and we used a_{20}= 3.196 (Å) for the bulk value of GaN as mentioned above[50].

After GaN reaches the thickness where misfit dislocations are introduced at the interface of two films, in addition to the strain energy in Eq. (31), a new term associated with dislocation energy is introduced[50] in the total energy equation, which is proportional to the density of dislocations,

$$E = \alpha_1 h_1 (a_1 - a_{10})^2 + \alpha_2 h_2 (a_2 - a_{20})^2 + \beta |a_1 - a_2| \tag{33}$$

where a_1 is the in-plane lattice constant of AlN and a_2 is that of GaN. Since AlN behaves as a virtual substrate for GaN and vice versa, the dislocation energy term is proportional to $|a_2 - a_1|$, which is a quantity proportional to the density of dislocations. In our case, a_2 is always larger than a_1, $|a_1 - a_2| = a_2 - a_1$. In the same way as above, the minimization condition gives us

$$\frac{\partial E}{\partial a_1} = 2\alpha_1 h_1 (a_1 - a_{10}) - \beta = 0 \tag{34}$$

$$\frac{\partial E}{\partial a_2} = 2\alpha_2 h_2 (a_2 - a_{20}) + \beta = 0 \tag{35}$$

So,

$$(a_1 - a_{10}) h_1 = \frac{\beta}{2\alpha_1}, \qquad (a_2 - a_{20}) h_2 = -\frac{\beta}{2\alpha_2} \tag{36}$$

An attempt to fit these equations to the lattice constants data is shown as solid curves in Fig. 24. In our experiment, h_1 was not varied, so a_1 would just be constant above the critical thickness according to this theory. This disagrees with observation, so we must revise the theory.

First, we question the assumption that the energy due to the dislocations is only proportional to the dislocation density. The assumption satisfactorily accounts for the h_2 variation of a_2 but incorrectly predicts that a_1 would remain constant since h_1 is fixed at 32 (Å). One improvement is to consider more than one energy term

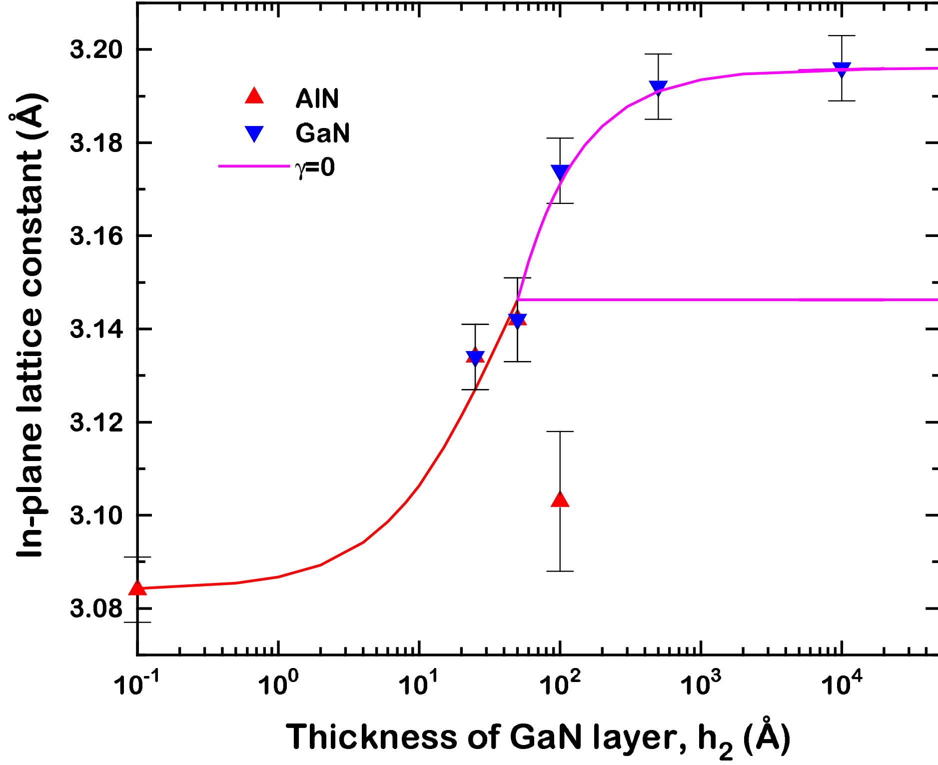

Figure 24: In-plane lattice constants of AlN and GaN films on sapphire (0001) with the fit using a simple theory.

related to dislocations to describe the h_2 dependence of a_1. So, we assumed in a very simple way that the interaction of dislocations must be included. The simplest form of interpretation would be a square of their density. With this higher-order correction, a new form of total energy is given by

$$E = \alpha_1 h_1 (a_1 - a_{10})^2 + \alpha_2 h_2 (a_2 - a_{20})^2 + \beta(a_2 - a_1) + \gamma(a_2 - a_1)^2 \tag{37}$$

and the minimization conditions are

$$\frac{\partial E}{\partial a_1} = 2\alpha_1 h_1 (a_1 - a_{10}) - \beta - 2\gamma(a_2 - a_1) = 0 \tag{38}$$

$$\frac{\partial E}{\partial a_2} = 2\alpha_2 h_2 (a_2 - a_{20}) + \beta + 2\gamma(a_2 - a_1) = 0 \tag{39}$$

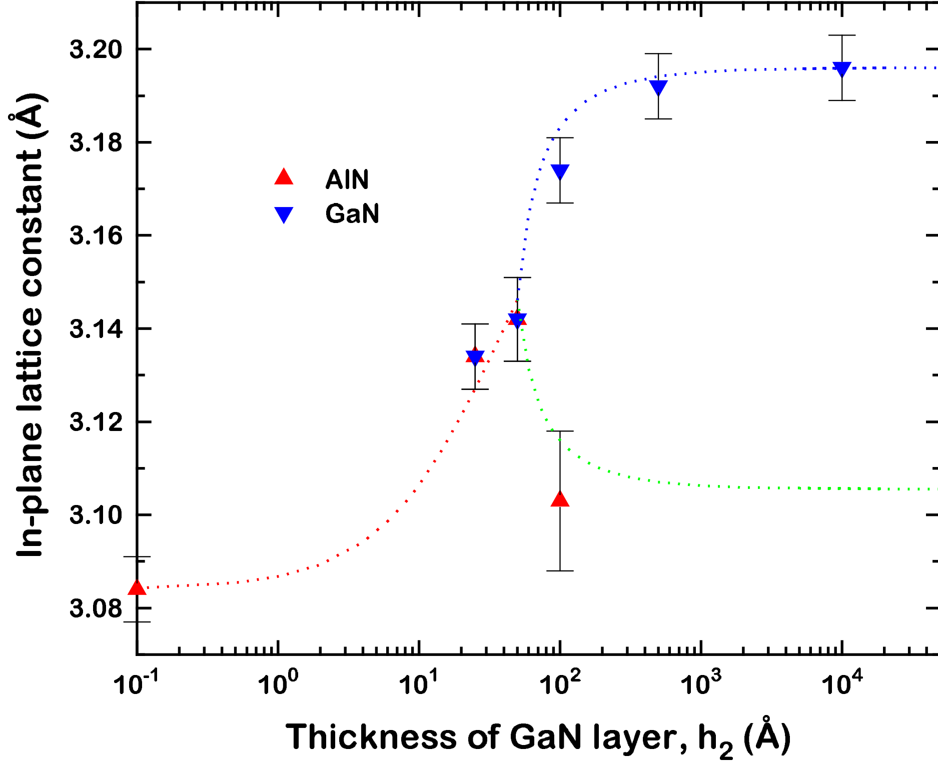

Figure 25: In-plane lattice constants of AlN and GaN films on sapphire (0001) with the fit using an improved theory.

From Eqs. (38) and (39),

$$\begin{pmatrix} a_1 \\ a_2 \end{pmatrix} = \frac{1}{h_1 h_2 + \gamma' h_1 + \epsilon \gamma' h_2} \begin{pmatrix} h_2(h_1 a_{10} + \epsilon\beta' + \epsilon a_{20}\gamma') + \gamma' h_1 a_{10} \\ h_2(\epsilon a_{20}\gamma' + h_1 a_{20}) + \gamma' h_1 a_{10} - h_1 \beta' \end{pmatrix} \tag{40}$$

where $\gamma' = \gamma/\alpha_2$, $\beta' = \beta/(2\alpha_2)$ and we used $\epsilon = \alpha_2/\alpha_1 = 0.8$. Therefore, what we end up with is explicit functional forms of a_1 and a_2 as a function of h_2 with two fitting parameters of γ' and β'. With these modified approach, the h_2 dependence of a_1 can be explained. In Fig. 25, the best fit with γ'=-18 and β'=2.49 is shown along with our data. Since γ' was the coefficient of the interaction of dislocations, the negative sign means that it is energetically less favorable for the system to decrease the density of dislocations above a critical thickness. The change of lattice constant with different

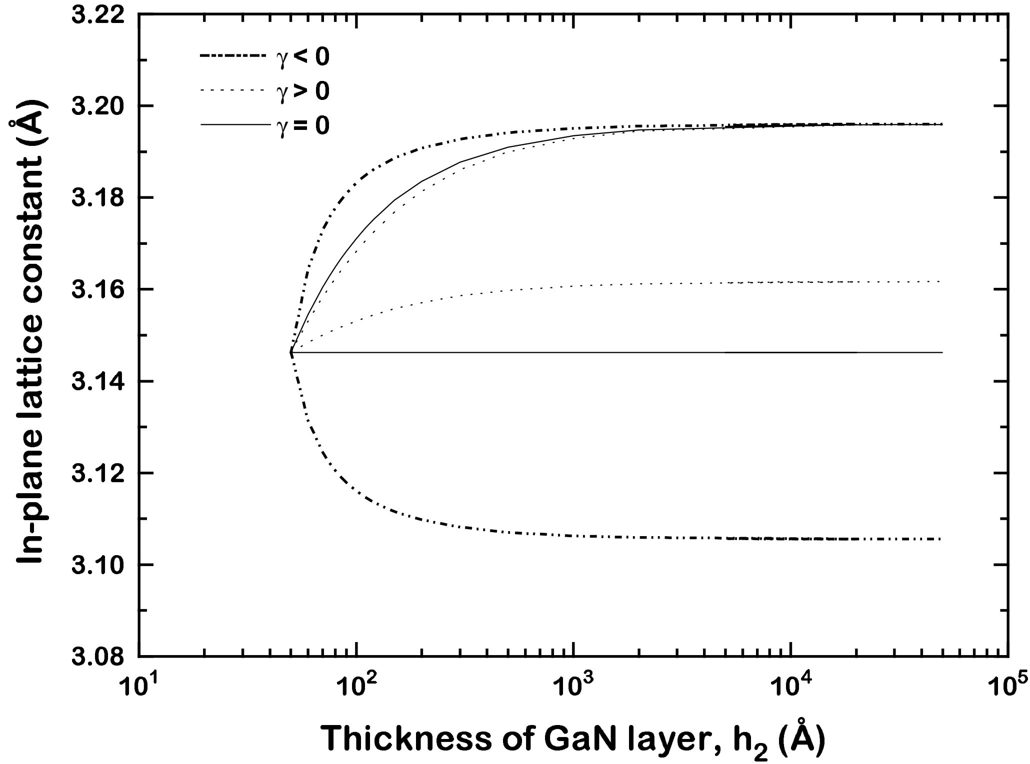

Figure 26: Theoretical description of in-plane lattice constants above the critical thickness with various γ's. This plot corresponds to Eq. (40) with a fixed β'.

values of γ's are shown in Fig. 26. This implies an attractive interaction between the dislocations. In other words, by including that term in the total energy, above a critical thickness the role of dislocations to relieve the lattice mismatch decreases compared with the role of strain.

In summary, the strain of GaN and AlN bilayer on sapphire (0001) is investigated as a function of GaN layer thickness using x-ray diffraction. An assumption of free standing bilayer was made to explain the strain of GaN and AlN. Below the critical thickness, the in-plane lattice constants of both GaN and AlN increased as a function

of GaN thickness predicted by the elastic theory maintaining pseudomorphic configuration. Above the critical thickness, however, the in-plane lattice constants split up and each film relaxed in such a way that the in-plane lattice constant approached their unstrained values.

Chapter V. Effect of AlN buffer layer on the strain relaxation of GaN

5.1 Thin film diffraction of AlN

As we found in the previous chapter, the role of AlN buffer layer on the strain relaxation of GaN is very important. To get a better understanding of AlN buffer layer, we grew thin AlN films on sapphire (0001) with or without GaN film on them and analyzed the strain relaxation of AlN. Preliminarily we studied the interface structure between sapphire and AlN with a scan normal to the surface. 80 Å thick AlN film on sapphire was chosen for this purpose. A scan along (00L) direction was made (Fig. 27) and was fitted using 65 or so alternating Al and N atomic layers. The best fit was obtained with an interface distance parameter of 0.45 Å. The sharp peak at q_z=2.9 ($Å^{-1}$) is a (006) peak of bulk sapphire and all other peaks are typical thin film diffraction fringes, which assures that AlN film is epitaxially well grown in the normal direction, at least. Information about the interface distance is extracted from the asymmetric structure around the bulk sapphire peak. As explained in Fig. 2, an asymmetric feature around a Bragg peak can arise from a variation of the interfacial distance between a film and substrate. In our fitting model, the parameter of $\mathrm{dist_{int}}$ was 0.45 Å. With all other fitting parameters fixed, $\mathrm{dist_{int}}$ was set to four different values and their effects are shown in Fig. 28. This assured that dist_{int} was determined accurately. In the next section, we will show the strain relaxation behavior of AlN using the same method we adopted in the previous chapters.

5.2 Thickness dependence of AlN on the strain of GaN

A series of AlN films with different thicknesses (without GaN on them) were measured to study strain relaxation. The procedures are the same as we described

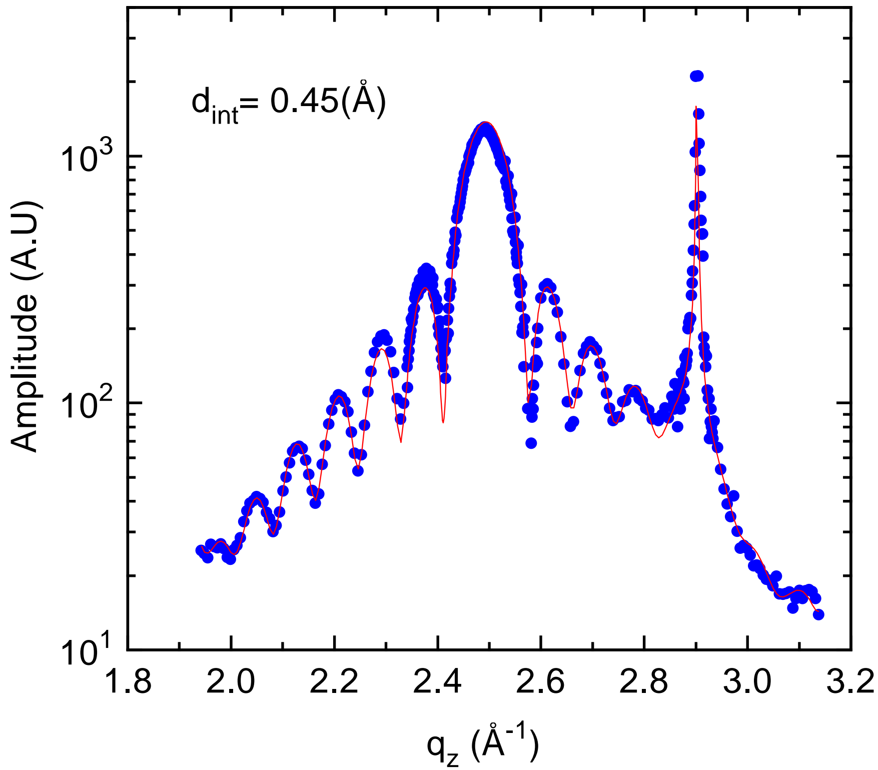

Figure 27: Fit of (00L) rod of 80 Å thick AlN film on sapphire substrate. A model with 65 alternating Al and N layers was used with several layers near the interface allowed to relax. The distance between sapphire and AlN at the interface was set to 0.45 Å.

in the previous chapter. We grew a series of samples of AlN thin films on sapphire (0001) with a thickness ranging from 12 Å to 1530 Å. The in-plane lattice constant of AlN layer was measured by two slightly different methods. The first method was to find at least six (out-of-plane) Bragg peaks and to use a least-squares fit to find the best reciprocal lattice which passed through the measured peak positions as described in Ch. II. With the second method, three symmetric equivalent in-plane (110) peak positions of AlN were used to find the in-plane lattice constant directly since (110) peak position is determined by the in-plane lattice constant alone. This required a grazing incidence geometry and a small out of plane component of momentum

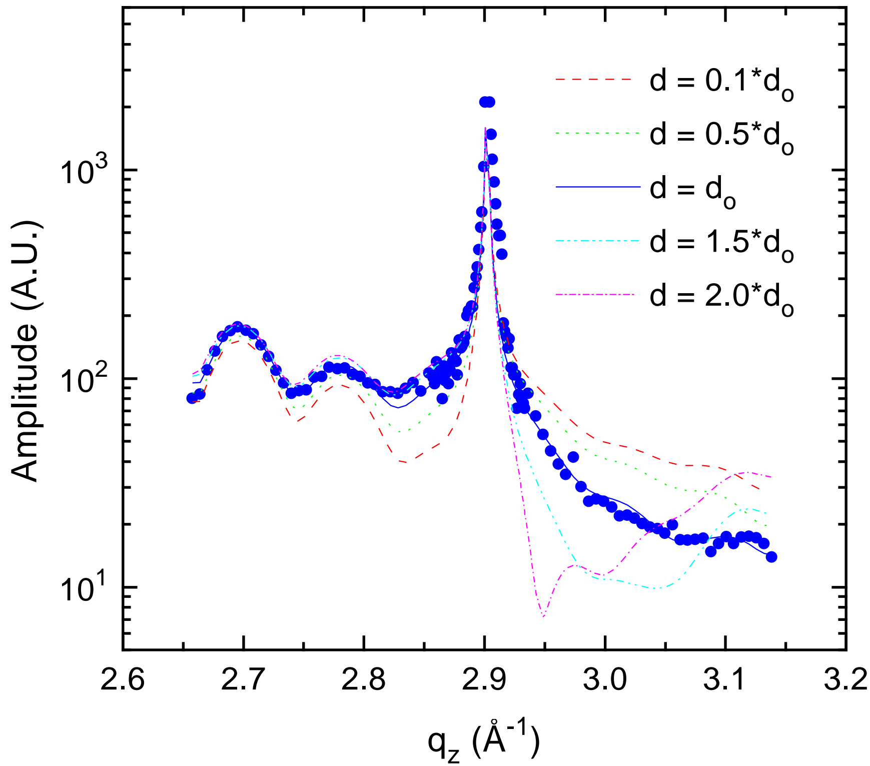

Figure 28: Change of fits with variation of interface distances. The same sample as shown in Fig. 27 with $d_\circ$=0.45 Å.

transfer. Our results for the lattice constant a of the AlN films are plotted in Fig. 29 as a function of their thickness. Since the lattice mismatch between sapphire and AlN is 11.7 %, most of relaxation in AlN layer happens in the first few layers. So, even though our thinnest sample was 12 Å, 83 % of relaxation was already made.

We attempted to fit the data with only one parameter h_c, using Eq. (19). Using the substrate lattice constant $a_s = 2.747$ Å and the lattice constant of the completely relaxed AlN film $a_\circ = 3.112$ Å, the parameter $h_c = 4 \pm 2$ Å was obtained with a least-squares fit method. The fit is not so good as in the case of GaN. It may be related with the fact that the misfit between AlN and sapphire is so big that the elastic theory can't be applied to any longer. Even though we tried to fit our experimental results

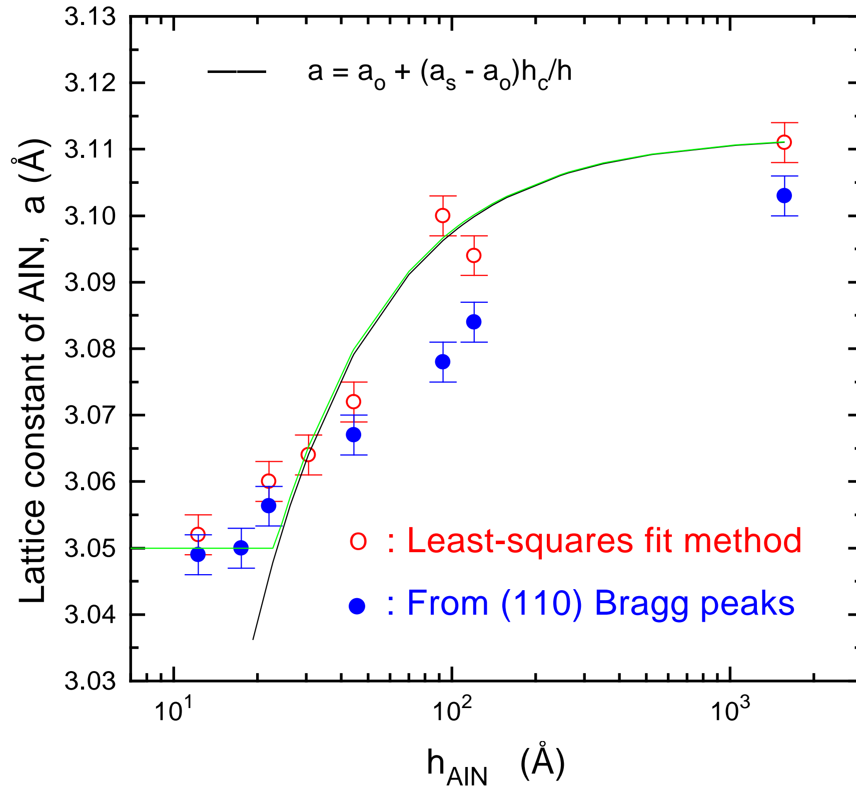

Figure 29: Lattice constant a of a series of AlN layers. $h_c = 4 \pm 2$ Å was used.

with an equilibrium model, it seems that our data follows a little different mechanism of strain relaxation.

We measured in-plane lattice constants of GaN with a fixed thickness with the thickness of AlN buffer layer changed. As shown in Fig. 30, the in-plane lattice constants of GaN decreased as the thickness of AlN increased. This result can be explained as follows. The in-plane lattice constant of AlN is not substantially affected by the thickness of GaN as long as their thicknesses are far above critical thickness and it increases as its thickness increases as shown in Fig. 29. As far as the GaN layer is concerned, if we consider the same behavior for the GaN in-plane lattice constant as described in Eq. (19) except using the in-plane lattice constant of AlN, a_s, as a

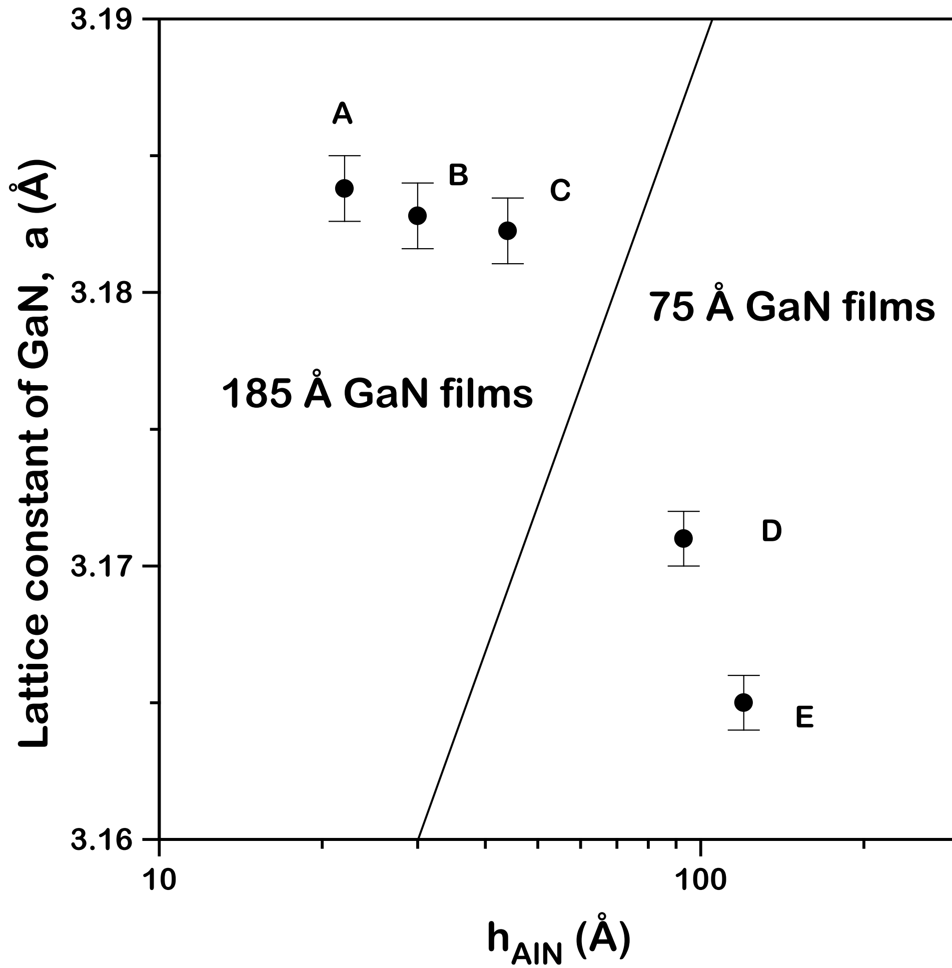

Figure 30: In-plane lattice constant of GaN in samples A through E.

variable then as we increase the AlN thickness the in-plane lattice constant of GaN should decrease.

The in-plane lattice constant decrease of GaN as the thickness of AlN buffer layer increases can be more rigorously explained. In order to explain this, we need to know GaN in-plane lattice constant as a function of its thickness with a series of a different thickness of AlN buffer layer. Since we know Eq. (19) is valid, the only value we need to calculate the dependence is a critical thickness as a function of in-plane lattice

constant of a buffer layer. Since the critical thickness of GaN on AlN buffer layer with a certain value of an in-plane lattice constant can be obtained from equilibrium theory, we can have a set of critical thicknesses as a function of AlN in-plane lattice constant.

Chapter VI. Strain relaxation induced by irradiation in $Si_{1-x}Ge_x$ films

$Si_{1-x}Ge_x$ alloy has been one of the most extensively studied systems in thin film physics due to its physical interest and technological applicability. [65, 66, 67, 68, 69, 70] With growing demand for multilayer structures, the main interest in this area lies in growth of defect free pseudomorphic film, which is highly strained. However, a theoretically predicted critical thickness does not concur with a value determined by experiments for SiGe. Since it is believed that growth of $Si_{1-x}Ge_x$ is so dominated by kinetic effect that the energy of the film is not minimized at each state of growth as a whole. It is well known that an experimentally determined critical thickness of $Si_{1-x}Ge_x$ on Si substrate is much larger than that predicted by equilibrium theory. The region between the equilibrium critical thickness and the experimentally determined critical thickness is therefore metastable[10, 71]. So, if a film is in the metastable regime, even though it is commensurate with the substrate, the film might relax as proper perturbations or excitations are provided such as post-growth annealing or irradiation, which would move the system into the energy minimized state.

The effect of post-growth high temperature thermal annealing on the strain relaxation of metastable $Si_{1-x}Ge_x$ thin films was studied by many people. The reason for this interest is that thermal annealing is routinely done during the device processing and any strain relaxation would cause a dramatic change in the device characteristics. Sardela *et al.*[72] reported that the in-plane lattice relaxation due to post-growth thermal annealing in $Si_{1-x}Ge_x$ on Si(001) as a function of annealing temperature and composition using high resolution reciprocal lattice mapping. In their work, $Si_{1-x}Ge_x$ thin films were grown pseudomorphically and were within the metastable region,

which means the thicknesses were believed to exceed the theoretically predicted critical thickness. Misfit dislocations activated by thermal annealing were introduced so that the Bragg peak became shifted as a result of the relaxation process. A broadening of the peak accompanied with the decrease of the peak intensity was attributed to the increased mosaicity caused by misfit dislocations.

Ion implantation has long been used for doping semiconductors. With its many advantages over other doping methods, it has one shortcoming: it induces defects in the crystal. However, the fact attracted many researchers to investigate irradiation effects on semiconductor materials either to get around the problems of causing defects or to study the strain relaxation induced by irradiation. Many recent works on the strain relaxation by irradiation on $Si_{1-x}Ge_x$ have been done[73, 74, 75, 76, 77, 78, 79, 80, 81]. Typical irradiation effects can be summarized by two things: 1) out-of-plane lattice constant expands due to point defects (such as interstitials) with virtually no change in in-plane lattice constant and 2) recovery of crystal damage by thermal annealing. In contrast, a decrease of out-of-plane lattice constant was also reported by heating up the sample during irradiation[82].

Radiation defects are typically caused by two dominant processes during irradiation; inelastic collisions with electrons and elastic nuclear collisions. Depending on the energy and the mass of the accelerated particles, as well as on the mass and the atomic number of the medium, which of two effects predominates. These defects have a distribution in the solid which is different from that of accelerated ions in the solid, since the position to which the maximum energy is transferred is not where those ions stop. The simplest defect, a Frenkel defect, is produced by the displacement of a lattice atom on to an interstitial site; a vacancy and an interstitial atom are the result. Dislocation type defects can be formed by accumulation of simple defects or as a result of stress caused by unannealed radiation damage. If many lattice atoms are

Table 6: A list of SiGe samples irradiated.

	Film thickness (Å)	Growth temperature (°C)
A	200	500
B	275	550
C	100	500
D	360	450
E	400	500

displaced by accelerated atoms in a small area, the defects area start to overlap each other and form an amorphous zone. For more detailed discussions of ion implantation and radiation damage, see references.[83, 84, 85]

In this work, we aimed at observing the strain relaxation of metastable $Si_{0.7}Ge_{0.3}$ film in the in-plane direction by irradiation. As we mentioned earlier irradiation might allow the system to relax closer to the energy minimized state. In this case, both the macroscopic and microscopic strain relaxation is of interest. Reciprocal lattice mapping (RLM) using x-ray diffraction is among the most powerful methods because of its capability to provide information in two different directions at the same time. The first is the macroscopic uniform strain relaxation which can be measured from the peak shift with respect to the substrate. The other, which can be deduced from the distribution of diffuse scattering near Bragg peak, is the evolution of structural imperfections caused by increased mosaicity or local strain fields. A series of $Si_{0.7}Ge_{0.3}$ films with different thicknesses was grown on Si(001) by vapor phase epitaxy between 450 °C and 550 °C, which are listed in Table 6. According to the previous work, those are roughly in the metastable regime[86, 87]. *In-situ* x-ray measurements during irradiation were done at the beamline X16A of National Synchrotron Light Source at Brookhaven National Laboratory. The irradiation gun

Table 7: Irradiation dose for each SiGe samples. Note that these samples were irradiated with 3 keV He^+ ions except the sample A with 25 keV Ga.

Sample		Total dose (ions/cm^2)
A	1st	8.0×10^{10}
	2nd	3.2×10^{11}
	3rd	1.0×10^{12}
	4th	3.2×10^{12}
	5th	1.4×10^{13}
	6th	3.6×10^{13}
B	10th	2.5×10^{15}
	11th	4.0×10^{15}
	12th	5.5×10^{15}
	13th	7.0×10^{15}
	14th	7.8×10^{15}
C	3rd	6.2×10^{14}
	6th	2.8×10^{15}
	9th	6.4×10^{15}
	12th	1.4×10^{16}
D	1st	1.8×10^{14}
	2nd	5.3×10^{14}
	3rd	8.7×10^{14}
	4th	3.5×10^{15}
	5th	4.9×10^{15}

was set to raster in the area of 3 cm × 6 cm. The dose rate was about 1.5×10^{12} (ions/min · cm^2) for Ga^+ and 1.0×10^{13} (ions/min · cm^2) for He. The amount of dose given to each sample is listed in Table 7. Two Si(111) monochromator crystals were used to select 1.56 Å wavelength x-rays. A scintillation detector was used with a 2 mm × 2 mm slit, but no analyzer crystal was used. A five-circle diffractometer combined with a ultra high vacuum chamber equipped with a Ga^+ ion gun was utilized at the beam line. In high vacuum below 2×10^{-7} Torr of the base chamber pressure, the sample was irradiated with 25 keV Ga^+ or 3 keV He^+ ions. The samples were aligned with (202) and $(1\bar{1}1)$ peaks of Si substrate. To monitor the relaxation of the film due

to irradiation, index *h,k,L* scans and diagonal scan in *h,k* plane through (202) peak of the film were done after each dose.

It is useful to understand x-ray diffraction data more easily if we keep in mind that there are typically two contributions to diffraction intensity; a sharp and coherent peak and diffusely scattered broad peak. The main sharp peak comes from the long range ordering of the film coherent with the substrate. In contrast, the diffuse peak can have several sources: thermal vibration of atoms (phonons), short range ordering, strain fields near dislocation cores and point defects. Therefore, with more dose, we expect a decrease of the coherent peak and an increase of diffuse scattering with a possible peak shift. Since the only variable in our experiment is irradiation dose, it is safe to assume that any change in diffuse scattering results from a different distribution of either point defects or of strain field by dislocations and not from phonons.

6.1 Irradiation with 25 keV Ga^+ ions

In Fig. 31, the peak of SiGe film in sample A is shown to be aligned with that of its Si substrate, confirming pseudomorphic growth of the film. A RLM prior to the first dose shows typical broadening in perpendicular direction due to thickness effect and very narrow peak in in-plane direction. Therefore, it can be inferred from the RLM that the as-grown film is commensurate with a small amount of point defects and no dislocations within the limit of our experimental resolution. By point defects, we mean local defects with no significant relaxation involved around themselves. However, dislocations are referred to as sources of relaxation which allows relaxation through strain fields and could possibly cause a peak shift.

From Fig. 31, if we follow the trace of maximum intensity over contour lines we can get a line which connects the highest intensity points in the RLM. As shown in

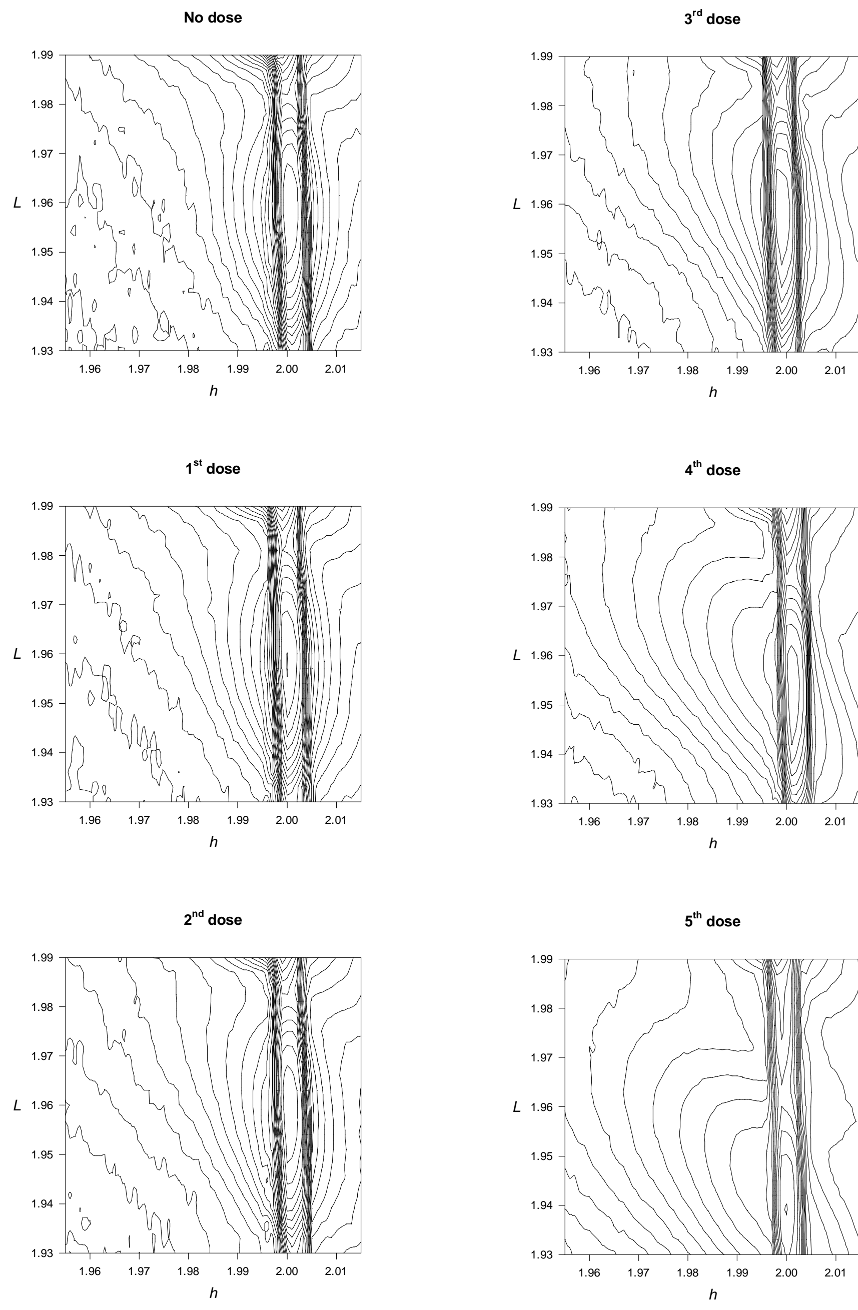

Figure 31: Mesh scans of a SiGe sample irradiated with 25 keV Ga^+ ions.

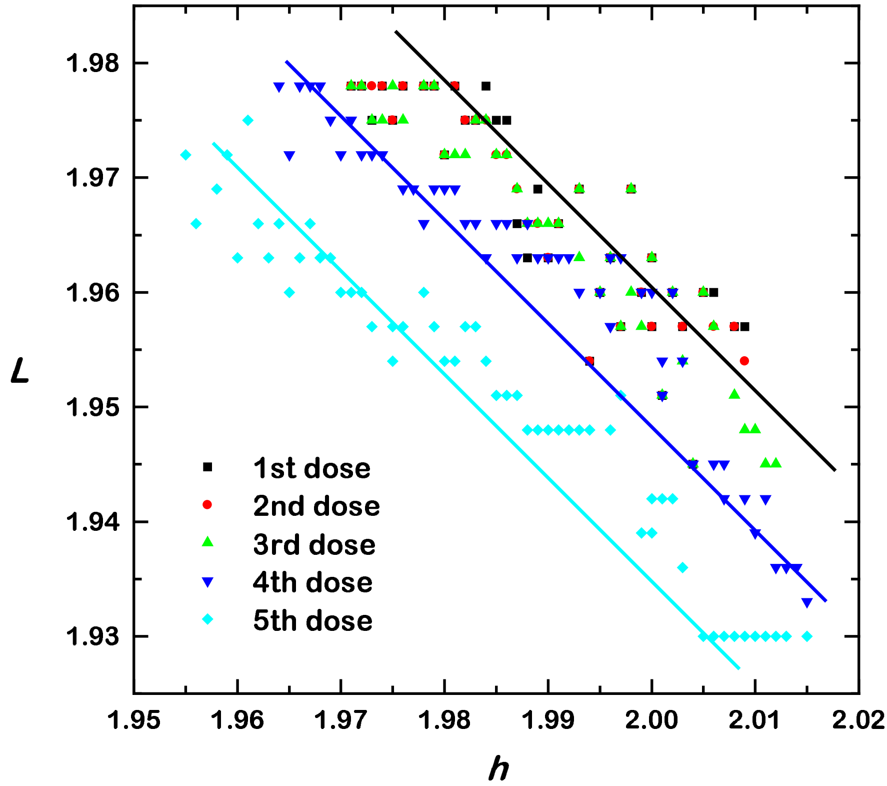

Figure 32: Lines of trace of the highest intensity in mesh scans.

Fig. 32, before dosing, the maximum intensity line has no slope. As we increase the dose, the line starts to incline. The inclination of the line connecting the highest intensity point is almost constant with increasing dose. If we connect the Bragg peak position of completely relaxed film and that of totally strained one, the inclination of that line agrees with those of the lines in Fig. 32. Therefore, it can be inferred from the figure that the film experiences typical lattice dilation in the surface normal direction.

In order to analyze the strain relaxation more rigorously, a data set of scans along

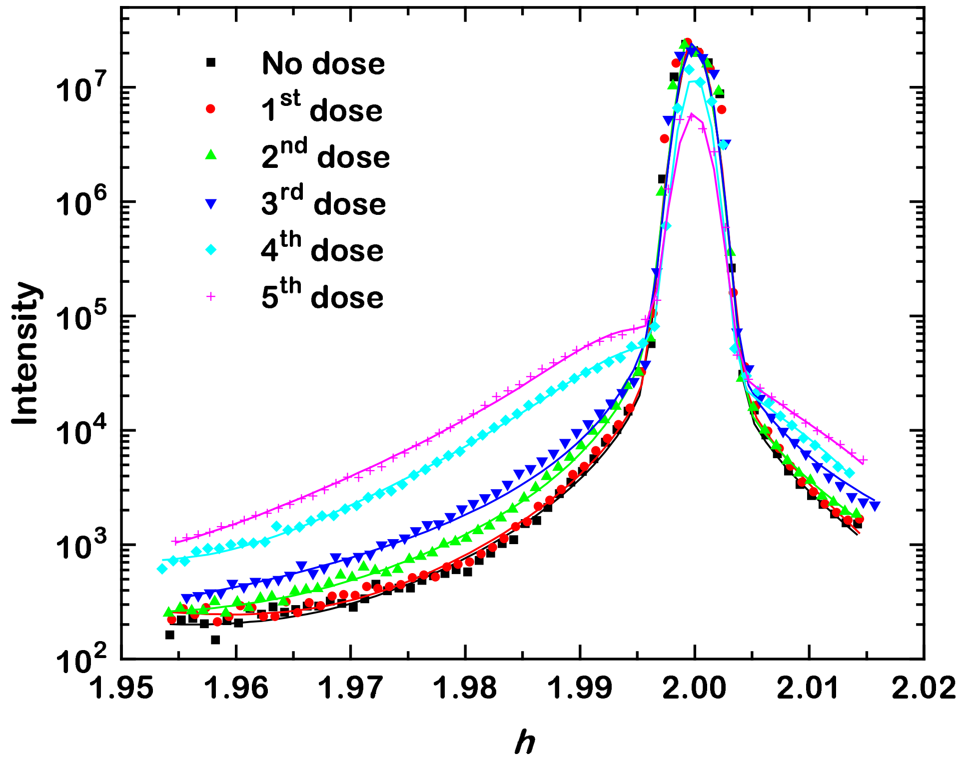

Figure 33: Index scans along h direction through (202).

the in-plane h direction was selected, which can be used to interpret strain relaxation along the in-plane direction. The index scan along the h direction prior to the first dosing, in Fig. 33, shows diffuse scattering, which has a $1/q^2$ dependence. This could be due to Huang diffuse scattering,[88, 89] but there is also a possibility that it is thermal diffuse scattering due to vibration of atoms. Symmetric diffuse scattering associated with the Si substrate is also seen in the upper region of the RLM.

With more dose, an asymmetric diffuse peak starts to appear and the (202) peak of SiGe in the RLM begins to move downward resulting from typical dilation effect

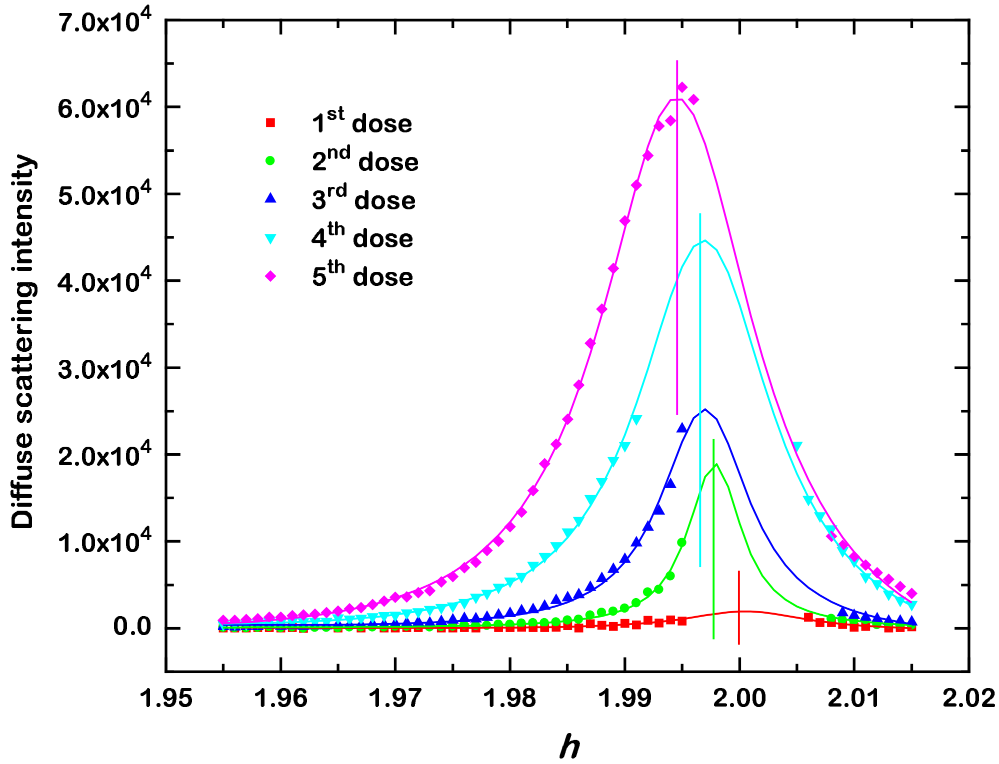

Figure 34: Diffuse scattering component of irradiated sample.

caused by point defects such as interstitials. In Fig. 33, h scans through (202) SiGe peak are shown with different amounts of irradiation. The appearance and shift of the broad, diffuse peak with increased dose of Ga^+ ions are more clearly seen. As a result of irradiation, the peak intensity of coherent SiGe diffraction decreased and the intensity of diffuse scattering increased. For clearer comparison, the diffuse scattering data are shown after subtraction of the scan from the unirradiated sample in Fig. 34. The fits are Lorentzians, which show the peak shift, broadening and increased intensity of the diffuse component. Note that the data near the coherent

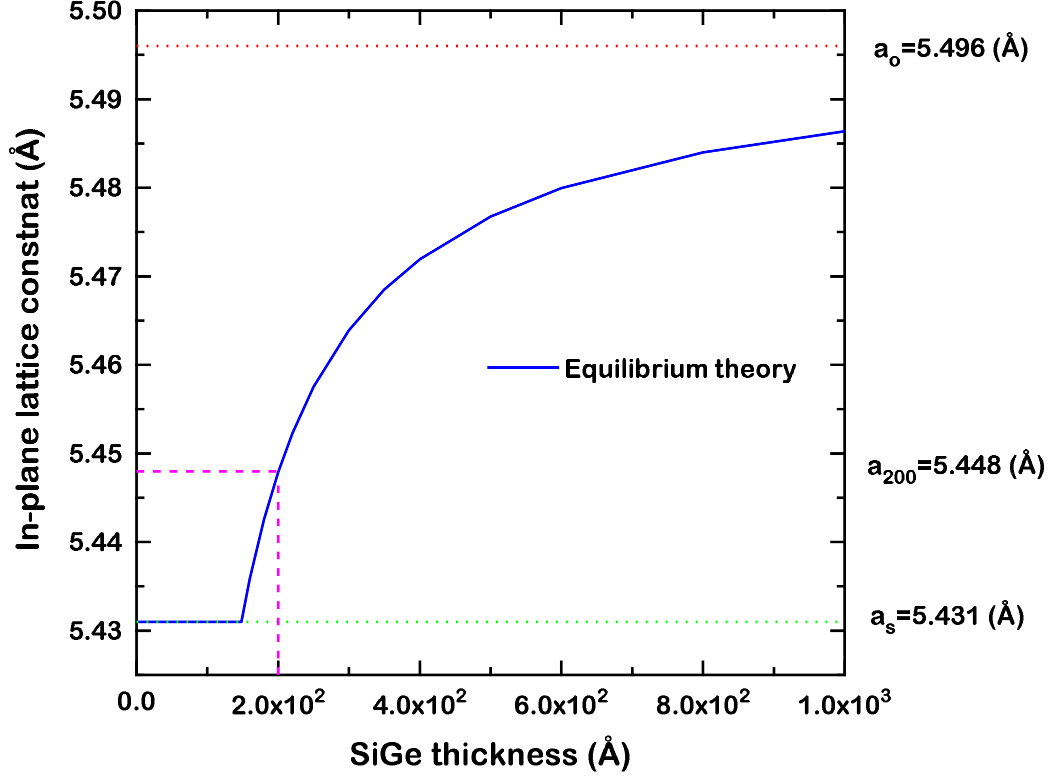

Figure 35: In-plane lattice constant of $Si_{0.7}Ge_{0.3}$ film as a function of thickness predicted by equilibrium theory.

peak have been omitted for consideration of diffuse scattering only. At higher doses, the diffuse scattering component does not follow $1/q^2$ dependence.

From these observations, the following statements can be made. The increased diffuse scattering can be attributed to a certain type of strain relaxation mechanism. In other words, irradiation introduces defects such as either pointlike vacancies or dislocations which result in a relaxation strain around them. In Fig. 35, it is shown that the in-plane lattice constant of $Si_{0.7}Ge_{0.3}$ as a function of thickness calculated by equilibrium theory using Eq. (19). $a_\circ$=5.496, a_s=5.431, and h_c=148 were used,

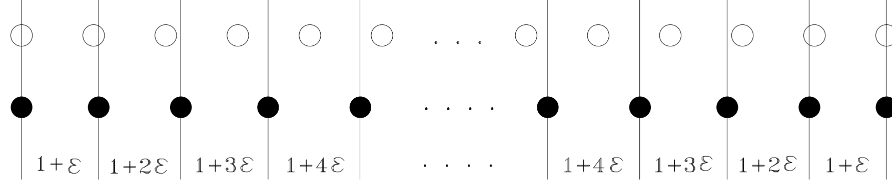

Figure 36: A 1-dimensional model of strain relaxation. Hollow circles represent original unrelaxed lattice points and solid ones are for relaxed lattice points.

where h_c was obtained by Eq. (29). As shown in Fig. 35, 200 Å of $Si_{0.7}Ge_{0.3}$ is in a metastable regime and the in-plane lattice constant for the thickness predicted by equilibrium theory is 5.448 Å. Therefore, in the reciprocal lattice unit of bulk Si, the peak position of this film in energy minimum state would be 1.994 (RLU). This agrees with the value we obtained as a diffuse peak position just before the film completely amorphized. Therefore, the film relaxed upon irradiation up to the point to which equilibrium theory predicts the film would do. To investigate the nature of relaxation mechanism, we tried a 1-dimensional model to simulate the situation.

In our model, we consider 2500 atoms situated at lattice points placed uniformly with unit separation in a 1-dimensional lattice. Then, one atom is taken out and neighboring atoms are allowed to relax toward the vacant site with the nearby spacings more stretched out, which is shown in Fig. 36. This model is physically more likely than uniformly relaxed lattice. In this relaxed cluster, N_r+1 lattice points are involved, two of which at the both ends are fixed. The relaxation displacement, ε,

was chosen to be dependent on N_r so that

$$\begin{aligned} \mathrm{N_r} + 1 &= \sum_{\mathrm{j=1}}^{(\mathrm{N_r}+1)/2} (1 + j\varepsilon) + \sum_{\mathrm{j=1}}^{(\mathrm{N_r}-1)/2} (1 + j\varepsilon) \\ &= N_r + \varepsilon \frac{(N_r+1)^2}{4} \end{aligned} \tag{41}$$

and $\varepsilon = 4/(N_r+1)^2$. Note that since one lattice point was taken out, only N_r atoms are available to fill out N_r+1 lattice units. In the following, we will refer to these displaced points as a relaxed cluster.

In the same way, in each calculation total N_d lattice points are taken out resulting in N_d relaxed clusters. The positions of the vacancy were randomly chosen and diffraction intensities from each configuration were averaged. The diffraction pattern of this arrangement of atoms is obtained by a Fourier transform. The instrumental resolution function was taken into account by averaging diffraction intensities within a Δq=0.003 Å^{-1} window. In Fig. 37, the results are shown with a different number of relaxed clusters. Qualitatively this model explains our data very well. Note that the range of relaxation is very large in this model. According to our model, the position of the diffuse peak is determined by the amount of relaxation completed and the width depends on N_r, which is the range of relaxation. The height of the diffuse peak is dependent upon N_d, the number of vacancy sites. It is straightforward to interpret the results of our model calculation. Since those relaxed lattice points contribute to the diffuse component, the peak shift is related with how much those atoms are displaced in average from the original lattice points. In the same reason, the peak width is determined by the size of a relaxed cluster.

As we see in Fig. 38, the more a film is irradiated, the wider the diffuse peak becomes and the larger the peak intensity is. So, within the framework of our model, the effect of irradiation can be explained as follows. Defects such as point-like or dislocations are introduced by irradiation which allows neighboring atoms to relax in

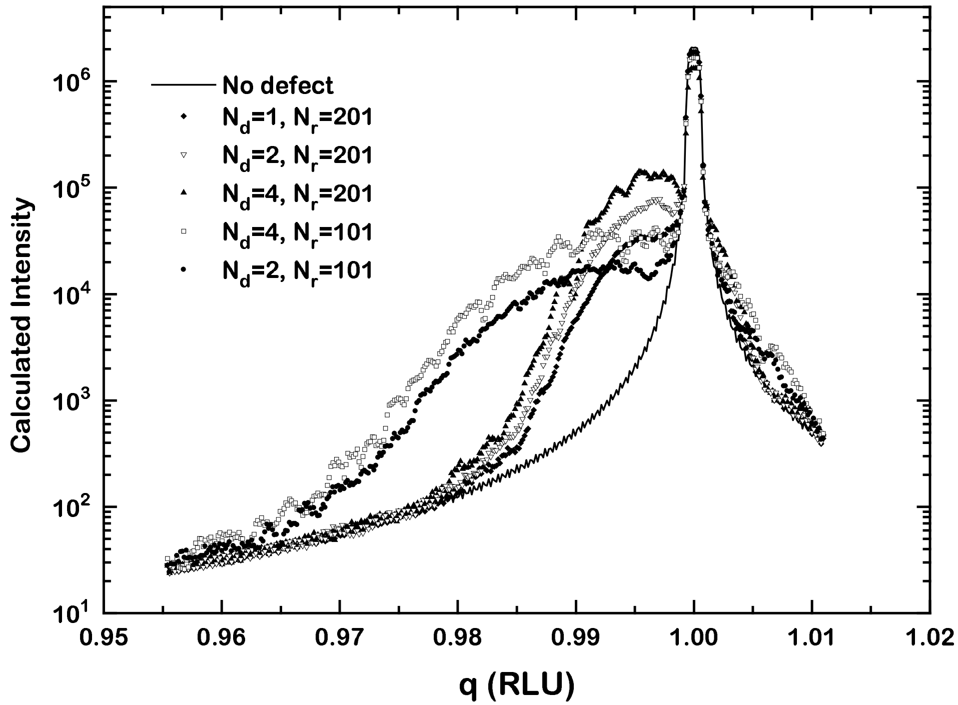

Figure 37: Diffraction intensity calculation using a 1-dimensional model of strain relaxation, described in the text.

a very long range. As a film becomes more irradiated, the number of defects increases and the range of relaxation decreases because the average distance between defects becomes smaller in a film that is heavily irradiated. However, the average amount of relaxation induced by defects increases as we increase dose. As far as the identity of defects is concerned, it is not clear whether they are point-like or line defects such as dislocations. One way to find whether diffuse component comes from either point-like defects or dislocations is as follows. Suppose we do mesh scan on *h,k* plane in the reciprocal space. If it were due to point-like defects, the broadening of the diffuse peak

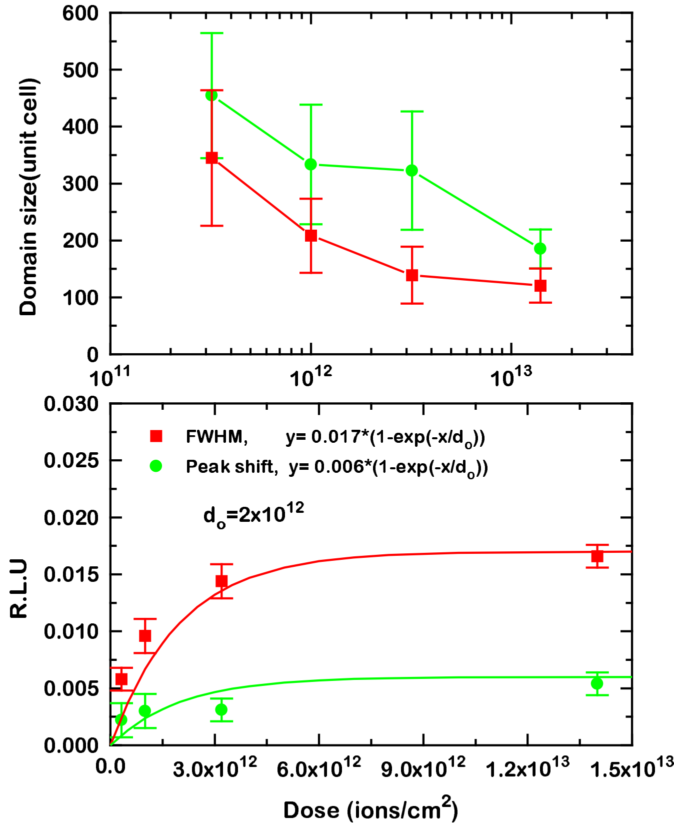

Figure 38: A plot of peak width and shift as a function of dose. Domain size calculated from peak width and shift is also shown in the upper panel.

would be isotropic because the relaxation is isotropic around such-defects. However, if it is from misfit dislocations, the broadening will look like a 'cross' due to high directionality of dislocations.

This interpretation is consistent with Kaganer *et al*'s work[90]. They calculated diffraction intensity from a thin film containing randomly distributed misfit dislocation networks and showed that the result was consistent with measurements. One of their conclusion was that at a low dislocation density coherent diffracted and diffuse

peaks would be separated. This kind of separation is only observable in a certain range of dislocation densities because the maxima of a coherent peak decreases exponentially.

Compared with our model to explain the strain relaxation due to irradiation, it is worth mentioning similar phenomena observed in other systems. For example, in noble metals there have been a lot of works regarding surface reconstruction and phase transition of Au(110) and Pt(110) surfaces[91, 92, 93]. In Au(110) surface, Robinson *et al.*[94] found that (3/2,0,0) peak from (2×1) reconstruction was displaced from an expected position and no higher order multiples of the primary reflection at (1/2-δ,0,0) were seen; instead reconstruction peaks were seen at positions displaced by bulk reciprocal lattice vectors from this primary location. This was explained by a model which is a locally (2×1) reconstruction of the bulk, interrupted by domain walls at regular intervals along [100]. In Au(110), a monatomic step[(111) facet] served as a domain wall and the experimental results were successfully understood with this model[94]. Similarly, Pt(110) surface also has a (2×1) surface reconstruction and displaced half order peaks, width and shift of which depend on temperature[95]. In Pt(110) case, the dependence of peak width and shift on temperature was explained by randomly distributed steps and anti-phase boundaries. From the point view of diffraction pattern, the trend of peak shift and broadening is similar in both noble metals and Si. However, phenomenologically speaking, there is a big difference in their structure to produce this type of diffraction pattern; in noble metals a local structure is maintained with monatomic steps modulated, but in Si an actual local spacing between atoms have changed without retaining its original value. For irradiated Si films, locally relaxed model is physically more probable.

Another example of peak shift and broadening is Si(113) surface. Si(113) takes (3×1) reconstruction and at 950 $\pm$ 40 K a (3×1) commensurate structure transforms

to an incommensurate disordered state[96, 97, 98, 99]. Transformation of structure in this example is involved in a change of local structure like in our case. However, it is different from our case in a sense the transformation of structure occurs all over the surface instead of a structural change of clustered-defects. So, in our case we were still able to observe the coherent peak due to a part of SiGe film which were not affected by irradiation.

If we assume that the defects are dislocations, we can obtain another interesting quantity from our data. With increasing dose of irradiation, the dislocations would introduce lattice mismatch and position of the diffuse scattering would move. As shown in Fig. 38, the width of diffuse peak in our experiment does increase and the position of peak shifts to lower h value, which means the in-plane lattice constant increases. The increase of in-plane lattice constant means that the elastic strain of the film decreases. Therefore, an average distance between dislocations becomes smaller. If we assume that the average size of small domain in the film would be proportional to the average distance between dislocations, the domain size can be calculated using Eq.(20). In the meanwhile, from the relationship, *Coherence Length* $\approx 2\pi/\Delta q$(FWHM), the domain size can be also derived. So, from these data the average size of domain was obtained and plotted in Fig. 38. The results from two different methods agree.

6.2 Irradiation with 3 keV He^+ ions

In Figs. 39 through 42, there are five or four scans are plotted for each sample. Three of them are index scans along reciprocal lattice axes, i.e., a radial scan is along the h direction, transverse along the k direction and an L scan. A diagonal scan is through a Bragg peak of a film along the direction in which a film is supposed to relax as we discussed above. A non-parallel scan is along the line between a totally relaxed

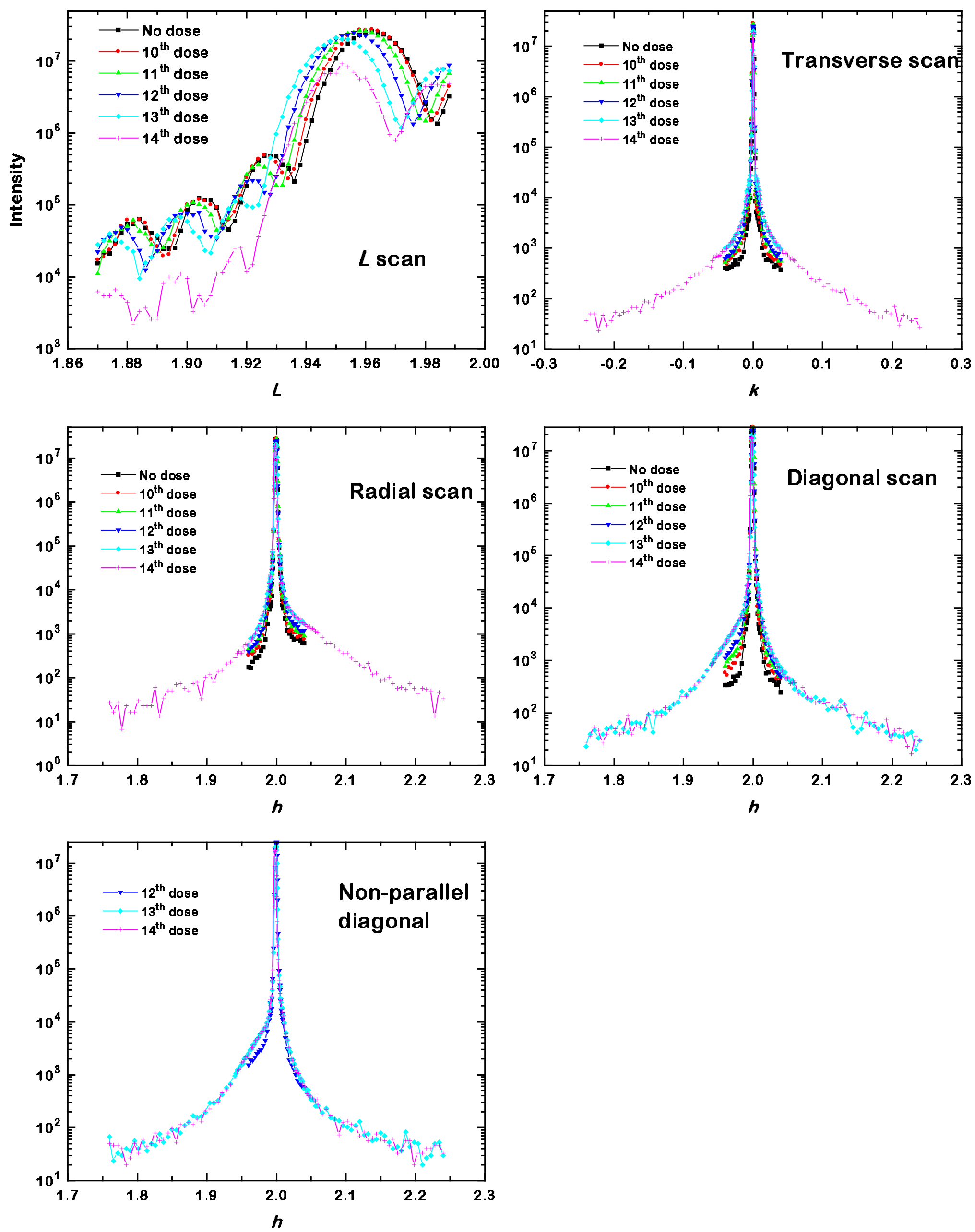

Figure 39: Scans of the sample B through (202) peak.

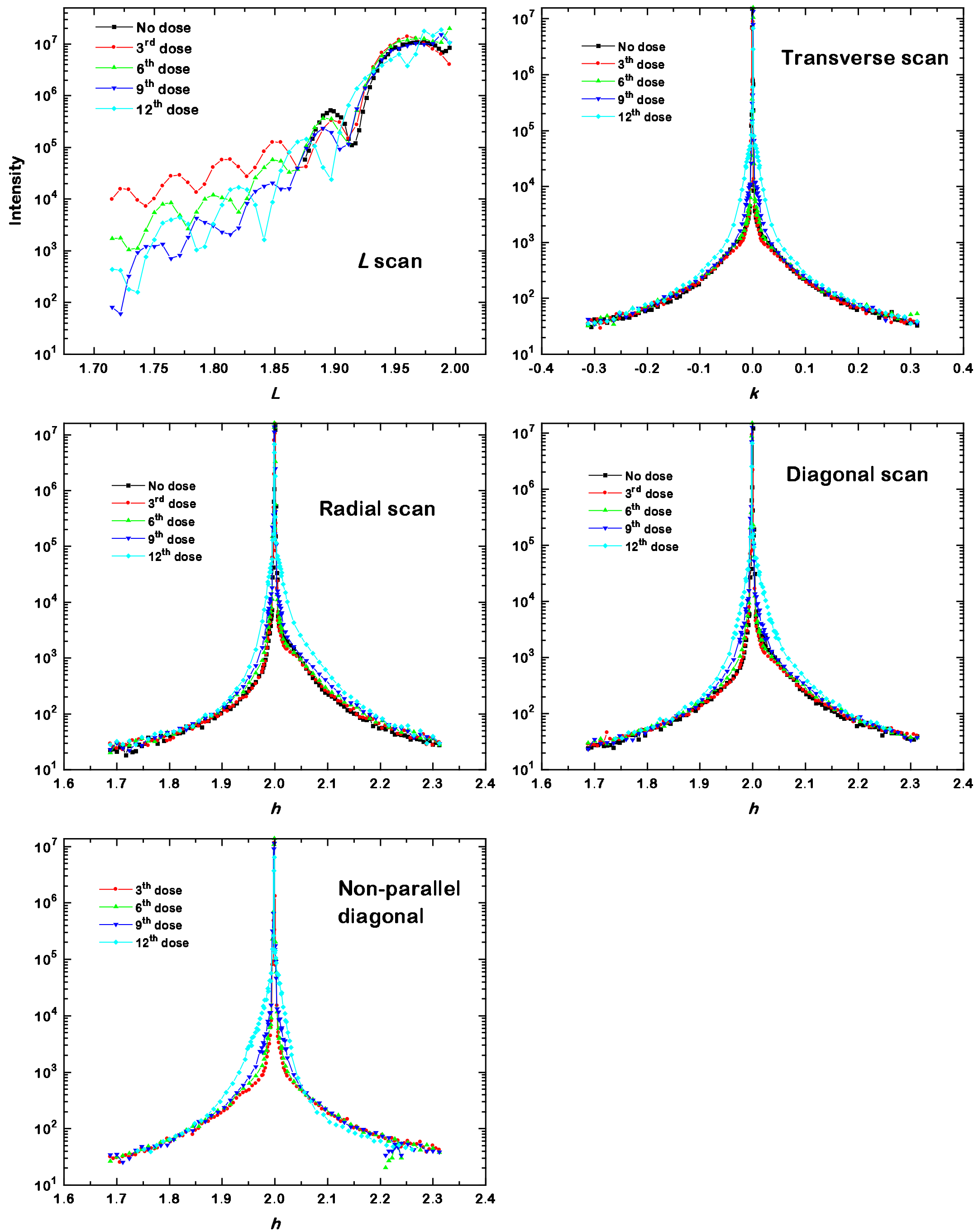

Figure 40: Scans of the sample C through (202) peak.

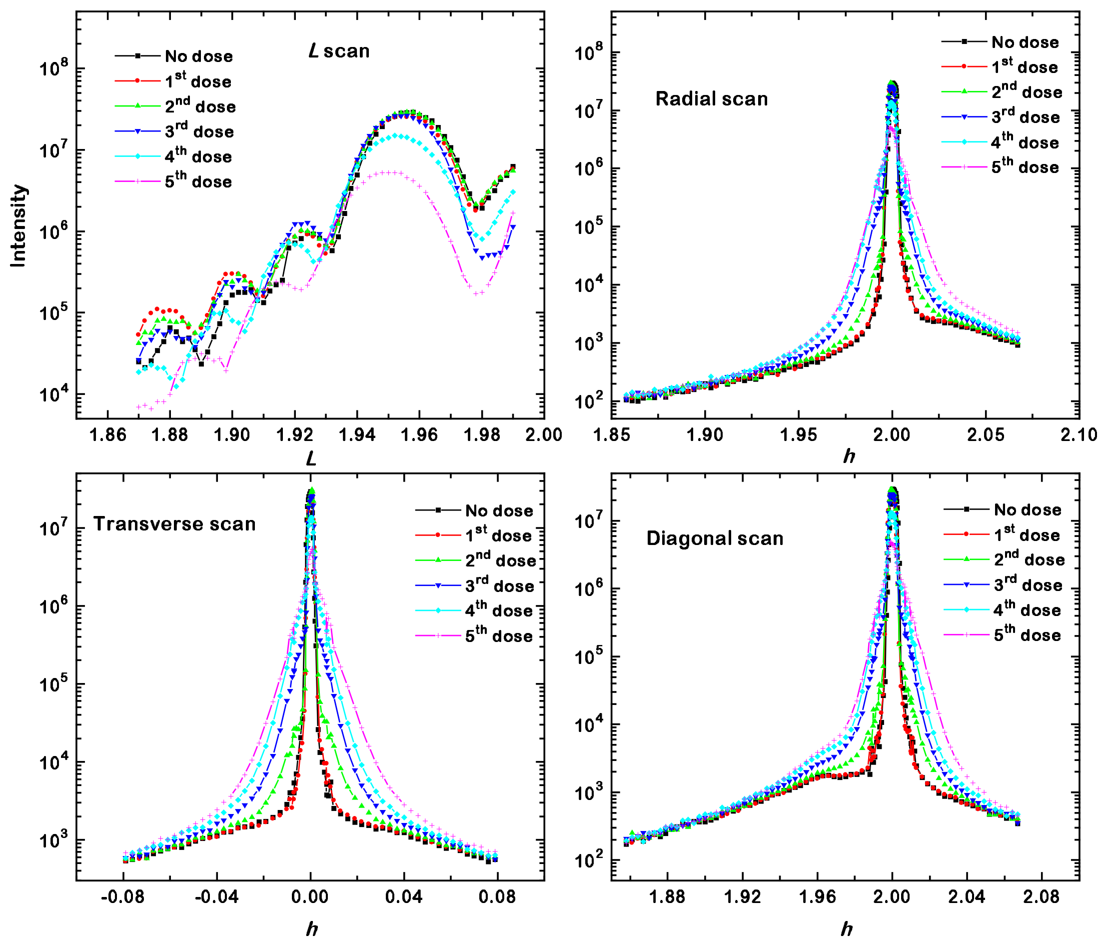

Figure 41: Scans of the sample D through (202) peak.

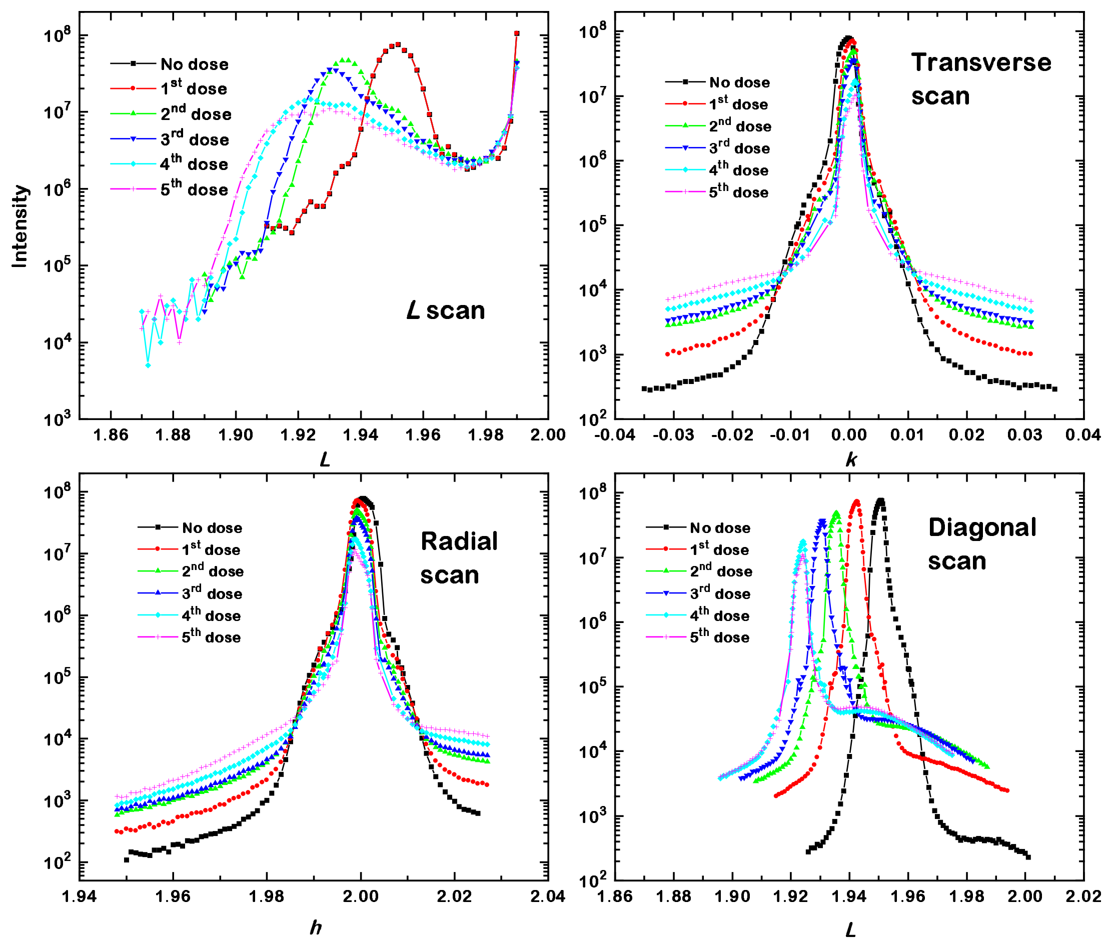

Figure 42: Scans of the sample E through (202) peak.

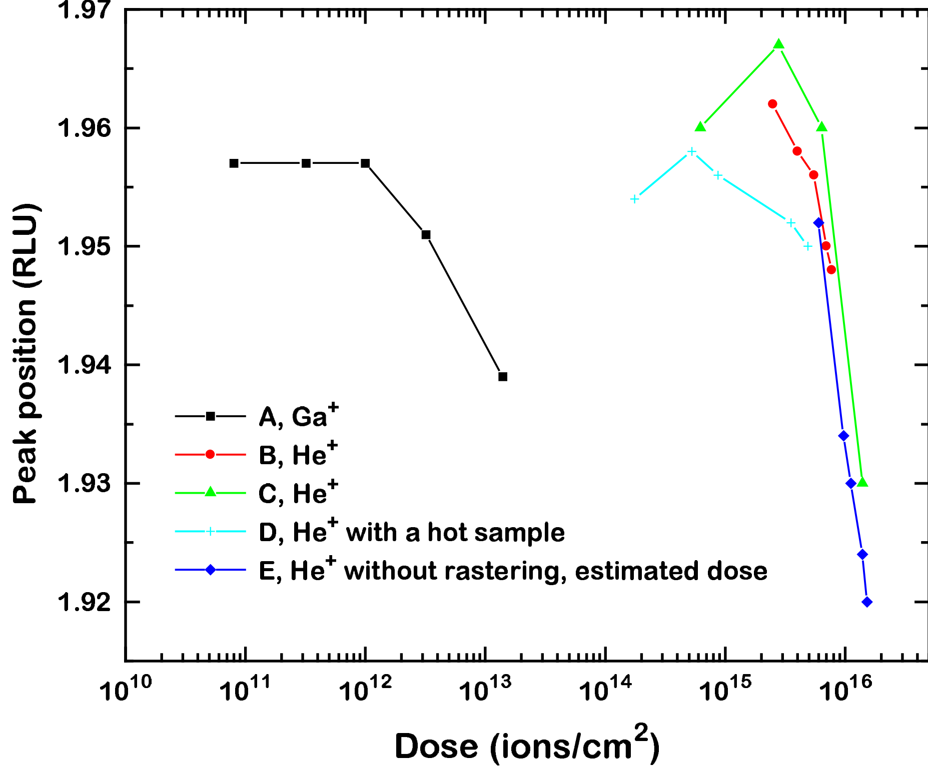

Figure 43: Dilation effect of out-of-plane lattice constant upon irradiation. Note that the sample D was irradiated with the sample hot and the sample E was irradiated without rastering. So, the dose was estimated from the amount of dilation.

peak position and a current Bragg peak position. In other words, a diagonal scan is parallel with the lines shown in Fig. 32, but passes through an actual Bragg peak of the film. However, a non-parallel scan always goes through the Bragg peak of a completely relaxed film and the actual Bragg peak of the film. Consistently through the samples, the out-of-plane lattice constant dilates with increasing dose. In h scans, there seems no clear sign of asymmetric broadening of diffuse component. However, for some samples there exists a slight amount of increase in diffuse peak intensity at

the shoulder of lower part of h. From L scans of the samples, the amount of dilation due to irradiation for each sample is plotted in Fig. 43.

In summary, a series of metastable $Si_{0.7}Ge_{0.3}$ films were irradiated with 25 keV Ga^+ or 3 keV He^+ ions and using *in-situ* x-ray diffraction the strain relaxation was observed. As we predicted, in-plane relaxation was observed along with the typical dilation effect in perpendicular direction. Before irradiation, the diffuse scattering was probably due to point defects or thermal vibration. With more dose, it was clearly observed that the film in sample A started to relax by introducing defects that allowed long range relaxation of neighboring atoms. The argument was supported by the shift and broadening of the diffuse scattering due to strain relaxation near defects induced by irradiation.

Chapter VII. Strain relaxation induced by irradiation; evidence of equilibrium theory for GaN

In Ch. IV, we showed evidence that epitaxial GaN films are not metastable by explaining strain relaxation as a function of thickness with an equilibrium theory[62]. In comparison, the growth of $Si_{1-x}Ge_x$ has been known to be influenced by kinetic effect so that the measured critical thicknesses are larger than those predicted by equilibrium theory. Since $Si_{1-x}Ge_x$ film is not grown under a complete equilibrium condition and in a metastable state, strain relaxation of in-plane lattice constant was expected when an external relaxation source such as energetic ion bombardment was provided. And in Ch. VI, we showed that a metastable SiGe film relaxed in response to irradiation. However, since GaN is assumed to be under equilibrium we don't expect any deviation of pseudomorphic status with further irradiation.

A series of GaN films on AlN buffer layer in different thickness combinations were grown using MBE. X-ray measurements were done at the beamline X16A of National Synchrotron Light Source at Brookhaven National Laboratory. Two Si(111) monochromator crystals were used to select 1.56 Å wavelength x rays. A scintillation detector was used with a 2 mm $\times$ 2 mm slit, but no analyzer crystal was used. A five-circle diffractometer combined with a ultra high vacuum chamber equipped with a He^+ ion gun was utilized at the beam line. In high vacuum below 2×10^{-7} Torr of the base chamber pressure, the sample was irradiated with 3 keV of He^+ ions.

The sample was aligned with (113) and ($\bar{1}23$) peaks of sapphire substrate. To monitor possible relaxation of GaN film due to ion bombardment, three index scans through (101) GaN peak were made for each dose. Since we used the sapphire substrate for indexing, the GaN (101) peak appears near (0.86, 0.86, 2.5) in sapphire units. In Fig. 44, *h, k, l* directional scans are shown for the sample with 25 Å of

GaN on it. In the h scan, there is no sign of peak shift with increasing dose. This result confirms expectation that no relaxation would take place. In addition to the absence of peak shift, little diffuse scattering due to irradiation was seen either. The full width at half maximum is almost constant during the whole period of dosing and only peak intensity goes down, again different from what we observed in SiGe films in the previous chapter. The small peaks near GaN (101) peak is due to $(11l)$ crystal truncation rod of sapphire substrate. The k scan shows that the alignment is maintained in a good condition during irradiation and the trend of a full width at half maximum and peak height is about the same as for the h scan. In Fig. 45, scans through (102) peaks of both AlN and GaN are shown. The decrease of peak intensity is more dramatic than (101) scans and the peak almost disappears after the 6th dose. In contrast to SiGe films, we conclude that what was happening to GaN film is that it was being destroyed by irradiation with little or no relaxation at all. For the sample with 50 Å of GaN on it, the same trend is observed.

One big difference between GaN and SiGe is that the dilation effect is not observed for GaN. In our measurements, the out of plane lattice constant increased up to a certain point of dosing, then it contracted with more dose. This is clearly seen in diagonal scan in Fig. 45. A possible explanation for the contraction of lattice constant was that He^+ ions knocked out the constituent atoms of the film and produce some amount of vacancy which makes the size of unit cell decrease. Atomic clustering would tend to form where there is a high concentration of atomic vacancies. One way to check this hypothesis is x-ray photoelectron spectroscopy (XPS). Since our sample is thin enough for photoelectrons to travel through it. XPS measures the binding energy of electrons and is sensitive to the structural environment of the emitting atom. We made XPS measurements with the sample C to see if there is any compositional difference before and after irradiation. XPS measurements were done

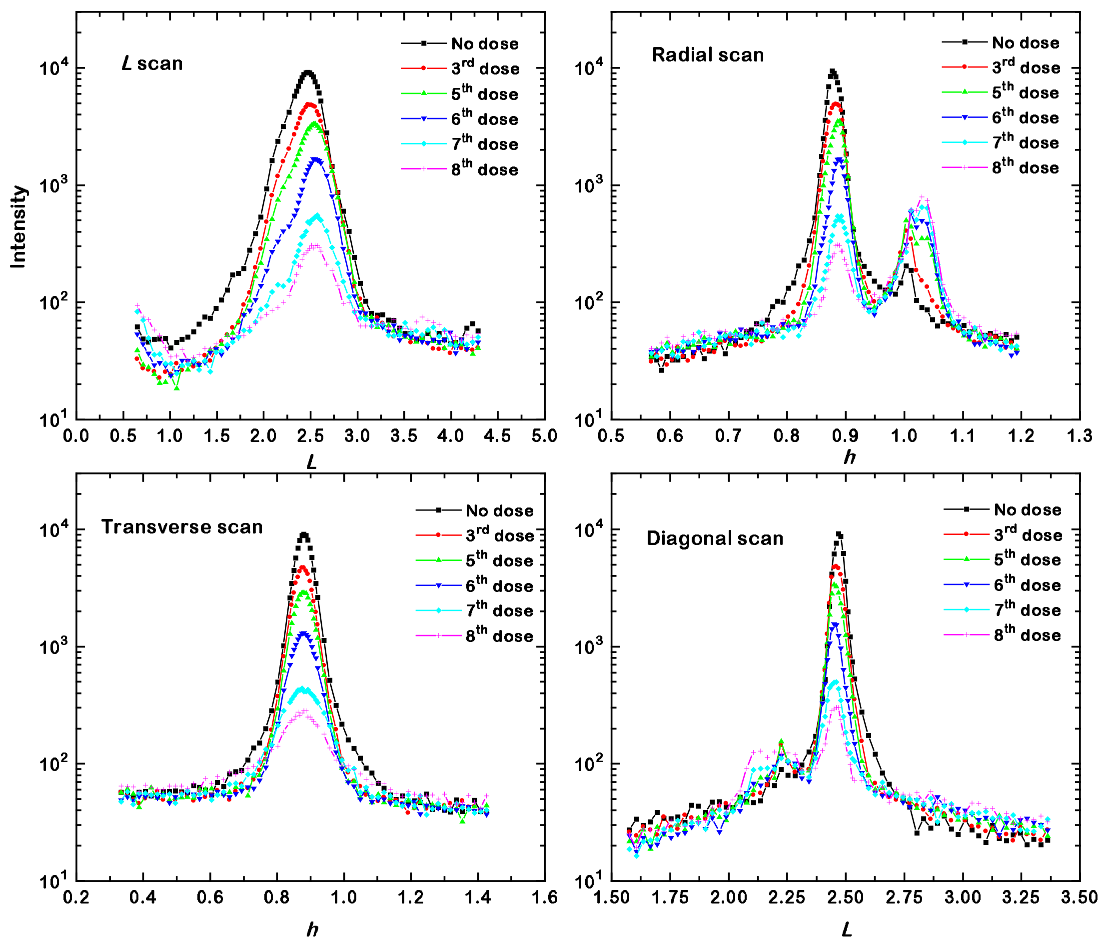

Figure 44: Scans of the sample B through (101) peak.

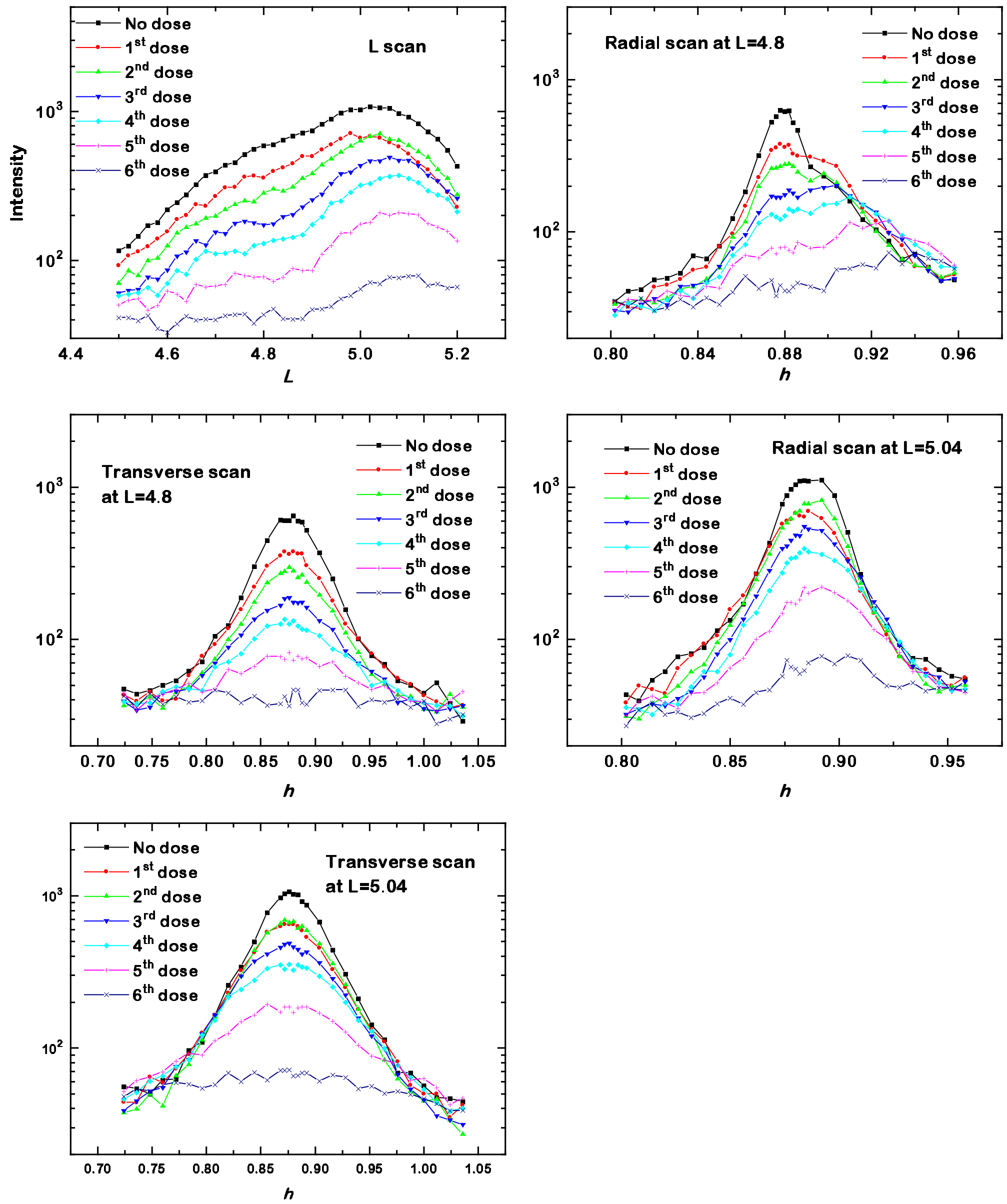

Figure 45: Scans of the sample B through (102) peak.

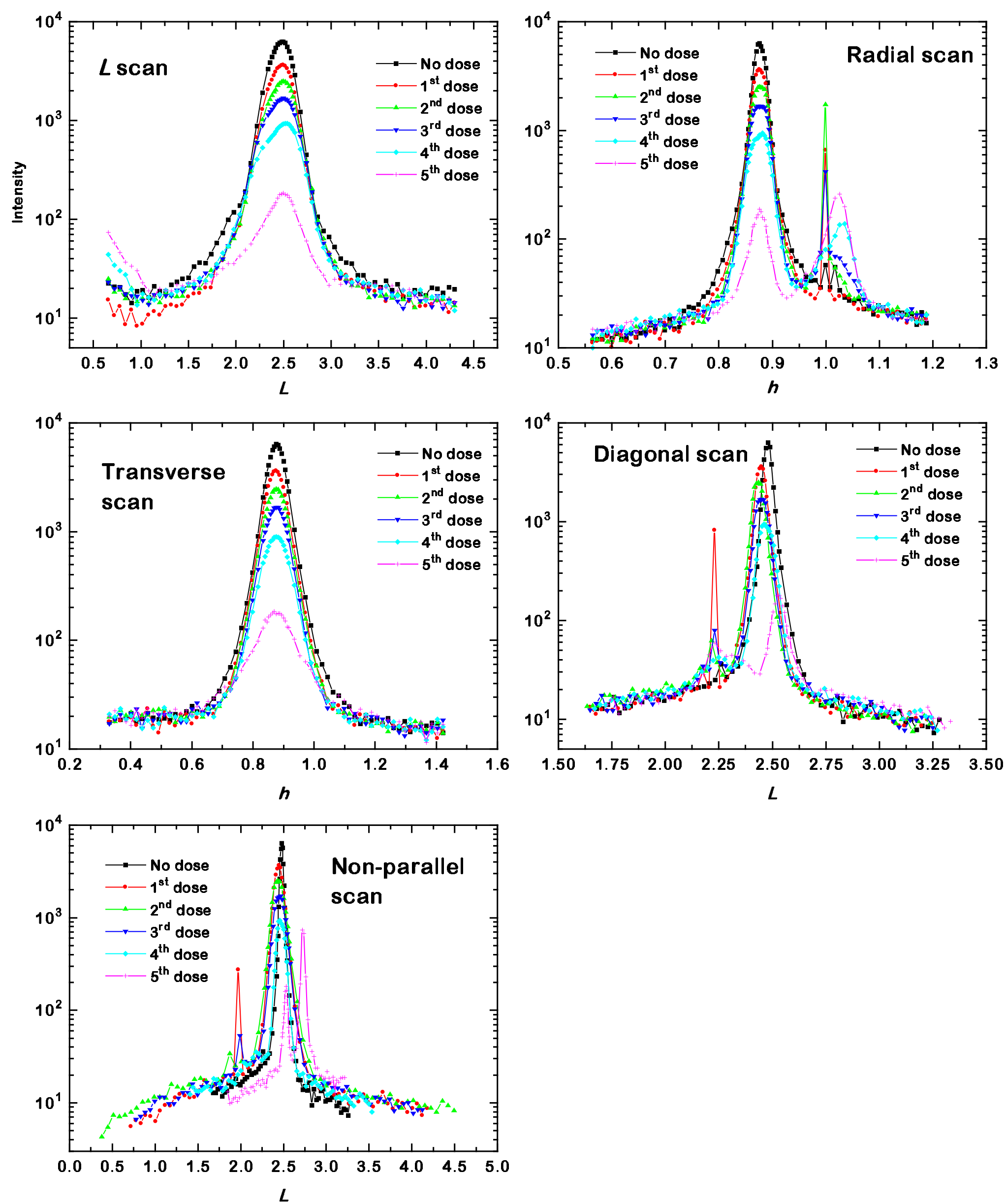

Figure 46: Scans of the sample C through (101) peak.

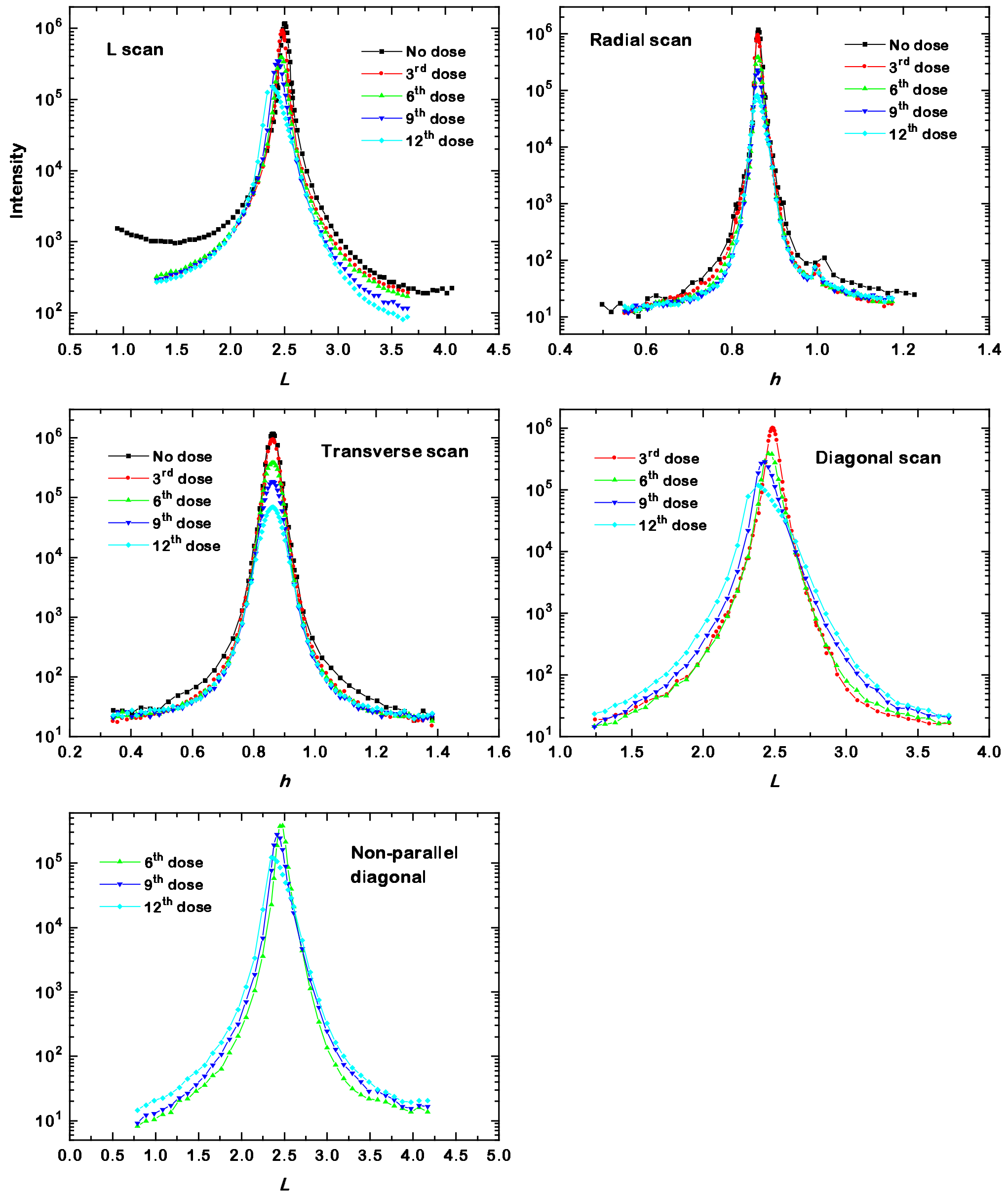

Figure 47: Scans of the sample G through (101) peak.

at the center of microanalysis at the University of Illinois with Perkin-Elmer PHI Model 5600 MultiTechnique system with a Mg Kα source. Ga 3d and 2p electrons were chosen to identify Ga bonding. A binding energy correction for sample charging was made.

The measured binding energy for Ga 3d electron before irradiation was 19.63 eV, which is consistent with the previous measurements from other authors[100]. Since the sensitivity of photoelectrons depend on the matrix of the compound which is being measured, the assumption that the sensitivity factor has not changed a lot before and after irradiation is not absolutely accurate. However, the measurement showed that the relative composition of Ga to N is almost 2.5 times after irradiation, the total dose of which was 1.2 $\times 10^{17}$ (ions/cm^2).

One possibility is that He^+ ions favorably collide with nitrogen atoms and induce partial Ga clustering which would result in contraction of out of plane lattice constant. Alternatively, He^+ hits Ga and N with the same probability, but with different knock-out probability. Change of color after irradiation may indicate Ga clustering, too. It is noteworthy that N-clusters might not survive because N_2 gas can escape. In Fig. 47, the same type of scans are shown for the sample G. Unlike the first two samples, it shows lattice dilation along the surface normal direction in the L scan. However, the decrease of peak intensity and absence of broadening are the same as before. The only difference between these samples was that the first two are below a critical thickness and G is above a critical thickness. The different behaviors in response to irradiation among GaN films are not clearly understood.

In summary, the effect of He^+ ion irradiation on GaN thin films was studied using *in-situ* x-ray diffraction. No relaxation of strain in in-plane lattice constant was observed which is one evidence of stable GaN under equilibrium state. A small contraction of out-of-plane lattice constant was measured and was attributed to nitrogen

Table 8: Irradiation dose for each GaN samples. All these samples were irradiated with 3 keV He^+ ions. The samples B and C are the same as in Ch. IV.

Sample	AlN (Å)	GaN (Å)		Total dose (ions/cm^2)
B	32	25	1st	2.9×10^{15}
			2nd	2.3×10^{16}
			3rd	2.9×10^{16}
			4th	3.6×10^{16}
			5th	4.7×10^{16}
			6th	7.0×10^{16}
			7th	9.0×10^{16}
			8th	1.1×10^{17}
C	32	50	1st	1.0×10^{16}
			2nd	2.7×10^{16}
			3rd	4.5×10^{16}
			4th	6.5×10^{16}
			5th	1.2×10^{17}
G	64	500	3rd	7.0×10^{15}
			6th	2.5×10^{16}
			9th	3.9×10^{16}
			12th	5.5×10^{16}

vacancy induced by irradiation. *Ex-situ* XPS measurements supported the argument of nitrogen vacancy by showing that the relative composition of Ga increased 2.5 times more than before irradiation. In the sample G, a lattice dilation effect was observed and the different behaviors among GaN films are not clear.

Chapter VIII. Summary and conclusion

Using x-ray diffraction we studied strain relaxation of physical systems in two different regimes; microscopically and macroscopically. For microscopic strain analysis, Sb/Si(111) was studied and it was observed that surface layers of Si with Sb adsorption rearranged themselves to maintain energy minimum configuration so that adsorbate-induced strain propagated several layers inside Si.

For the case of macroscopic strain relaxation analysis, GaN thin films grown on sapphire (0001) with AlN buffer layer were investigated. Equilibrium theory was successfully applied to explain their strain relaxation as a function of thickness. However, it was not clear that AlN films grown on sapphire (0001) also followed the same theoretical prediction. In contrast with GaN, for SiGe films, a kinetic effect needs to be included to explain a larger experimentally determined critical thickness than theoretically predicted. In this sense, GaN behaves in a fundamentally different way from SiGe. To investigate thoroughly this difference, we irradiated GaN and SiGe samples below critical thickness with high energetic ions in order to activate defects which allowed neighboring atoms to relax. Since SiGe was in a metastable state, but not GaN, we found that only SiGe relaxed upon introducing defects induced by irradiation. Our prediction was confirmed by observing a peak shift in irradiated SiGe samples. No shift but only intensity decrease was observed for GaN.

References

[1] I. K. Robinson and D. J. Tweet, Rep. Prog. Phys. **55,** 559 (1992).

[2] J. D. Jackson, Classical Electrodynamics (1975).

[3] B. E. Warren, X-ray Diffraction (1969).

[4] I. K. Robinson, Phys. Rev. B. **33,** 3830 (1986).

[5] Donald A. Walko, unpublished.

[6] W. R. Busing, and H. A. Levy, Acta. Cryst. **22,** 457 (1967).

[7] F. R. N. Nabarro, Theory of crystal dislocations, *Oxford Univ. Press* (1967).

[8] J. P. Hirth and J. Lothe, Theory of dislocations, 2nd Ed. *John Wiley* & *Sons,* (1982).

[9] E. Kasper and H. -J. Herzog, Thin Solid Films **44,** 357 (1977); E. Kasper, Surf. Sci. **174,** 630 (1986).

[10] S. C. Jain, J. R. Willis, and R. Bullough, Adv. in Physics **39,** 127 (1990).

[11] L. J. Brillson, Surf. Sci. Rep. **2,** 123 (1982).

[12] M. Tabe and K. Kajiyama, Jpn. J. Appl. Phys. **22,** 423 (1983).

[13] R. A. Metzger and F. G. Allen, Surf. Sci. **137,** 397 (1984).

[14] S. A. Barnett, H. F. Winters and J. E. Greene, Surf. Sci. **165,** 303 (1986).

[15] J. M. Nicholls, B. Reihl, and J. E. Northrup, Phys. Rev. B **35,** 4137 (1987).

[16] J. Nogami, S. Park, and C. F. Quate, Phys. Rev. B **36,** 6221 (1987).

[17] R. J. Hamers and J. E. Demuth, Phys. Rev. Lett. **60,** 2527 (1988).

[18] R. I. G. Uhrberg, R. D. Bringans, M. A. Olmstead, R. Z. Bachrach, and J. E. Northrup, Phys. Rev. B **35,** 3945 (1987).

[19] C.-Y. Park, T. Abukawa, T. Kinoshita, Y. Enta and S. Kono Jpn. J. Appl. Phys. **27,** 147 (1988).

[20] T. Abukawa, C.-Y. Park and S. Kono, Surf. Sci. **201**, L513 (1988).

[21] P. Mårtensson, G. Meyer, N. M. Amer, E. Kaxiras and K. C. Pandey, Phys. Rev. B **42,** 7230 (1990).

[22] J. C. Woicik, T. Kendelewicz, K. E. Miyano, P. L. Cowan, C. E. Bouldin, B. A. Karlin, P. Pianetta and W. E. Spicer, Phys. Rev. B **44,** 3475 (1991).

[23] S. Nakatani, A. Saito, Y. Kuwahara, T. Takahashi, M. Aono and S. Kikuta, Jpn. J. Appl. Phys. **31,** L426 (1992).

[24] S. Nakatani, Y. Kuwahara, T. Takahashi and M. Aono, Surf. Sci., **357-358,** 65 (1996).

[25] P. H. Fuoss, I. K. Robinson, Nucl. Inst. and Meth. **222,** 171 (1984).

[26] I. K. Robinson, Handbook on Synchrotron Radiation, **3,** 221 (1991).

[27] A. L. Patterson, Phys. Rev. **46,** 372 (1934).

[28] I. K. Robinson, Rep. Prog. Phys. **55,** 599 (1992).

[29] O. L. Alerhand, J. D. Joannopoulos, and E. J. Mele, Phys. Rev. B, **39,** 12622 (1989).

[30] Y. Qian, P. F. Lyman, Tienlin Lee, and M. J. Bedzyk, Physica B, **221,** 430 (1996).

[31] P. F. Lyman, Y. Qian, and M. J. Bedzyk, Surf. Sci., **325,**, L385 (1995).

[32] M. Richter, J. C. Woick, J. Nogami, P. Pianetta, K. E. Miyano, A. A. Baski, T. Kendelewicz, C. E. Bouldin, W. E. Spicer, C. F. Quate, and I. Lindau, Phys. Rev. Lett., **65,** 3417 (1990).

[33] M. W. Grant, P. F. Lyman, J. H. Hoogenraad, and I. E. Seiberling, Surf. Sci., **279,** L180 (1992).

[34] R. Felici *et al.,* unpublished.

[35] S. Tang, and A. J. Greeman, Phys. Rev. B, **47,** 1460 (1993).

[36] B. D. Yu, and A. Oshiyama, Phys. Rev. B, **50,** 8942 (1994).

[37] A. F. Wells, Structural Inorganic Chemistry, New York: *Oxford Univ. Press,* 868 (1984).

[38] D. H. Rich, A. Samsavar, T. Miller, F. M. Leibsle, and T.-C. Chiang, Phys. Rev. B, **40,** 3469 (1989).

[39] M. Mizuta, S. Fujieda, Y. Matsumoto, and T. Kawamura, Jpn. J. Appl. phys. **25,** L945 (1986); S. Strite, D. Chandrasekhar, D. J. Smith, J. Sariel, H. Chen, N. Teraguchi, and H. Morkoç, J. Cryst. Growth **127,** 204 (1993).

[40] H. Morkoç, S. Strite, G. B. Gao, M. E. Lin, B. Sverdlov, and M. Burns, J. Appl. Phys. **76,** 1363 (1994).

[41] S. N. Mohammad, A. Salvador, and H. Morkoç, Proc. IEEE **83,** 1306 (1995); S. Strite and H. Morkoç, J. Vac. Sci. Technol. B **10,** 1237 (1992); S. Strite, M. E. Lin, and H. Morkoç, Thin Solid Films **231,** 197 (1993).

[42] S. Yoshida, S. Misawa, and S. Gonda, Appl. Phys. Lett. **42,** 427 (1983).

[43] H. Amano, N. Sawaki, I. Akasaki, and Y.Toyoda, Appl. Phys. Lett. **48,** 353 (1986).

[44] O. Lagerstedt and B. Monemar, Phys. Rev. B **19,** 3064 (1979).

[45] W. L. Bond, Acta Cryst. **13,** 814 (1960).

[46] T. Detchprohm, K. Hiramatsu, K. Itoh and I. Akasaki, Jpn. J. Appl. Phys. **31,** L1454 (1992); K. Hiramatsu, T. Detchprohm and I. Akasaki, Jpn. J. Appl. Phys. **32,** 1528 (1993); H. Amano, K. Hiramatsu and I. Akasaki, Jpn. J. Appl. Phys. **27,** L1384 (1988).

[47] I. K. Robinson, H. Graafsma, A. Kvick, and J. Linderholm, Rev. Sci. Instrum. **66,** 1765 (1995).

[48] G. C. Osbourn, IEEE J. Quantum Electron. QE-22, 1677 (1986).

[49] J. H. van der Merwe, Surf. Sci. **31,** 198 (1972).

[50] C. Kim, I. K. Robinson, J. Myoung, K. Shim, K. Kim, and M. Yoo, Mat. Res. Soc. Symp. Proc. **423,** 557 (1996).

[51] J. W. Matthews and A. E. Blakeslee, J. Cryst. Growth **27,** 118; **32,** 265 (1974).

[52] B. W. Dodson and J. Y. Tsao, Appl. Phys. Lett. **51,** 1325 (1987); **52,** 52 (1988).

[53] E. Kasper, in Physics and Applications of Quantum Wells and Superlattices, edited by E. E. Mendez and K. von Klitzing (Plenum Press, New York and London, 1987), p.101.

[54] R. People and J.C. Bean, Appl. Phys. Lett. **47,** 322 (1985).

[55] A. Fischer, H. Kuhne, and H. Richter, Phys. Rev. Lett. **73,** 2712 (1994).

[56] Lisa Sugiura, J. Appl. Phys. **81,** 1633 (1997).

[57] S. Nakamura, T. Mukai, and M. Senoh, Appl. Phys. Lett. **62,** 1786 (1994).

[58] S. Nakamura, T. Mukai, and M. Senoh, J. Appl. Phys. **76,** 8189 (1994).

[59] S. Nakamura, M. Senoh, N. Iwasa, S. Nagahama, T. Yamada, T. Matsushita, H. Kiyoku, and Y. Sugimoto, Jpn. J. Appl. Phys. 1 **35,** L74 (1996).

[60] O. Aktas, W. Zim, Z. Fan, F. Stengel, A. Botchkarev, A. Salvador, B. Sverdlov, S. N. Mohammad, and H. Morkoc, International Electronic Device Meeting 205 (1995).

[61] F. Y. Huang, and K. L. Wang, Phil. Magz. Lett., **72,** 231 (1995).

[62] C. Kim, I. K. Robinson, J. Myoung, K.-H. Shim, M.C. Yoo, and K. Kim, Appl. Phys. Lett. **69,** 2358 (1996).

[63] T. Azuhata, T. Sota, and K. Suzuki, J. Phys.: Condens. Matter **8,** 3111 (1996).

[64] J. P. Hirth, and J. Lothe, *Theory of dislocations*, 2nd Ed.,John Wiley & Sons, P.436 (1982).

[65] J. C. Bean, "Silicon-based semiconductor heterostructures" in "Silicon MBE" ed. E. Kasper and J. C. Bean (CRC press, Florida) **2,** Ch.11 (1988).

[66] S. S. Iyer, G. L. Patton, J. M. C. Stork, B. S. Meyerson, and D. L. Harame, IEEE Trans. Electron Dev. **36,** 2943 (1989).

[67] T. Manku and A. Nathan, J. Appl. Phys. **72,** 1205 (1993).

[68] T. Mishima, W. C. Fredriksz, G. F. A. van der Walle, D. J. Gravesteijn, R. A. van den Heuvel and A. A. van Gorkum, Appl. Phys. Lett. **57,** 2567 (1990).

[69] F. Schäffler and H. J. Jorke, Appl. Phys. Lett. **58,** 397 (1991).

[70] R. A. Kubiak, E. Basaran, D. W. Smith, A. D. Plews, J. Brighten, S. M. Newstead, P. Phillips, T. E. Whall, and E. H. C. Parker, Extended abstracts of the 1993 International Conference on Solid State Devices and Materials, Makuhari, 237 (1993).

[71] R. People and J. C. Bean, Appl. Phys. Lett. **49,** 229 (1985).

[72] M. R. Sardela, Jr. and G. V. Hansson, Appl. Phys. Lett. **65,** 1442 (1994).

[73] S. Mantl, B. Holländer, W. Jäger, B. Kabius, H. J. Jorke, and E. Kasper, Nucl. Instrum. Methods B **39,** 405 (1989).

[74] B. T. Chilton, B. J. Robinson, D. A. Thompson, T. E. Jackman, and J. -M. Baribeau, Appl. Phys. Lett. **54,** 2 (1989).

[75] D. C. Paine, D. J. Howard, N. G. Stoffel, and J. H. Horton, J. Mater. Res. **5,** 1023 (1990).

[76] M. Vos, C. Wu, I. V. Mitchell, T. E. Jackman, J. -M. Baribeau, and J. P. McCaffrey, Appl. Phys. Lett. **58,** 951 (1991).

[77] D. J. Eaglesham, J. M. Poate, D. C. Jacobson, M. Cerullo, L. N. Pfeiffer, and K. West, Appl. Phys. Lett. **58,** 523 (1991).

[78] T. E. Haynes and O. W. Holland, Appl. Phys. Lett. **61,** 61 (1992).

[79] M. Vos, C. Wu, I. V. Mitchell, T. E. Jackman, J. -M. Baribeau, and J. P. McCaffrey, Nucl. Instrum. Methods B **66,** 361 (1992)

[80] G. Bai and M. -A. Nicolet, J. Appl. Phys. **71,** 4227 (1992).

[81] D. Y. C. Lie, A. Vantomme, F. Eisen, M. -A. Nicolet, V. Arbet-Engels, and K. L. Wang, Mater. Res. Soc. Symp. Proc. **262** (1993).

[82] P. Kringhøj, J. M. Glasko, R. G. Elliman, Nucl. Instrum. Methods B **96,** 276 (1995).

[83] H. Ryssel, and I. Ruge, Ion implantation. New York: John Wiley (1986).

[84] J. F. Ziegler, Ion implantation science and technology, 2nd Ed., Academic Press (1988)

[85] P. Ehrhart, J. Nucl. Mat. **216,** 170 (1994).

[86] J. C. Bean, L. C. Feldman, A. T. Fiory, S. Nakahara, I. K. Robinson, J. Vac. Sci. Technol. **A2,** 436, (1984).

[87] E. Kasper, H. -J. Herzog, and H. Kibbel, Appl. Phys. **8,** 199 (1975).

[88] K. Huang, Proc. R. Soc. **A190,** 102 (1947).

[89] P. H. Dederichs, J. Phys. F. **3,** 471 (1973).

[90] V. M. Kaganer, R. Köhler, M. Schmidbauer, R. Opitz, and B. Jenichen, Phys. Rev. B **55,** 1793 (1997).

[91] J. C. Campuzano, M. S. Foster, G. Jennings, R. F. Willis, and W. Unertl, Phys. Rev. Lett. **54,** 2684 (1985).

[92] W. Moritz and d. Wolf, surf. Sci. **163,** L655 (1985); L. D. Marks, Phys. Rev. Lett. **51,** 1000 (1983); M. Copel and T. Gustafson, Phys. Rev. Lett. **57,** 723 (1986).

[93] E. C. Sowa, M. A. van Hove, and D. L. Adams, Surf. Sci. **199,** 174 (1988); G. L. Kellog, Phys. Rev. Lett. **55,** 2168 (1985); P. Refy, W. Moritz, and d. Wolf, Phys. Rev. B **38,** 7275 (1988).

[94] I. K. Robinson, Phys. Rev. Lett. **50,** 1145 (1983); I. K. Robinson, Y. Kuk, and L. C. Feldman, Phys. Rev. B **29,** 4762 (1984).

[95] I. K. Robinson, E. Vlieg, and K. Kern, Phys. Rev. Lett. **63,** 2578 (1989).

[96] B. Z. Olshanetsky and V. I. Mashanov, Surf. Sci. **111,** 414 (1981).

[97] Y. -N. Yang, E. D. Williams, R. L. Park, N. C. Bartelt, and T. L. Einstein, Phys. Rev. Lett. **64,** 2410 (1990).

[98] Y. -N. Yang, N. C. Bartelt, T. L. Einstein, R. L. Park, and E. D. Williams, in *The structure of Surfaces III,* edited by K. Takayanagi and X. D. Xie, Springer-Verlag, Berlin, (1991).

[99] D. L. Avernathy, S. Song, K. I. Blum, R. J. Birgeneau, and S. G. J. Mochrie, Phys. Rev. B **49,** 2691 (1994); D. L. Avernathy, R. J. Birgeneau, K. I. Blum, and S. G. J. Mochrie, Phys. Rev. Lett. **71,** 750 (1993).

[100] S. D. Wolter, B. P. Luther, D. L. Wlatemyer, C. Önneby, S. E. Mohney, and R. J. Molnar, Appl. Phys. Lett. **70,** 2156 (1997).

Vita

Chinkyo Kim was born on Sep. 17, 1970 in In-Cheon, the second largest harbor in Korea. He received a B.S. in physics from Seoul National University with honors in 1993 and an M.S. in physics from University of Illinois at Urbana-Champaign in 1995. He had received Undergraduate Special Fellowship from Korean Foundation for Advanced Studies from 1990 through 1993. And he had received Fellowship for Study Abroad from the same foundation from 1994 through the end of his study at the University of Illinois.

A list of publications:

1. "Critical thickness of GaN thin films on sapphire (0001)", Chinkyo Kim, I. K. Robinson, Jaemin Myoung, Kyu-Hwan Shim, Myung-Cheol Yoo and Kyekyoon Kim, Appl. Phys. Lett. **69,** 2358 (1996)

2. "Optical characteristics of p-type GaN films grown by plasma-assisted molecular beam epitaxy", J. M. Myoung, K. H. Shim, C. Kim, O. Gluschenkov, K. Kim, S. Kim, D. A. Turnbull and S. G. Bishop, Appl. Phys. Lett. **69,** 2722 (1996)

3. "Refined structure of $(\sqrt{3} \times \sqrt{3})$ Sb/Si(111)", Chinkyo Kim, D. A. Walko and I. K. Robinson, Surf. Sci. **388,** 242 (1997)

4. "Effect of growth temperature on the properties of p-type GaN grown by plasma-assisted molecular beam epitaxy", J. M. Myoung, K. H. Shim, O. Gluschenkov, C. Kim, K. Kim, S. Kim and S. G. Bishop, Accepted for publication in J. Cryst. Growth

5. "Extrapolation of critical thickness of GaN thin films from lattice constant data using synchrotron X-ray", Chinkyo Kim, I. K. Robinson, Jaemin Myoung, Kyuhwan Shim, Kyekyoon Kim and Myung-Cheol Yoo, Mat. Res. Soc. Symp. Proc. **423,** 557 (1996)

6. "High quality p-type GaN films grown by plasma-assisted molecular beam epitaxy", J. M. Myoung, C. Kim, K. H. shim, O. Gluschenkov, K. Kim and M. C. Yoo, Mat. Res. Soc. Symp. Proc. **423,** 385 (1996)

7. "Growth and characterization of AlGaN/GaN heterostructures with multiple quantum well by PAMBE", K. H. Shim, J. M. Myoung, O. V. Gluschenkov, C. Kim, K. Kim, M. C. Yoo, S. Kim, D. A. Turnbull and S. G. Bishop, Mat. Res. Soc. Symp. Proc. **423,** 347 (1996)